DEVELOPMENT AND APPLICATION OF INTEGRATED OZONE CONTACTOR DESIGN AND OPTIMIZATION TOOLS

A Thesis
Presented to
The Academic Faculty

by

Doo-Il Kim

In Partial Fulfillment
of the Requirements for the Degree
of Doctor of the Philosophy in the
School of Civil and Environmental Engineering

Georgia Institute of Technology

August 2007

DEVELOPMENT AND APPLICATION OF INTEGRATED OZONE CONTACTOR DESIGN AND OPTIMIZATION TOOLS

Approved by:

Dr. JAEHONG KIM, Advisor
School of Civil and Environmental Engineering.
Georgia Institute of Technology

Dr. THORSTEN STOESSER
School of Civil and Environmental Engineering
Georgia Institute of Technology

Dr. E. MICHAEL PERDUE
School of Earth and Atmospheric Science
Georgia Institute of Technology

Dr. SOTIRA YIACOUMI
School of Civil and Environmental Engineering
Georgia Institute of Technology

Dr. PHILIP J. W. ROBERTS
School of Civil and Environmental Engineering
Georgia Institute of Technology

Date Approved: 05 16, 2007

[To my family]

ACKNOWLEDGEMENTS

I thank all members of my Ph. D. committee, Dr. Jae-Hong Kim, Dr. Thorsten Stoesser, Dr. E. Michael Perdue, Dr. Sorita Yiacoumi, and Dr. Philip J. W. Roberts for their support and advice for my research. Especially, I'd like to thank my advisor, Dr. Jae-Hong Kim, without his guidance and support I would not be here. I would compare him to a great sculptor who creates priceless fine art from humble raw material. It was my great pleasure to do research with him over the last five years. I also acknowledge Dr. Roberts for his huge support of my research and Dr. Semih Nemlioglu who guided me into the world of the 3D-LIF.

I am grateful to my old office mate, Dr. Yong-Gyun Park, who has been sharing a good friendship with me ever since. I also thank many colleagues in my research group, Hyung Hoon, Dr. Jae-Sang Lee, Pranay Mane, Amisha Shah, Wan-Ru Chen, Yu Miyashita, Lokesh Padhye, Sang-Hyuck Park, Seung-Jin Lee who shared creative ideas with me in the laboratory. I specially thank Saurabh Marda who had a lot of fun with me when doing monochloramine research. I appreciate visiting scholars, Dr. Sung-Hong Kim, Dr. Yeon-Gu Jeong, Dr. Se-Yong Nam, and Yong-Mo Cho, who gave me fresh ideas. I acknowledge all the faculties, staffs, and other students in the environmental engineering department for their excellent instructions and support.

My greatest thanks goes to my wife, Hye-Seung Lee, for her devotion to the family during five years of my study in the US and to my lovely daughter, Ji-Yoon, and my son,

Sung-Min, for whom I always feel sorry because I did not to spend enough time. I owe great thanks to my parents, parents-in-law, my brother, and my sister for their unconditional love.

I'd like to acknowledge Dr. Myung J. Kim, Dr. Chea-Young Lee, and Beom-Han Yoon for their priceless support during my research. I would like to thank the beautiful David L. Tippin Water Treatment Facility in Tampa, Fl for allowing me to do very practical research there along with Dr. Myung J. Kim with whom I had great discussions.

This research is partially funded by Georgia Tech. and the USEPA in the United States, KOWACO, HEC and Shinwoo Engineering in South Korea.

TABLE OF CONTENTS

LIST OF TABLES

LIST OF FIGURES

LIST OF SYMBOLS AND ABBREVIATIONS

θ	Dimensionless time
τ	Mean residence time
υ	Kinematical viscosity (L^2T^{-1})
ρ	Water density (ML^{-3})
σ_θ^2	Variance
A_D	Frequency factor for ozone demand decay
A_{indigo}	Absorbance of indigo solution
A_N	Frequency factor for microbial inactivation
A_R	Frequency factor for ozone decay
A_{water}	Absorbance of water
C	Concentration (ML^{-3})
D	Ozone demand (ML^{-3})
d	Dispersion number
D	Diffusivity (L^2T^{-1})
D_0	Initial Ozone demand (ML^{-3})
E	Residence time distribution
E_θ	Dimensionless residence time distribution
$E_{D,a}$	Activation energy for ozone demand decay (J/mol)
$E_{N,a}$	Activation energy for microbial inactivation (J/mol)
$E_{R,a}$	Activation energy for ozone decay (J/mol)
F	Accumulative residence time distribution
f	Flow rate of DI water divided by total flow rate
F_θ	Dimensionless accumulative residence time distribution

Fr	Froude number
g	Gravitational acceleration (LT^{-2})
H	Channel Height (L)
I_b	Standard black image pixel light intensity
I_c	Vignetting corrected pixel light intensity
I_{cc}	Attenuation corrected pixel light intensity
I_r	Raw image pixel light intensity
I_s	Standard white image pixel light intensity
k_D	First order ozone decay kinetic constant (T^{-1})
k_La	Volumetric mass transfer coefficient (T^{-1})
k_N	Second order inactivation kinetics ($L^3M^{-1}T^{-1}$)
k_NCt_{lag}	Delay factor
k_R	Second order rate constant for ozone demand decay ($L^3M^{-1}T^{-1}$)
L	Characteristic length
L	Reactor length (L)
N	Number density of viable microorganism (L^{-3})
N_0	Number density of viable microorganism (L^{-3}) at time zero
$[O_3]_l$	Liquid phase ozone concentration (ML^{-3})
P	Laser intensity at x
P_0	Laser intensity at x_0
R	Ideal Gas Constant (8.314 J/mol/^oK)
Re	Reynolds number
t	Time (T)
T_{10}	Time required 10% of tracer to pass through a reactor (T)
U	Velocity (LT^{-1})

W	Reactor width (L)
We	Weber number
z	Axial distance (L)
3D-LIF	Three Dimensional Laser Induced Fluorescence
A/D	Analog/Digital
ADR	Axial Dispersion Reactor
APHA	American Public Health Association
C. parvum	*Cryptosporidium parvum*
CFD	Computational Fluid Dynamics
COV	Coefficient Of Variance
CSTR	Continuous Stirred Tank Reactor
CT	Concentration × Time
FBD	Fine Bubble Diffuser
FIA	Flow Injection Analysis
HDT	Hydraulic Detention Time
I.D.	Inner Diameter
LIF	Laser Induced Fluorescence
LT2SWTR	Long Term 2 Surface Water Treatment Rule
LWPOF	Linnwood Water Plant Ozone Facility
MC-SFR	Multi-Channel Stopped Flow Reactor
NOM	Natural Organic Matter
OCM	Ozone Contactor Model
*p*CBA	*p*-Chloro Benzoic Acid
PFR	Plug Flow Reactor
PLC	Programmable Logic Controller

RTD	Residence Time Distribution
SFR	Stopped Flow Reactor
SV	Solenoid Valve
SVI	Side-stream Venturi Injector
SVI-DT	Side-stream Venturi Injector Down-flow Tube
UK	United Kingdom
US EPA	United States Environmental Protection Agency
UV	Ultra Violet

SUMMARY

Noble integrated ozone contactor design and optimization tools, including an instrument that measures ozone decay kinetics real time, the software that performs predictive simulation, and an experimental method to examine hydrodynamic characters within the ozone contactor, are practical tools developed in this study for new and existing ozone contactor, simultaneously maximizing disinfection efficiency and minimizing of disinfection by-product formation.

Multi-channel stopped-flow reactor (MC-SFR) is an instrument developed and verified for automatic, continuous analysis of ozone decay kinetics in changing natural waters. Highly controlled MC-SFR system provides rapid, accurate, and reproducible measurement of ozone decay kinetics. This system showed capability to estimate hydroxyl radical exposure during initial phase of ozone decay, which was a challenge using an existing system. MC-SFR system also showed potential for real time kinetics measurement required for automatic control and optimization of an ozone contactor.

Ozone Contactor Model (*OCM*) is the software developed as an innovative tool for full-scale ozone bubble-diffuser contactor design and optimization in support of current and future regulations regarding pathogen and bromate control in drinking water. Application of the *OCM* software for the simulation of a full-scale ozone contactor performance with respect to *Cryptosporidium parvum* oocyst log inactivation and bromate formation was performed using experimental results obtained from Linnwood Water Plant Ozone Facility (LWPOF) at Milwaukee Water Works, Milwaukee, WI. *OCM* software predicted residual ozone concentration and bromate formation accurately and is verified as a promising tool for design and optimization of a full scale ozone

contactor. Each chamber of the ozone contactor showed CSTR-like hydrodynamic characteristics and needs to be modified into plug flow by reducing non-ideal flow such as short-circuiting and back-flow.

Three dimensional laser induced fluorescence (3D-LIF) allows real time characterization of mixing conditions in a physical model ozone contactors by capturing fluorescence image emitted from a laser dye (i.e., Rhodamine 6G) using a high speed CCD camera. 3D-LIF system analyzed the hydrodynamics of an ozone contactor with direct discharge jet and side-stream venturi injector (SVI). Direct discharge into an ozone contactor unexpectedly resulted in good agreement with axial dispersion reactor (ADR) model and low dispersion. The preferred hydrodynamic characteristics with direct discharge are thought to be closely related to the longitudinal swirling flow created by discharge jet momentum. Analyzing the effect of flow rate and jet diameter on dispersion number and T_{10} showed that 1.35 m jet is optimum for lowest dispersion but lacks lateral mixing, which could be compensated using pipe-line dissolution system before discharge. Multi-porous diffusion wall, installed near the discharge jet to diminish the turbulence, was not effective to decrease dispersion number because it breaks swirling flow and evokes longitudinal back-flow.

3D-LIF experimentally showed non-ideal flow characteristics (i.e., short-circuiting and back-flow) from multi-chambered ozone contactor with fine bubble diffuser (FBD). Non-ideal flow deteriorates dispersion number and T_{10} of multi-chambered ozone contactor and is affected by flow rate. Over- or under-flow baffle opening size, however, rendered minor effects on the dispersion, mixing, and T_{10}.

Finally, integrated tools are applied to the design of a new ozone contactor under planning stage to assess original design and to recommend the improvements. OCM

software simulation suggested additional ozone quenching facility for low pH and temperature, additional ozonation capacity, and target dispersion number range. It was recommended to eliminate two CSTR from original ozone contactor configuration (i.e., two CSTR followed for PFR) because of poor mixing and high dispersion number issues.

CHAPTER 1

INTRODUCTION

Ozone is widely used as a disinfectant for drinking water because of its high efficiency for *Cryptosporidium parvum* oocyst inactivation (Gyürék, et al, 1999;Rennecker, et al, 2000;Driedger, et al, 2001). Lower level of chlorinated disinfection by-product formation is another advantage over chlorine based disinfectant. However, ozone produces bromate, a potential human carcinogen, from bromide (von Gunten & Zobrist, 1993;von Gunten & Hoigné, 1994;Song, et al, 1996;Amy, et al, 2000;von Gunten & Pinkernell, 2000;Kim, et al, 2004). The bromide concentrations in the drinking water sources in the United States range from 27 to 65 μg/L (USEPA, 2003). These values are high enough to potentially form bromate at levels greater than the current maximum contamination level (MCL) of 10 μg/L, regulated by the United States Environmental Protection Agency (USEPA, 1994).

Optimal design and control of ozone disinfection process is required to reduce the risk of over-formation of bromate and maximize ozone disinfection efficiency. However, achieving these dual actions are complex because various parameters including flow hydrodynamics, raw water quality, and operating conditions simultaneously affect both pathogen inactivation and DBP formation. In particular, ozone contactor hydrodynamics play a crucial role in the inactivation efficiency of *C. parvum* oocysts (Roustan, et al, 1993). The importance of an adequate hydrodynamic design becomes more apparent when bromate formation becomes a concern (Roustan, et al, 1996;Kim, et al, 2006a;Kim, et al, 2006b). Predictive models have been therefore developed in the past to provide a solution for these complex optimization problems. Among these models, the axial dispersion reactor (ADR) model coupled with inter-phase mass transfer model and

chemical and biological reactions has been proven very useful to simulate the performance of multi-chambered bubble-diffuser ozone contactors, which are the target of this study.

While the ADR models have been proven useful in laboratory and pilot-scale process validation, real world practice have been challenging. First of all, the models developed in the past have not been tested with the full-scale treatment processes. Second, accuracy and ease of model prediction depends on the availability of fast and reliable input parameters such as ozone decay kinetic constants. Based on the advantages of such predictive models, demand for real time instrumentation that measures reliable ozone decay kinetic constants is growing in the drinking water treatment field. Third, the ADR model prediction does not provide information regarding detailed hydrodynamic conditions for the ozone contactor which can be used to guide the plant retrofitting or redesign. No empirical tool is available to evaluate how specific flow path design and flow rate control affect the overall mixing characteristics and disinfection efficiency.

The objective of this study is to address some of the critical limitations of current modeling practices in ozone contactor design and optimization. The first objective of this study is to develop an instrument can precisely measure ozone decay kinetic constants in a near-continuous manner allowing for easy integration into predictive simulation tools for contactor optimization (Chapter 3). The instrument is referred to as a "multi-channel stopped-flow reactor" (MC-SFR) in this study.

The second objective of this study is to modify the ADR-model based Ozone Contactor Model (*OCM*) software and apply and validate the model through a case study on the full-scale ozone contactors. Ozone contactors at the Linnwood Water Plant Ozone Facility (LWPOF) at the Milwaukee Water Works, Milwaukee, WI were tested. Ozone

and bromate concentrations obtained from full-scale experiments are compared with those obtained from the model simulation results. The *OCM* software is also used to predict the level of *C. parvum* oocyst inactivation. Additional model simulations are performed to illustrate how the *OCM* software can be used for plant design and optimization. (Chapter 4)

The third objective of this study is to apply three-dimensional laser-induced fluorescence (3D-LIF) technology to evaluate the flow hydrodynamics in various types of reactor systems. 3D-LIF quantifies the entire instantaneous tracer concentration field over three dimensional sampling space at very high resolution (Tian & Roberts, 2003). 3D-LIF technique was first applied to analyze hydrodynamics of the new ozone contactor with a side-stream venturi ozone injector (SVI). Analyzed hydrodynamic parameters include the diameter of an influent jet, the dispersion number, the flow rate, and an optional diffusion wall that evenly disperses ozone and the raw water mixture. This chapter is aimed to provide recommendations for design improvement for a new ozone contactor. (Chapter 5)

3D-LIF technique was further applied to analyze hydrodynamics of the multi-chambered Linnwood Water Plant Ozone Facility with fine bubble diffuser and vertical flow by a conservative tracer test using 3D-LIF. This research will focus on non-ideal flow characteristics of each ozone chamber, which has short-circuiting and back-flow. Influence of flow rate, the baffle opening width, and the number of chambers on dispersion will be revealed. (Chapter 6)

Finally, MC-SFR, *OCM* software, and 3D-LIF as a integrated design tools were applied to design a new ozone contactor in South Korea. The purpose of this chapter is to predict residual ozone concentration, *CT*, bromate formation, and *C. parvum* oocyst log

inactivation using OCM software and kinetic constant obtained using MC-SFR. The predicted value directly used to decide initial ozone concentration, operational pH, and quenching capacity according to temperature. Hydrodynamics of original design are analyzed and recommendations are provided using 3D-LIF. (Chapter 7)

CHAPTER 2

BACKGROUND

2.1. Ozone

2.1.1. Ozone Decay in the Aqueous Phase

Ozone has a much stronger oxidation potential than other oxidants such as free chlorine and monochloramine that are commonly used for water treatment. It reacts either directly or indirectly with diverse compounds in water, most pronouncedly through a dipolar cyclo-addition on an unsaturated bond and an electrophilic or nucleophilic attack (Langlais, et al, 1991). These direct reactions are highly selective in unsaturated aromatic and aliphatic compounds (Hoigné et al, 1985). Ozone in the aqueous phase is degraded auto-catalytically. Ozone decay mechanism has been studied by many researchers, and models such as HSB model (Staehelin & Hoigné 1982; Buhler et al., 1984; Staehelin et al., 1984) and GTF model (Tomiyasu et al., 1985) are the most notable ones. The hydroxyl radical, a product of ozone degradation, is also an oxidant that is highly reactive non-selectively in various compounds in water (Hoigné & Bader, 1976; von Gunten, 2003).

Ozone degradation is affected by various organic and inorganic compounds that exist in natural water. The hydroxide ion plays an important role of initiating a chain reaction (Langlais et al, 1991). Humic acids and phosphate species can regenerate the super oxide anion ($O_2 \cdot^-$) from the hydroxyl radical, the process of which is referred to as "promotion" in the chain reaction (Hoigné et al., 1987). Bicarbonate, carbonate, and humic substances can consume the hydroxyl radical without producing a super oxide anion, which decreases the ozone decay rate in natural water (Singer et al., 1992; Elovitz & von Gunten, 1997; Elovitz & von Gunten, 1999). While ozone decay is affected by

diverse constituents in natural water, its decay kinetics are well expressed with first-order kinetic expression, as shown at Equation (2.1) (Singer & Hull, 2000).

$$\frac{d[O_3]_l}{dt} = -k_D[O_3]_l \tag{2.1}$$

where $[O_3]_l$ is liquid phase ozone concentration (ML^{-3}), t is time (T), and k_D is the first-order ozone decay kinetic constant (T^{-1}). Lev and Regli (1992a) incorporated a second-order rate term for natural organic matter and modified Equation (2.1) into Equations (2.2) and (2.3)

$$\frac{d[O_3]_l}{dt} = -k_D[O_3]_l - k_R[D]\cdot[O_3]_l \tag{2.2}$$

$$\frac{d[D]}{dt} = -k_R[D]\cdot[O_3]_l \tag{2.3}$$

where $[D]$ is the ozone demand (ML^{-3}), and k_R is the second-order rate constant for the ozone demand decrease ($L^3M^{-1}T^{-1}$). Rate constants k_D and k_R are affected by temperature and represented by an Arrhenius expression, as shown at Equations (2.4) and (2.5), respectively.

$$k_D = A_D \times \exp(-\frac{E_{D,a}}{RT}) \tag{2.4}$$

$$k_R = A_R \times \exp(-\frac{E_{R,a}}{RT}) \tag{2.5}$$

where $E_{D,a}$ and $E_{R,a}$ are the activation energy (J/mol), A_D and A_R are frequency factors, R is the ideal gas constant (8.314 J/mol/^oK), and T is the absolute temperature (^oK).

2.1.2. Ozone in Water Treatment

Used in drinking water treatment in Europe more than one hundred years, ozone disinfection has proven effective, as the strong oxidation potential of ozone is more efficient at inactivating the *C. parvum* oocyst, virus and *Giardia* than chlorine-based disinfectants (Gyürék et al., 1999; Rennecker et al., 1999; Rennecker et al., 2000). Ozone produces much less THM and HAA compared to free chlorine (Reckhow et al., 1986; Hoigné & Bader, 1988; Dojlido et al., 1999). Additionally, ozone has the following advantages: 1) Ozone can remove taste- and odor-producing compounds (Kusakabe et al., 1991; Hwang et al., 1994; Andreozzi et al., 2003); 2) ozone can increase biodegradability for the biological filter (Gilbert, 1987; Amy et al., 1991; Adams et al., 1997; Carlson & Silverstein, 1997; Melin & Odegaard, 2000; Andreozzi et al., 2001; Nishijima et al., 2003; Yavich et al., 2004); 3) ozone can oxidize ferrous (Fe^{2+}), manganese (Mn^{2+}), ammonia, algal toxins, antibiotic chemicals, and pesticides (Singer & Zilli, 1975; Dore et al., 1980; Elmgharitabib et al., 1982; Kowbel et al., 1982; Mason et al., 1990; Stockinger et al, 1996; Yang et al., 1999; Rositano et al., 2001); and 4) ozone can enhance coagulation efficiency. Ozonation, however, is accompanied by human carcinogenic disinfection by-product formation such as bromate.

2.2. Disinfecting Encysted Parasites from Surface Water

Encysted parasites such as *Giardia lamblia* and *Cryptosporidium parvum* are more resistant to conventional chlorination practices, difficult to detect due to their low concentration in surface water, and reported to cause acute water-born diseases in North America (Finch & Belosevic, 2001). As ozone can effectively inactivate these encysted pathogens, the ozonation process has recently been extensively adopted in the United States.

The inactivation kinetics of *Giardia lamblia* and *Cryptosporidium parvum* are expressed by the following Chick-Watson Model and the Delayed Chick Watson Model, shown at Equations (2.6) and (2.7).

The Chick-Watson Model: $\ln\frac{N}{N_0} = -k_N CT$ (2.6)

The Delayed Chick Watson Model:

$$\ln\frac{N}{N_0} = \begin{cases} 0 & Ct < Ct_{lag} = \frac{1}{k_N}\ln\frac{N}{N_0} \\ -k_N Ct - k_N Ct_{lag} & Ct \geq Ct_{lag} = \frac{1}{k_N}\ln\frac{N}{N_0} \end{cases} \quad (2.7)$$

where N, N_0, k_N, C, t, and $k_N Ct_{lag}$ are the number density of viable microorganisms, the initial number density of viable pathogens, the second-order inactivation rate constants ($L^3M^{-1}T^{-1}$), the disinfectant concentration (ML^{-3}), the time (T), and the delay factor, respectively. The dependence of the inactivation kinetic rate constant (k_N) on temperature is expressed by the following Arrhenius equation.

$$k_N = A_N \times \exp(-\frac{E_{N,a}}{RT}) \quad (2.8)$$

where A_N is the frequency factor, $E_{N,a}$ is the activation energy (J/mol), R is the ideal gas constant (8.314 J/mol/^{o}K), and T is the absolute temperature (^{o}K). A second-order inactivation kinetic constant k_N ($L^3M^{-1}T^{-1}$) for *C. parvum* oocyst was suggested by Clark

et al. (2002) and the USEPA (USEPA, 2006), as shown in Equations (2.9) and (2.10) respectively, which are often used for the predictive model.

$$k_N = 0.118 \times 1.1^T \quad (2.9)$$

$$k_N = 0.0917 \times 1.097^T \quad (2.10)$$

where T is the temperature (^oC).

2.3. Bromate

2.3.1. Bromate: The Disinfection By-product of Ozone Disinfection

Bromate has been classified as a potentially carcinogenic inorganic compound by the International Agency for Research on Cancer (IARC) (WHO, 1990) and limited to 10 μg/L, the maximum contamination level (MCL) accepted in the United States (Federal Register, 1994). Bromate is a byproduct of the process of disinfection during the ozonation of raw water, which contains bromide. It has been reported to be a cause of kidney cancer in laboratory animals (Siddiqui et al., 1996).

2.3.2. Factors Affecting Bromate Formation

Bromate is produced from bromide, which reacts with hydroxyl radicals and ozone, as shown at Figure 2.1. Affected by many operational factors and raw water quality during ozonation, bromate formation is associated with higher ozone, hydroxyl radical concentrations, temperature, and contact time. A higher pH of the ozone contactor promotes bromate formation by producing more hydroxyl radicals at the initial phase and deprotonating HOBr at the secondary phase. OBr^- is more closely associated with bromite (BrO_2^-) formation than HOBr because it reacts with ozone, a more effective pathway than going through BrO• by reacting with hydroxyl radicals, which is rare in the secondary phase.

The quality of raw water, which may include bromide, ammonia, and natural organic matter, also influences bromate formation. The amount of bromide in raw water strongly affects its production. Ammonia consumes HOBr/OBr^- and turns into bromamine (NH_2Br), which is converted into a bromide anion (Br^-). Carbonate and bicarbonate scavenge hydroxyl radicals but result in carbonate radical production, which might promote bromate formation. Another influencing bromate formation, although more complex, is natural organic matter. It reacts with molecular ozone and hydroxyl radical, producing stable product or secondary oxidants. However, natural organic matter leads to the formation of bromo-organic compounds by reacting with HOBr/OBr^-, which reduces bromate formation.

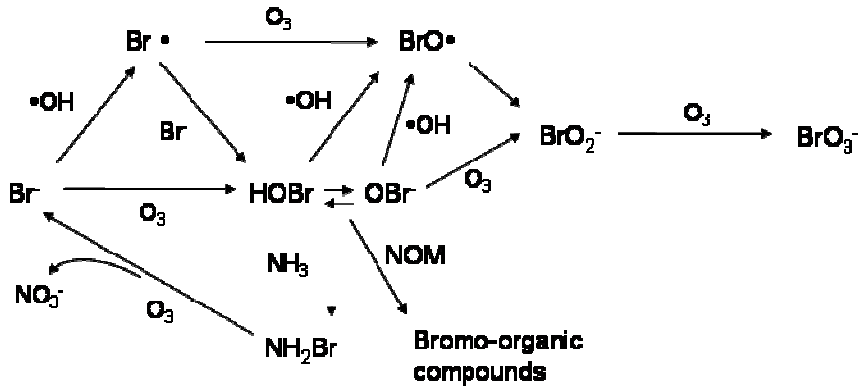

Figure 2.1. Mechanical model of bromate formation during ozonation of natural water (Pinkernell & von Gunten, 2001; Kim et al, 2007)

2.3.3. Methods for Reducing Bromate Formation during Ozonation

The process of bromate formation is divided into the rapid initial phase and the slower secondary phase (Pinkernell & von Gunten, 2001). The initial phase for bromate formation is affected by hydroxyl radicals and the secondary phase by both ozone and

hydroxyl radicals (Driedger et al., 2001; Pinkernell & von Gunten, 2001). Low pH leads to low hydroxyl radical formation, but it could also result in low bromate formation (von Gunten & Pinkernell, 2000; Driedger et al., 2001). Ammonia, if added, could consume $HOBr/OBr^-$ and lessen bromate formation. Both methods are practical ways in controlling bromate formation in a drinking water treatment facility with ozonation.

2.3.4. Balancing Bromate Formation and Pathogen Inactivation

A higher degree of pathogen inactivation is incorporated with strong exposure to ozone, which might lead to excessive bromate formation. Thus, during ozonation, achieving higher inactivation and lower bromate formation simultaneously is a conflicting goal. In particular, during low temperature seasons, more ozone is needed to achieve target inactivation, but it results in higher bromate production. Lower bromate formation can be achieved by lowering pH and adding ammonia. However, low pH might become problematic because of excessively high residual ozone concentration, and the added ammonia could boost nitrification in the distribution network.

2.4. Ozone Contactor Hydrodynamics

2.4.1. Disinfection Efficiency and Hydrodynamics

The most ideal reactor types, frequently found in ozone contactor designs, are the continuously stirred tank reactor (CSTR) and the plug flow reactor (PFR). While the CSTR is well mixed and has uniform concentration, the PFR is characterized by the plug flow that does not allow mixing between adjacent flow elements (Levenspiel, 1999). These ideal flow patterns cannot represent real flow patterns in an ozone contactor that prevents ideal flow because it leads to short-circuiting and back-flow, and creates a stagnant zone. These problematic flow characteristics could be analyzed by two- or three-dimensional fluid visualization tools such as computational fluid dynamics (CFD). However, a one-dimensional residence time distribution (RTD) curve is still a practical

way to analyze the flow characteristics in an ozone contactor. The RTD graph is often represented by the dimensionless exit age distribution curve, E, which is defined mathematically by Equation (2.11). The Mean residence time (τ) is defined in Equation (2.12). E_θ, as shown in Equation (2.13), is more often used than E with a dimensionless time term (θ), shown in Equation (2.14). The F curve is defined as the accumulation of the E curve, as shown in Equation (2.15).

$$E = \frac{C}{\int_0^\infty C dt} \cong \frac{C}{\sum_i C_i \Delta t_i} \tag{2.11}$$

$$\tau = \frac{\int_0^\infty tC dt}{\int_0^\infty C dt} \cong \frac{\sum_i t_i C_i \Delta t_i}{\sum_i C_i \Delta t_i} \tag{2.12}$$

$$E_\theta = \tau \times E \tag{2.13}$$

$$\theta = \frac{t}{\tau} = \frac{t}{\frac{\int_0^\infty tC dt}{\int_0^\infty C dt}} \cong \frac{t}{\frac{\sum_i t_i C_i \Delta t_i}{\sum_i C_i \Delta t_i}} \tag{2.14}$$

$$F = \int_0^t E dt \tag{2.15}$$

Figure 2.2 a) shows representative RTD curve obtained from a full-scale fine bubble diffuser (FBD) ozone contactor with a 43MGD flow rate using sodium fluoride, a conservative tracer. E_θ, and F_θ are obtained by the previous equations. From the F_θ curve of this figure, the T_{10} value can be obtained from the dimensionless time axis, which is used for obtaining CT_{10} values in which C is the average ozone concentration and T_{10} is defined as the time needed for 10% of the non-reactive tracer to pass through a reactor. Note that the efficiency of ozone contactor disinfection is regulated based on CT_{10} values proposed by the USEPA (1991).

The axial dispersion model (ADR) is used to represent the flow motion close to the plug flow reactor, expressed mathematically in Equation (2.16):

$$\frac{\partial C(\theta,z)}{\partial \theta} = d\frac{\partial^2 C(\theta,z)}{\partial z^2} - \frac{\partial C(\theta,z)}{\partial z} \tag{2.16}$$

where C is the conservative tracer concentration (ML^{-3}), d is the dispersion number (dimensionless), defined as Equation (2.17), z is the axial distance (L), and θ is dimensionless time.

$$d = \frac{D}{UL} \tag{2.17}$$

where D is the diffusivity (L^2T^{-1}), U is the flow velocity (LT^{-1}), and L is the characteristic length (L). The dispersion number (d) is obtained by solving equation (2.18) for a large dispersion ($d > 0.01$) and a closed reactor after substituting the variance (σ_θ^2), which is obtained from Equation (2.18) (Levenspiel, 1999).

$$\sigma_\theta^2 = 2d - 2d^2 \times (1 - e^{-\frac{1}{d}}) \tag{2.18}$$

$$\sigma_\theta^2 = \frac{\int (t-\tau)^2 C dt}{\int C dt} = \frac{\int t^2 C dt}{\int C dt} - \tau^2 \tag{2.19}$$

If the CSTR is adopted, the hydrodynamic characteristics of an ozone contactor, are affected by the number of CSTR in the series (Lev & Regli, 1992b). The effect of its number is easily compared using the F_θ curves shown in Figure 2.3. This figure shows

that T_{10}/τ, equivalent to 10% of the F_θ curve, increases as the number of CSTR in the series increases, which indicates better disinfection efficiency based on the T_{10} values suggested by USEPA (1991). The dispersion number (d) also affects the hydrodynamic characteristics of the ozone contactor, shown in Figure 2.3, where the T_{10} values decrease as the dispersion number (d) increases from 0.01 to 5.

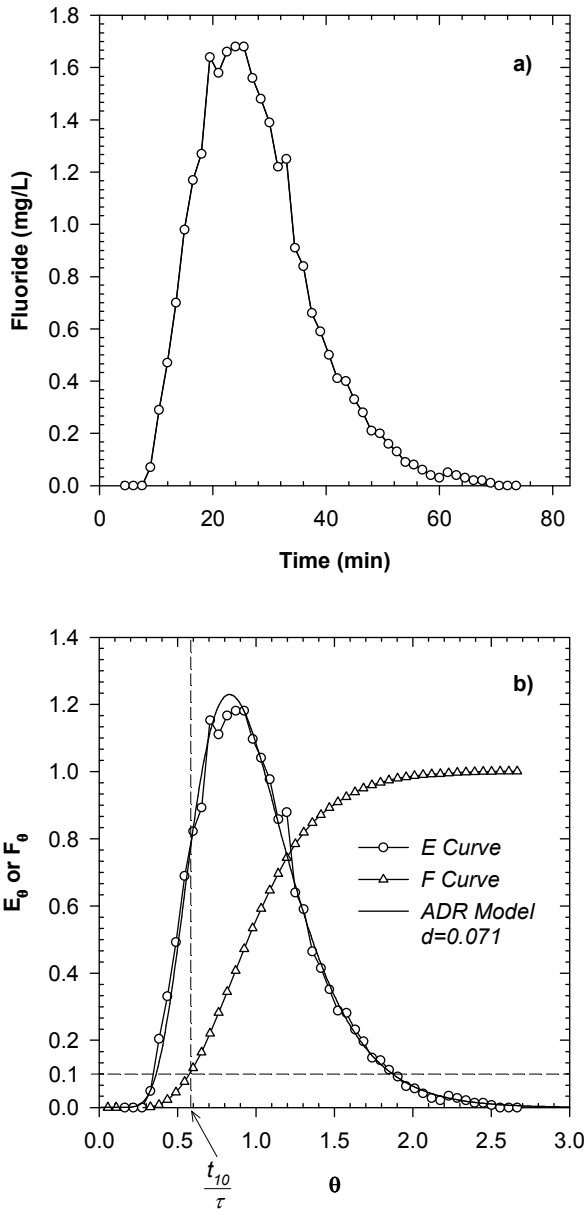

Figure 2.2. Representative RTD graph from a full-scale plant (43MGD) using NaF as a tracer for a), the E and F curves obtained from this RTD, t_{10}/τ, and the ADR model fit for b).

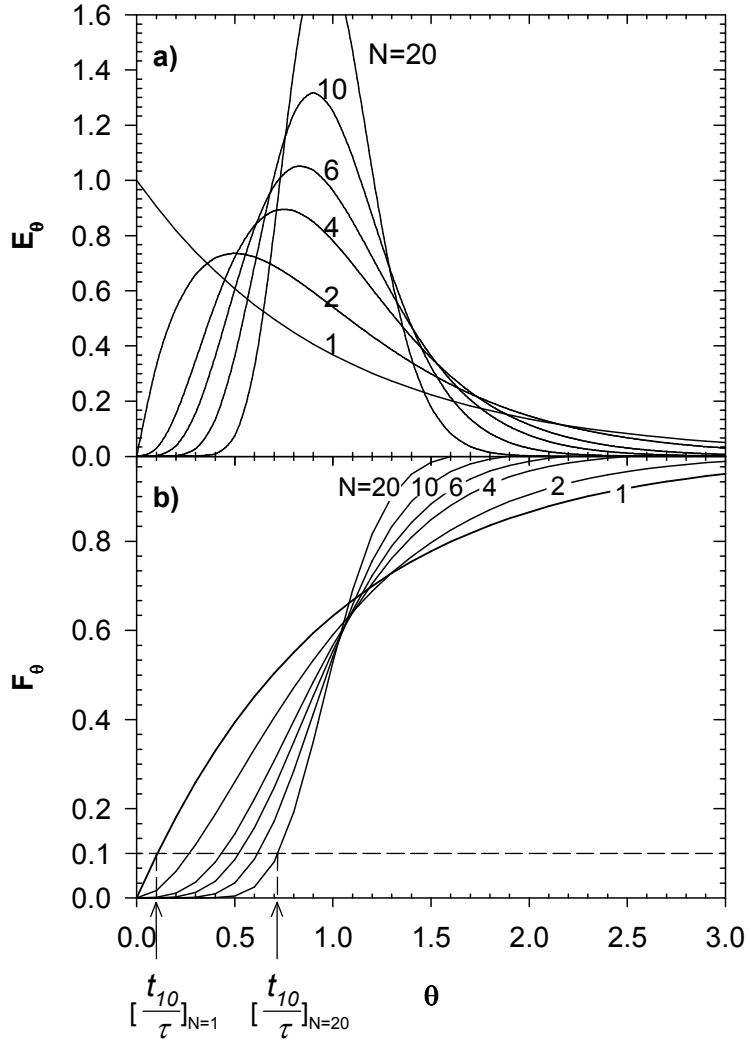

Figure 2.3. Dimensionless RTD graphs for N-CSTR in series model: response for the pulse input for a), for the step input for b) (Levi & Regli, 1992b)

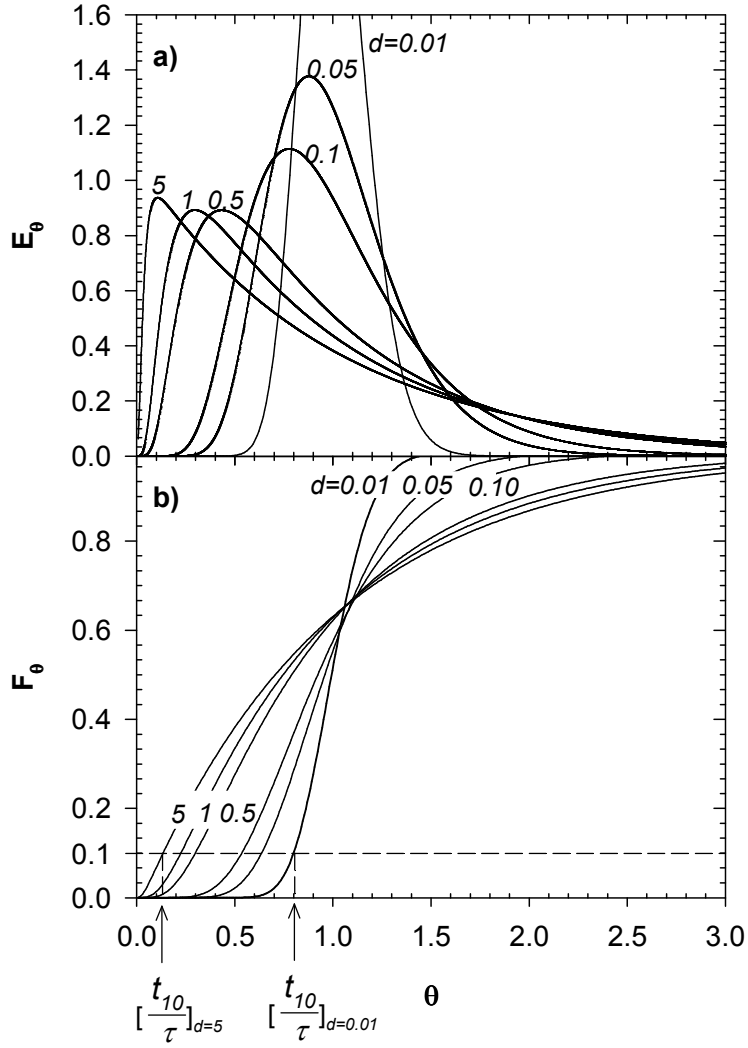

Figure 2.4. Dimensionless RTD graphs for the PFR model with different dispersion numbers (*d*): response for the pulse input for a), response for the step input for b) (Kim, 2002)

2.4.2. Ozonation Methods for Full-Scale Plants

Ozone is generally fed into the ozone contactor by a fine bubble diffuser (FBD) or a side-stream venture injector (SVI). An FBD system, which sparges ozone bubbles through a set of fine bubble diffusers, is used for low to medium ozone concentration with a sufficient volumetric flow rate. However, it might experience the channeling of larger gas bubbles at an insufficient gas flow rate (Schulz et al., 1995). Figure 2.5 illustrates a representative FBD ozone contactor with consecutive four double baffles, which have approximately 20% higher T_{10}/HDT values than a single baffle because a narrow channel between double baffles serves as a plug flow reactor (Do-Quang et al., 2000).

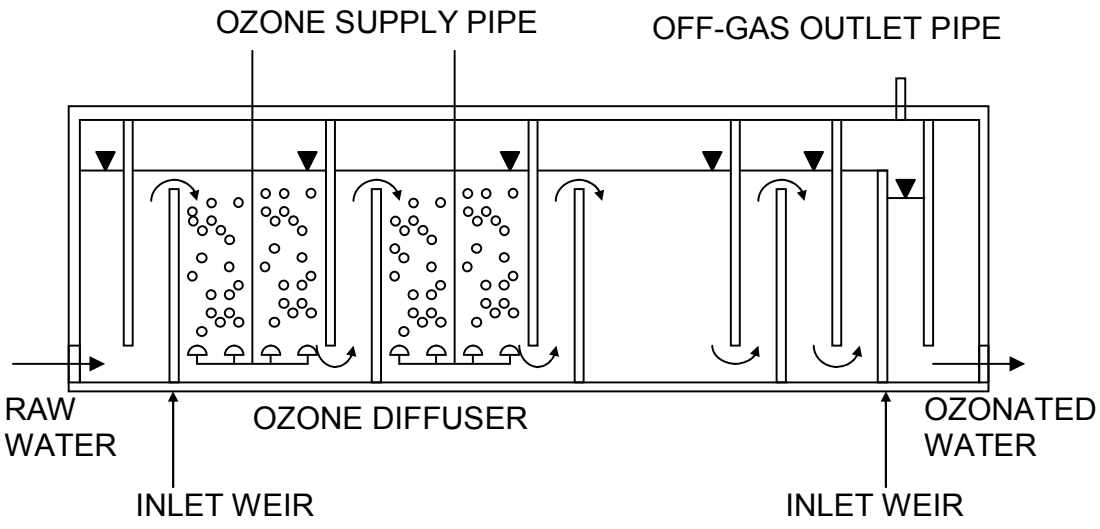

Figure 2.5. Sectional view of an FBD Contactor with a double baffle, the Southwest WTP (Orlando, Florida) (Schulz & Bellamy, 2000)

An SVI system is suitable for high ozone concentration and low volumetric ozone flow rate (Schulz et al., 1995). An SVI, not influenced by the gas flow rate, is free from

diffuser clogging caused by oxidized iron or manganese deposits on a diffuser, and better initial mixing by inflow momentum energy in an ozone contactor. However, drawbacks of the SVI system include possible gas-liquid segregation, higher head loss, and additional pumps for the side-stream (Schulz et al., 1995).

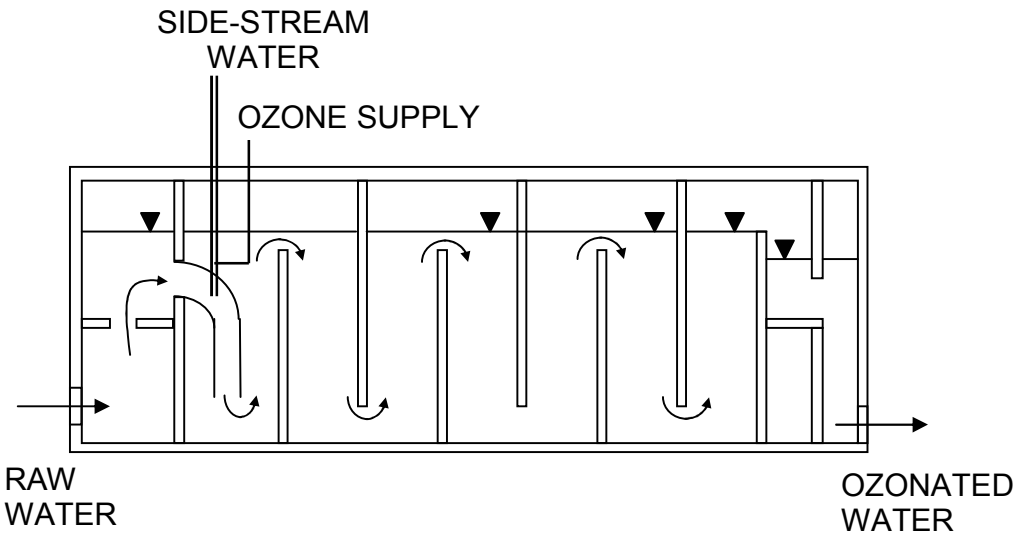

Figure 2.6. Sectional view of an SVI-DT Contactor, the Lanier WTP (Gwinnett County, Georgia) (Schulz & Bellamy, 2000)

2.5. Physical Model Study Using a Scaled Down Reactor

For experiments using three-dimensional, laser-induced fluorescence, a proto-ozone contactor is scaled down into a physical model reactor. The basic principle of scaling down from a proto-plant to a physical model is to share kinematical and geometrical similarities (Schmidtke & Smith, 1983). Kinematical similarity is expressed by dimensionless numbers such as Froude, Reynolds, and Weber numbers, which

represent different mechanisms of fluid motion. The Froude number (*Fr*), used to describe gravitational flow motions with a free surface, is defined as the ratio of inertial force to gravitational force:

$$Fr = \frac{U}{\sqrt{gH}} \tag{2.20}$$

where U is the water velocity (LT^{-1}), g is gravitational acceleration (LT^{-2}), and H is the channel depth (L). The Reynolds number (*Re*) relates inertial force and viscous force as follows:

$$Re = \frac{UL}{\upsilon} \tag{2.21}$$

where L is the characteristic length (L) and v is the kinematic viscosity (L^2T^{-1}). Finally, the Weber number (*We*) defines the effect of surface tension on free surface flow as follows:

$$We = \frac{\rho L U^2}{\sigma} \tag{2.22}$$

where ρ is the density (ML^{-3}) and σ is the surface tension (MT^{-2}). All of these numbers cannot share similitude. Therefore, by neglecting less important dimensional numbers, partial similarity is acceptable.

The following is an example of using Froude number similarity through the Buckingham π theorem (Munson, et al, 1998) to scale down a proto plant to a physical

model. The Buckingham π theorem is based on the dimensional homogeneity of physically meaningful variables; that is, the dimensionless π terms of the proto-scale and physical model-scale reactors should be consistent. All the representative parameters that characterize the flow condition in the reactor (i.e., all the meaningful variables) can be formulated into the following equation:

$$t = f(D, U, g, W, L) \tag{2.23}$$

where t is residence time, D is diffusivity, g is gravitational acceleration, H is height, W is width, and L is length of ozone contactor. This equation can be rearranged as a function of a set of dimensionless π terms:

$$\pi_1 = \varphi(\pi_2, \pi_3, \pi_4) \tag{2.24}$$

where $\pi_1 = \frac{t \times U}{H}$, $\pi_2 = \frac{g \times U}{H^2}$, $\pi_3 = \frac{W}{H}$, and $\pi_4 = \frac{D}{H}$.

Rearranging the above equation results in

$$\frac{t \times U}{H} = \varphi\left(Fr, \frac{W}{H}, \frac{D}{H}\right) \tag{2.25}$$

Therefore, scale-down practices can be implemented if the consistency of the Froude number and the above geometric dimensionless groups can be maintained between the physical model reactor and the proto-scale reactor.

2.6. Three Dimensional Laser-Induced Fluorescence

The three-dimensional laser-induced fluorescence (3D-LIF) technique is an extremely useful tool for the observation of the mixing behaviors of various types of reactor systems. With this technique, the entire instantaneous tracer concentration field at very high resolution in three-dimensional space can be quantified. Laser dye such as Rhodamine 6G emits fluorescence light when it is exposed to a laser beam with its excitation wavelength and sufficient energy. Figure 2.7-a) illustrates linear fluorescence light by a linear laser beam. Planar laser sheets created by reflecting the laser beam using oscillating scanning mirrors and a plano-convex lens can create a two- dimensional fluorescent image, as shown at Figure 2.7-b). Useless reflected light is filtered out by the laser filter, as shown at Figure 2.7-c). Multiple laser sheets created by another orthogonal oscillating mirror compose a set of three-dimensional images.

The images are further processed to correct optical errors (i.e., vignetting) and laser light loss during travel through water (i.e., attenuation) according to Tian and Roberts (2003). The darker image on the margin is referred to as vignetting, which is corrected, pixel by pixel by Equation (2.26), using a standard black and white image.

$$I_c(i,k) = K\frac{I_r(i,k) - I_b(i,k)}{I_s(i,k) - I_b(i,k)} \tag{2.26}$$

where $I_c(i,k)$, $I_r(i,k)$, $I_s(i,k)$, and $I_b(i,k)$ are pixels of corrected, raw, standard white, and black images, respectively, at the i_{th} and j_{th} pixel indices. K is the average pixel value of the standard white image. Images are further processed to correct the attenuation error, which is corrected with Beer's law, as in equation (2.27).

$$P = P_0 e^{-(a_W + 0.00023 \times C)(x - x_0)} \tag{2.27}$$

where P and P_0 are laser intensity at x and x_0 (cm), respectively, a_W, is the attenuation coefficient of water, which ranges from 0.0011 to 0.0045 cm^{-1}, and C is the concentration of Rhodamine 6G (μg/L). Finally, pixels are corrected using Equation (2.28) for attenuation.

$$I_{cc}(i,k) = \frac{I_c(i,j)}{e^{\sum_{m=1}^{i}(a_W + 0.00023 \times C) \times \Delta x}} \tag{2.28}$$

where I_{cc} is the corrected pixel value and Δx is the distance between the two pixels. These correction procedures are done by software called *TFlook*, developed by Tian and Roberts (2003). Rhodamine 6G concentration (C) is obtained from Equation (2.29).

$$C = \mu \times I_{cc} \tag{2.29}$$

where μ is calibration factor.

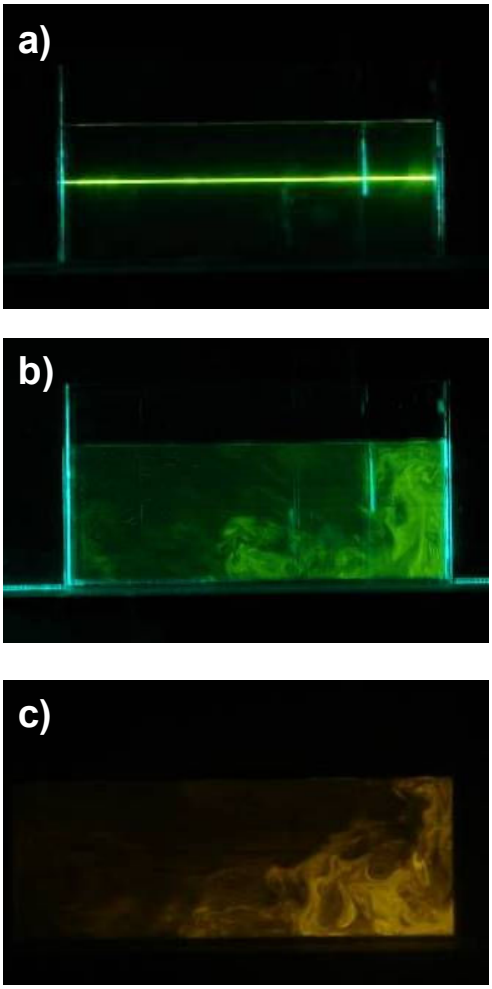

Figure 2.7. Fluorescence emitted by Rhodamine 6G excited by a linear laser beam for a), a two-dimensional fluorescence image excited by a laser sheet for b), a two- dimensional image filtered out using a laser filter for c).

CHAPTER 3

A MULTI-CHANNEL STOPPED-FLOW REACTOR FOR MEASURING OZONE DECAY RATE: INSTRUMENT DEVELOPMENT AND APPLICATION

SHORTENED TITLE: A MULTI-CHANNEL STOPPED-FLOW REACTOR

3.1. Introduction

While ozone is used in diverse water treatment applications including taste and odor control, color removal, oxidation of organic and inorganic species, and flocculation enhancement, the primary goal of ozonation in most water treatment processes has been disinfection (Langlais *et al.*, 1991). The effectiveness of ozone as a disinfectant has been further highlighted by the recently promulgated U.S. EPA's Long Term 2 Enhanced Surface Water Treatment Rule (LT2ESWTR) (USEPA, 2006a). One of the critical issues for contactor operation and design, particularly when considering higher *CT* (residual aqueous ozone concentration × contact time) values required for *Cryptosporidium parvum* oocyst inactivation, is accurately controlling ozone dosage to maintain required efficiencies while minimizing operational cost and controlling the formation of disinfection by-products such as bromate (BrO_3^-) under regulatory requirement (USEPA, 2006b). As recently described by Rakness *et al.* (2005), accurately estimating the rate of ozone decay is a critical component of *CT* estimation under certain design schemes. Furthermore, when decay data is available, reactive transport models can be further employed to simultaneously consider the effects of ozone contactor configuration and operating conditions (Zhou *et al.*, 1994; Kim *et al.*, 2002a; Kim *et al.*, 2002b; Tang *et al.*, 2005). Such models have been verified with lab- and full-scale tests and applied to

achieve maximum contactor efficiency and minimum by-product goals (Kim *et al.*, 2002a; Tang *et al.*, 2005). However, accurate calculations of ozone decay kinetics are challenging in many systems, as ozone decay occurs relatively fast and can vary greatly among natural waters.

Ozone decay is the result of combined effects of ozone auto-decomposition and its reaction with various constituents. In pure water systems, as described in numerous studies, ozone auto-decomposition is initiated by hydroxide ion and propagated by intermediate radical species such as hydroxyl (·OH), superoxide ($HO_2\cdot/\cdot O_2^-$) and ozonide ($HO_3\cdot/O_3^-\cdot$) radicals (Bühler *et al.*, 1984; Staehelin *et al.*, 1984; Staehelin and Hoigné, 1982). When considering such a system, predicting ozone decay using well described elementary chemical reactions has been relatively successful (Kim *et al.*, 2004), However, in natural waters, ozone can also react directly with various organic (e.g., NOM) and inorganic (e.g., Fe^{2+}, carbonate) constituents resulting in further decomposition and corresponding formation of secondary oxidants (e.g., hydroxyl radical) (Hoigné and Bader, 1983a; 1983b; Hoigné *et al.*, 1985). Accordingly, the rates of ozone decay can vary widely between natural waters as a function of multiple water quality parameters (Westerhoff *et al.*, 1997) making accurate predictions of ozone decay kinetics in most natural waters nearly impossible, and unreliable for process incorporation. For a specific natural water, the most reliable decay rate information comes from direct, empirical measurements that inherently account for all the water quality conditions including temporal variability. However, depending on sampling and derivation methodologies, empirical decay kinetic information can remain as the source of uncertainty, often providing conservative estimates of *CT* (Rakness *et al.*, 2005).

When considering an approach for direct, continuous measurements of ozone decay rates, a robust measurement of dissolved ozone in natural water, ensuring precision

and accuracy, in a timely manner is prerequisite. Dissolved ozone in water can be measured by a number of methods with the simplest and most reliable including direct UV measurement at 260 nm (Bahnemann and Hart, 1982) and colorimetric methods that involve the degradation of indigo dye (cleavage of the C=C double bond between of the sulfonated indigo dye) (Bader and Hoigné, 1981) or $Fe(terpy)_2^{2+}$ (bis(terpyridine)iron(II) oxidized to bis(terpyridine)iron(III)) (Tomiyasu and Gordon, 1984), both resulting in a decrease in absorbance at 600 and 552 nm, respectively. While direct absorbance in the UV is the most appropriate for ultra pure water systems, many organic and inorganic solutes can interfere within a direct UV measurement. Due to a relatively high molar extinction coefficient at 600 nm, at which NOM absorbance is low, and a high specific reactivity with ozone but not with secondary oxidants, indigo method has been widely used to measure the concentration of ozone dissolved in natural waters.

An efficient, reproducible methodology for kinetic analysis using the indigo method requires a highly controlled reactor design that precisely considers time as a variable when compared to simple batch type reactors. For example, ozone decay kinetic constants have been obtained by measuring residual ozone concentration in batch reactors by the indigo method after a concentrated ozone stock solution is transferred to the reactor and a predetermined reaction time has elapsed (Cho *et al.*, 2003; Onari, 1988; Park *et al.*, 2001; Park *et al.*, 2004). Disadvantages include possible short-circuiting (*i.e.*, loss to the sampling lines) of concentrated ozone introduced at the onset of the reaction and lower precision due to batch to batch variability. Flow injection analysis (FIA) techniques have been shown to overcome such problems associated with batch reactor design (Onari, 1988; Straka *et al.*, 1985; Straka *et al.*, 1984). In FIA design, a sample mixture flows inside a tubular reactor for a predetermined hydraulic residence time (*i.e.*, corresponding to reaction time) and the residual ozone concentrations are subsequently

measured (Hunt and Mariñas, 1997). However, results obtained under continuous flow conditions are subject to confounding factors from physical process such as dispersion and resulting band broadening (Burguera, 1989). Dispersion is proportional to the square root of the mean residence time (i.e. tube volume divided by pumping rate) or traveled length of tube (Růžička, 1988). As a result, decreasing peak height (*i.e.*, due to dispersion) will decrease the sensitivity of an analysis as a function of time. Similar in concept to FIA design, reaction kinetics can be also be measured via a stopped-flow reactor (SFR) design which simply stops the flow after instantaneous flow-through mixing of reactants (Hungerford *et al.*, 1985) whereby flow via a carrier solution is transported for subsequent measurement when the desired reaction time is reached. In addition to minimizing dispersion associated with typical FIA designs, benefits of SFR design include reduced length of reactor tubes and subsequent sample and reagent volumes (Hungerford *et al.*, 1985). It is also easier to extend this design into synchronized systems for automated analyses when compared to batch type reactors. Additionally, stopped-flow methods have previously been used to investigate kinetics of ozone reaction and decay (Nemes *et al.*, 2000). However, SFR design is also subject to problems associated with dispersion when reaction time is extended over tens of seconds.

The objective of this study was to develop an instrument, named as multi-channel stopped-flow reactor (MS-SFR), which can precisely measure ozone decay kinetic constants in a near continuous manner allowing for easy integration into predictive/simulation tools for contactor optimization. The principle of the instrument is similar to other stopped-flow reactors, however, differing in the fluid separation as it is mechanically separated to minimize dispersion during extended reaction periods. Note that the commonly used method of two-phase segregation via intermittent introduction of gas in a flow-through system could not be considered due to ozone volatility. Therefore, the reaction proceeds similarly to a batch reactor, while transport and measurement

proceed in a similar manner to a flow-through reactor. Data presented in this paper includes reactor parameter optimization, verification of data precision and accuracy, and demonstrated applicability with representative synthetic waters.

3.2. Instrument Development

Figure 3.1 shows a schematic diagram of the MC-SFR. The major components include six (tubular) reactors, two six-channel solenoid valves, a spectrophotometer and two pumps. Inlets of the system consist of two 1.59 mm I.D. Teflon tubes collecting sample water (line S), concentrated ozone stock solution (line O) and one 0.56 mm I.D. Teflon tube collecting ultra-pure distilled water (line D). These lines are connected to a peristaltic pump (Pump A) (MIDI-Digital Driver, Ismatec, Glattbrugg, Switzerland) equipped with three pump heads. After passing the pump, the line S merges with the line D through a T-connector into a 1.59 mm I.D. Teflon tube which further merges with the line O through another T-connector into a Teflon tube with the same I.D. The merged tube is further connected to a static mixer followed by a direct-lift type 6-channel solenoid valve (SV1) (6X Gradient Manifold Isolation Valves, Nresearch, West Caldwell, NJ) which distributes the incoming mixed sample to as many as six tube outlets. Reaction tubes consist of six 1.59 mm I.D. Teflon tubes with length of 2.0 m connected to each port of the solenoid valve. The other end of each tube is also connected to each port of an identical 6-channel solenoid valve (SV2). At SV2, the six tubes merge back into a single 1.59 mm I.D. Teflon tube which then further merges with a 0.79 mm I.D. Teflon that collects indigo stock solution through a peristaltic pump (Pump B) (Masterflex L/S Console Driver with Masterflex L/S Cartridge Pump Head, Cole Parmer, Chicago, IL). The combined line passes through an 80 μL volume flow-through quartz cuvette (Hellma USA, Plainview, NY) placed in a Spectronic 20D+ Spectrophotometer (Thermospectronic, Woburn, MA). To maintain a constant temperature, reactor portions of the system are immersed in a water bath (TE10D circulator, Techne, Cambridge, UK).

Operations are controlled by a set of programmable logic control (PLC) modules. Both pumps are connected to an ADAM 4521 D/A converter module (Advantech®, Taipei, Taiwan). Pumps can be toggled on and off and flow rate can be changed by this module. Both solenoid valves are connected to ADAM 4060 relay module which opens and closes each port individually. Temperature in the water bath is monitored and adjusted through an ADAM 4011 thermometer module. The analog signals from the spectrophotometer are processed by an ADAM 4017 A/D converter module. All PLC units are connected to a personal computer. A set of program codes was developed as a part of this study using the GeniDAQ software (Advantech®, Taipei, Taiwan) to control pumps, solenoid valves and water bath and to process signals from the water bath and spectrophotometer automatically. The following series of operations are performed automatically and repeatedly by the MC-SFR and control software allowing for the determination of aqueous ozone decay kinetics every 20-30 minutes.

Step 1. Determining Ozone Stock Solution Concentration. The MC-SFR operation measures the dissolved stock ozone concentrations based on the indigo colorimetric method (Bader and Hoigné, 1981). Since indigo slowly degrades over time even if kept in dark ((APHA) *et al.*, 1998), it is necessary to measure the absorbance of stock solution prior to each individual experiment. Therefore, the first step of MC-SFR operation is mixing the indigo solution and the DI water at predetermined (arbitrary) flow rates. Such a dilution with Mili-Q water is necessary to measure the absorbance of the mixture at 600 nm (A_{water}) within linear absorbance range. After flow is initiated, a lag time of 2 min is allowed to achieve a stable signal by a spectrophotometer. Ozone stock solution concentration is then measured, which may vary from experiment to experiment, by mixing the indigo solution and the ozone stock solution at the same respective flow rates. After mixing starts, a lag time of 2 min is again allowed to achieve a stable signal by a spectrophotometer and the absorbance is recorded (A_{indigo}). For A_{water} and A_{water}

measurement, the flow path was shortened by installing a by-pass line (not shown at Figure 3.1) between two static mixers to minimize ozone decay during transport. Initial ozone concentration is calculated according to the following formula:

$$[O_3] = \frac{48{,}000}{23{,}150} \times \frac{A_{water} - A_{indigo}}{f} \tag{3.1}$$

Where f = flow rate of DI water (or flow rate of sample water, which is controlled to be same) divided by the total flow rate into the spectrophotometer (i.e., flow rate of water plus that of indigo solution). The molar absorbance of indigo trisulfonate was assumed to be 23,150 cm^{-1} as suggested previously (Chiou *et al.*, 1995).

In the above and following experiments, stock solutions of dissolved ozone with concentrations ranging from 5.0 to 28.0 mg/L were prepared by bubbling gas ozone through a Mili-Q water (>20 μΩ/cm at 25°C) at a pH 5 in a 500-mL gas-washing cylinder. Ozone gas was generated by a PCI-Wedeco Model GSO 10 ozone generator (Herford, Germany) from pure oxygen. Prior to contact with the stock solution, the ozone gas was washed through a 500 mL gas washing bottle containing a 10 mM phosphate buffer solution at pH 6. Indigo stock solution was prepared following the procedure described previously (APHA *et al.*, 1998). Fresh indigo stock solution was prepared no more than 1 week prior to experiments.

Step 2. Reactor charging and Reaction Initiation. During the second step, all six reactors (i.e., 1.59 mm I.D. Teflon tubes, 2m in length, 3.96 mL in volume) are filled with a mixture of sample water and ozone stock solution driven by Pump A (Figure 3.1) at the maximum flow (71.0 mL/min). The ratio between the ozone stock solution flow rate and the same water flow rate is controlled at 0.07 (±0.001). To ensure even flow

rates and adequate flushing, the mixture is allowed to flow through the first reactor tube for 40 s. After 40 s of flushing (approximately 12 times the residence time of the reactor), the solenoid valves at both ends of the reactor are simultaneously shut off to initiate the first reaction. The residence time of the mixture inside the reactor tube during charging phase is approximately 3.3 s, which is included in the total MC SFR residence time. As soon as the valves for the reactor 1 are closed, the sample mixture is directed toward the second reactor tube for 20 s via solenoid valve 1 (SV1). After a 20 s flushing period (approximately 6 reactor volumes), the reaction for the second tube is initiated by simultaneous closing of the designated solenoid valves at each end of the reactor as done for the first reactor tube. This process is consecutively performed to the sixth reactor tube.

Step 3. Reaction. Reactions are carried out for a predetermined period under stagnant hydrodynamic conditions at controlled temperatures. For example, if reactor tubes 1 through 6 are closed for 2, 4, 6, 10, 15, and 20 min after Step 2, residual ozone concentration measurements will correspond to reaction times of 2, 4, 6, 10, 15, and 20 min respectively. After in-line ozone measurements (described below in Step 4), an ozone decay curve is then constructed using these six data points as well as the initial ozone concentration determined in Step 1. The duration of reaction in each reactor tube can be independently adjusted by the control software, allowing for temporal flexibility in kinetic analyses.

Step 4. Reaction Termination and Residual Measurement. After a predetermined reaction time is reached, the corresponding solenoid valves are opened and flow is resumed (Pump A) inside the reactor (with the reactor tube 6 being the first and reactor tube 1 being the last) via Mili-Q water (Pump A, line D) as a carrier solution. Upon elution from the reactor tube, the sample solution is then immediately mixed with indigo

solution delivered by Pump B. The ratio of sample flow rate and indigo solution flow rate used in Step 1 is maintained. As the sample solution is mixed with the indigo solution, residual ozone is quenched, terminating the reaction. This mixture is then passed through a flow through cell in a spectrophotometer to measure the absorbance at 600 nm (A_{sample}). Residual ozone concentration for each sample water is calculated according to Equation (1) with A_{water} replaced by A_{sample}.

Step 5. Signal Processing. Figure 3.2 illustrates how the signals generated by the spectrophotometer are processed by the PLC and the control software resulting in an ozone decay curve from a single experiment (i.e., one set of Steps 1 through 4). Raw voltage signals (0 - 1.0 V) directly obtained from the spectrophotometer correspond to transmittance of the samples with different reaction times as shown in Figure 3.2a. A transmittance decreases with an increase in reaction time, as residual ozone concentration decreases and less indigo is thus consumed. Analog signals are transformed by an A/D converter (Adam 4017, Advantech, Taipei, Taiwan) into digital values and further processed into absorbance signals by the GeniDAQ control software (Figure 3.2b). Ozone concentration at each reaction time is obtained according to Equation (3.1) as shown in Figure 3.2c. An average of the highest five in each peak measured over a one second interval is reported for each reaction time (e.g., reactor tube). For example, as shown in Figure 3.2, a kinetic curve with ozone concentration at t = 0 (initial ozone concentration), 1, 2, 4, 8, 12 and 16 min is constructed. Note that since each data point corresponds to one of six reactor tubes, a kinetic curve with maximum seven data points (i.e., including the initial point) is possible with the current design of MC-SFR during a single set of experiment (a single set of Step 1 through Step 4).

3.3. Instrument Parameter Optimization

Prior to measuring ozone decay kinetics, tracer tests were performed to optimize the key design parameters that might affect the mixing conditions during fluid transport. Indigo trisulfonate was used as a non-reactive tracer in the absence of ozone. Unless stated, conditions were the same as described above except replacing reactive ozone with Mili-Q water. Parameters tested included reactor tube length (0.2 to 2.0 m) and diameter (1.59 mm and 7.93 mm I.D.), sample flow rate (16.6 to 39.4 mL/min) and indigo flow rate (30.0 to 47.4 mL/min). Experimental results (not shown) suggested that the length of tube needs to be at least 1.2 m in order for the spectrophotometer to retrieve stable absorbance signals. Tubes with I.D. of 1.59 mm were determined to be optimal between the sample collection and the indigo injection point and tube I.D. of 0.79 mm, was better suited for input into the flow-through cell. Tubes with higher flow rates and smaller I.D. were preferred to reduce dispersion and enhance the mixing before the flow-through UV cell (Růžička, 1988). Higher flow rates in general resulted in more stable readings by spectrophotometer due to possibly lower dispersion under these conditions while exceedingly high flow rates decreased in sensitivity as a variable and became wasteful with regard to reagents. Under these described conditions, optimal flow rates of sample and indigo solutions for stable signals were identified at 16.6 mL/min and 39.4 mL/min, respectively.

3.4. Instrument Verification and Application

Applicability of the MC-SFR system was verified using several different sample waters by evaluating precision and accuracy of the measurements. Figure 3.3 illustrates representative ozone decay kinetics in organic-free, synthetic water obtained with the MC-SFR. The synthetic water for this experiment was prepared by decarbonating Mili-Q water with scientific-grade nitrogen for 30 min followed by adding predetermined amounts of 0.1 M NaH_2PO_4, Na_2HPO_4, and $NaHCO_3$ stock solutions to achieve pH 7.5 and total phosphate ($C_{T,PO4} = [H_2PO_4^-] + [HPO_4^{2-}]$) and total carbonate ($C_{T,CO3} = [HCO_3^-]$

+ $[CO_3^{2-}]$) concentrations of 10^{-3} and 10^{-4} M, respectively. Identical kinetic experiments aimed at evaluating instrument precision were performed independently five times. At a constant temperature of 20°C, each data point in Figure 3.3 represents an average value of five independent experiments with a corresponding error bar. For all the data points shown, the standard deviations were very small and ranged from 0.014 to 0.031 mg/L.

Further experiments were performed using the synthetic waters at pH 6.5, 7.5 and 8.5 with $C_{T,PO4} = 10^{-3}$ M and $C_{T,CO3} = 10^{-4}$ M. Temperature was controlled at 20°C. Each ozone decay curve at different pH values in Figure 3.4 was constructed from two independent experiments performed with different sets of reaction times. The first experiment had the reaction times of 1, 3, 5, 8, 12 min and the second experiment with 2, 4, 6, 10, 14 min. These two sampling schemes were chosen to demonstrate the flexibility of MC-SFR system to build a single decay curve by combining two or more kinetic experiments (operated under the same conditions). Since the experiments are performed automatically and repetitively, the kinetic curves with a large number of data points, extending beyond the seven points of a single experiment, could easily be constructed as shown in this figure. These specific experimental conditions were chosen to compare with the previously reported ozone decay kinetics. Batch data in Figure 3.4 was shown for comparison purpose from Kim *et al.* (2005), in which ozone decay in identical synthetic waters were measured using a headspace-free, gas-tight syringe batch reactor designed operated with a high level of control (Kim *et al.*, 2004). The resulting comparison demonstrates the accuracy of the MC-SFR as the independently derived kinetic decay curves are virtually identical.

The kinetic curves in Figures 3.3 and 3.4 were further compared with an ozone decay mechanistic model previously developed by (Kim *et al.*, 2004) based on (Bühler *et al.*, 1984; Christensen *et al.*, 1982; Forni *et al.*, 1982; Sehested *et al.*, 1984; Sehested *et*

al., 1983; Staehelin *et al.*, 1984; Staehelin and Hoigné, 1982). Reactions involving carbonate and carbonate radicals were based on (Buxton and Elliot, 1986; Buxton *et al.*, 1988; Czapski *et al.*, 1999). Overall, the model matched reasonably well with the experimental data with similar levels of deviation observed in the past studies. A slight under prediction was observed when ozone decay was faster (*i.e.*, kinetics in Figure 3.3 and pH 8.5 kinetics in Figure 3.4), which was consistent with the previous observations and might be indicative of limitations of the current mechanistic model in accurately predicting ozone decay in organic-free waters (Kim *et al.*, 2004).

Additional experiments were performed using decarbonated synthetic water that contained $C_{T,PO4} = 10^{-3}$ M and 2 mg/L of model organic matter, as Suwannee River NOM purchased from the International Humic Substance Society. An aliquot of 0.5 μM of *p*-chlorobenzoic acid (*p*CBA) was spiked as a probe compound for the purpose of measuring hydroxyl radical exposure during ozone decay. In addition, *t*-butanol at 10^{-4} M was added as a radical scavenger to obtain measurable ozone decay and *p*CBA decay kinetics within the experimental time frame. Figure 3.5 shows ozone decay curves as determined by the MC-SFR at adjusted pH values of 6.5, 7.5, and 8.0 at a reaction temperature of 20°C. Each decay curve was built with data from two independent experiments with different reaction time sets. After the initial fast decay of ozone during the first two minutes, ozone decay followed first-order kinetic law which is commonly assumed for natural waters (Singer and Hull, 2000; Kim *et al.*, 2002) with k_D = 0.034, 0.079, and 0.23 min^{-1} for pH 6.5, 7.5 and 8.0 respectively. In this case, initial fast decay of ozone in the model natural water was not instantaneous but rather gradual. This transition from fast to slow kinetics has been observed in natural water samples in previous studies and transition time depends on the water constituents. However, if instantaneous ozone decay is assumed, as is commonly done in contactor operation and if the first-order kinetics fitted to the later portion of the decay curve is taken for the entire

reaction, the *CT* for the sample water during the first two minutes of exposure would be 1.8, 1.6, and 1.3 mg/L for pH 6.5, 7.5, and 8.0, respectively. Alternatively, the ozone decay curve could be analyzed assuming that ozone decay is the result of combined effect of second order reaction with fast ozone demand which dominates initial phase and the first-order decay:

$$\frac{d[O_3]_l}{dt} = -k_D[O_3]_l - k_R[D]\cdot[O_3]_l \tag{3.2}$$

$$\frac{d[D]}{dt} = -k_R[D]\cdot[O_3]_l \tag{3.3}$$

Following the simple regression analysis described in (Kim *et al.*, 2006), resulting fitted curves with k_R = 1.79, 1.62, and 1.37 L/mg-min at pH 6.5, 7.5 and 8.0 and the same k_D values, which are also shown in Figure 3.5. The *CT* calculated during the first two minutes of exposure based on this approach was 2.2, 2.0 and 1.7 mg-min/L for pH 6.5, 7.5, and 8.0, respectively. This is noteworthy as the assumption of instantaneous initial fast decay would result in 17, 21, and 25% of underestimation of CT for pH 6.5, 7.5 and 8.0, respectively.

Characterizing the initial phase of ozone decay is also important when the level of hydroxyl radical exposure is considered. Experimental data shown in Figure 3.6 was obtained by sampling for *p*CBA at the outlet of the MC-SFR system for the same experiments described in Figure 3.5. In this case, the MC-SFR served as a reactor to examine the reaction kinetics of *p*CBA consumption which corresponds to exposure to hydroxyl radical concentration. Concentrations of *p*CBA were determined with a HPLC 1100 series system (Agilent, Palo Alto, CA) using a Zorbax eclipse XDB-C8 column, following the method by described elsewhere (Elovitz and von Gunten, 1999). The

variable R_{ct} in Figure 3.6 is defined as the exposure ratio of hydroxyl radical to ozone and mathematically expressed according to Elovitz *et al*. as follows (Elovitz and von Gunten, 1999):

$$R_{ct} = \frac{\int [\cdot \mathrm{OH}]dt}{\int [\mathrm{O_3}]dt} = \frac{\ln([p\mathrm{CBA}]/[p\mathrm{CBA}]_0)}{-k_{\cdot OH/pCBA} \times \int [\mathrm{O_3}]dt} \tag{3.4}$$

While the plot of ln([*p*CBA]/[*p*CBA]$_0$) versus $\int [\mathrm{O_3}]dt$ results in linear plot during the later phase of ozonation and the hydroxyl radical concentration is proportional to ozone concentration with a constant value (*i.e*., constant slope in Figure 3.6 and [·OH] is equal to $R_{ct} \times [\mathrm{O_3}]$), it is apparent that the slope exhibited a gradual change during the initial phase. In an attempt to estimate R_{ct} values from the slope of this non-linear curve, the curves were simply (and arbitrarily) divided into sections with linear regions. For example, one can estimates that the R_{ct} changes from approximately 1.2×10^{-7} during the fist 20 s of the reaction then decreases to 4.6×10^{-9} having a transition period of approximately 1.6×10^{-8} at pH 6.5 during a period between 20s to 2 min of ozone decay. At higher pH of 8.0, the apparent third phase in the curve might not have been reached but the same trend of increasing R_{ct} as the reaction proceeded was observed. If initial phase of *p*CBA decrease were assumed instantaneous, as has been done in previous studies (Elovitz and von Gunten, 1999; Kim *et al.*, 2006), some level of underestimation of hydroxyl radical exposure, by possible orders of magnitude, during initial phase of ozone exposure would result. Such an effect might play a critical role in estimation of disinfection by-product concentration as hydroxyl radical can significantly contribute to bromate formation (von Gunten and Hoigné, 1994). High levels of hydroxyl radical exposure during the initial phase, which has not been well characterized by previous

batch experiments due to sampling limitations, may have partly attributed to apparent fast or near instantaneous formation of bromate in some natural waters (Kim *et al.*, 2006).

3.5. Conclusion

A highly controlled MC-SFR system that mechanically separates the reaction fluid element providing preferred batch reaction conditions and while maintaining flow-through reactor advantages was developed and verified. This instrument was specifically designed to obtain the ozone decay kinetics for the range of reaction times relevant to water treatment (*i.e.*, up to a few tens of minutes) as well as that for relative short period of reaction time that might be important in accurately estimating ozone and radical exposure during initial phase of ozonation. These kinetics evaluations can be performed automatically and a near continuous manner. High levels of instrument accuracy and precision were observed along with flexible applicability in regard to both reaction times (*i.e.* seconds to minutes) and analyses (*i.e.* residual ozone and *p*CBA concentrations) as demonstrated with laboratory synthetic waters. For contactor optimization based on reliable ozone decay kinetic data, which is essential for accurate CT estimation and/or input into predictive models, such a MC-SFR design could prove very useful in practice, for example, as a viable alternative to a side-stream pipe system which relies on extended CSTR calculations (Rakness *et al.*, 2005).

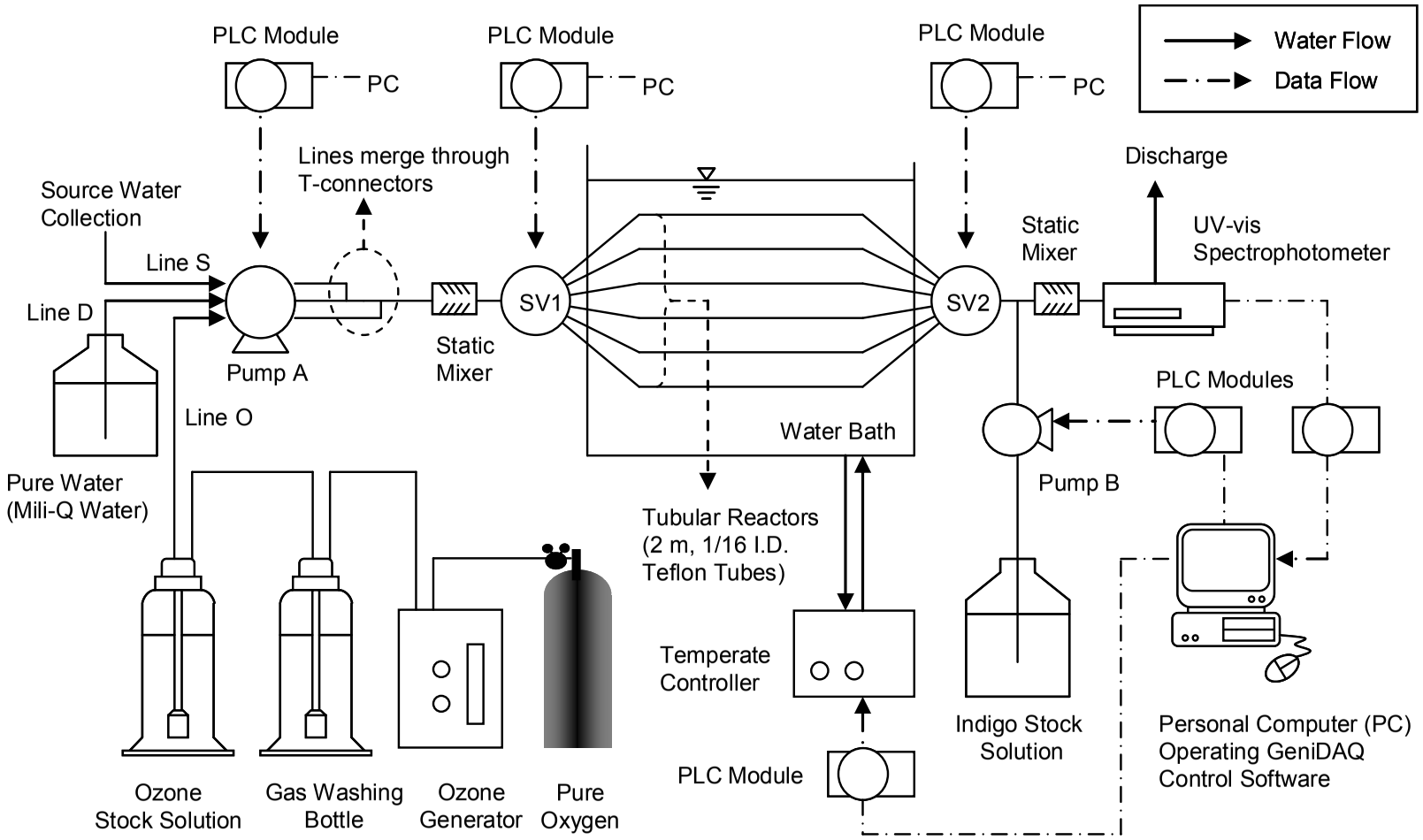

Figure 3.1. A detailed schematic representation of a multi-channel stopped-flow reactor (MC-SFR) system

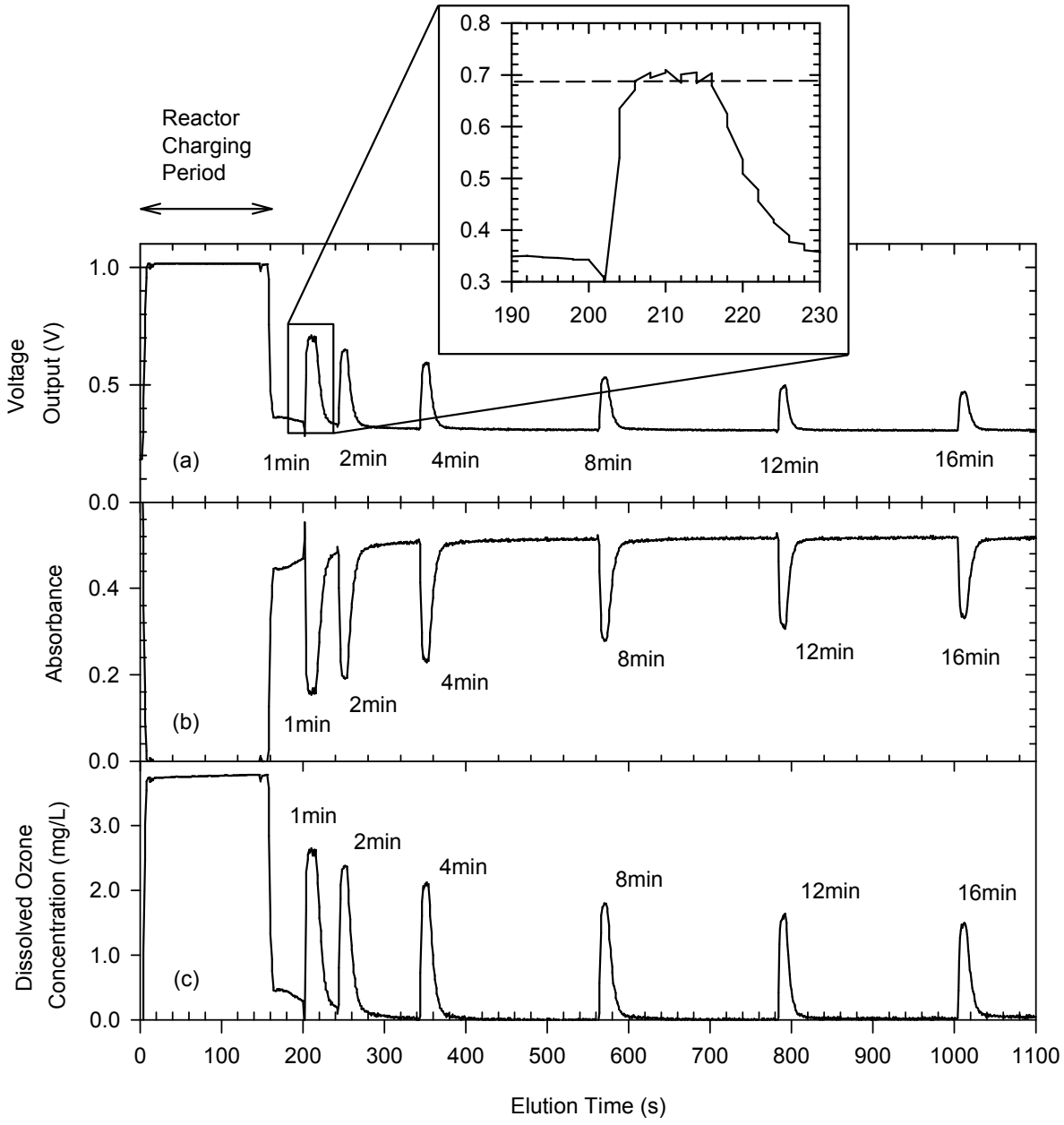

Figure 3.2. A process of raw data analysis by the MC-SFR for ozone decay in a model water: (a) raw voltage signals from the spectrophotometer, (b) absorbance of residual indigo, and (c) residual ozone concentrations at different reaction times.

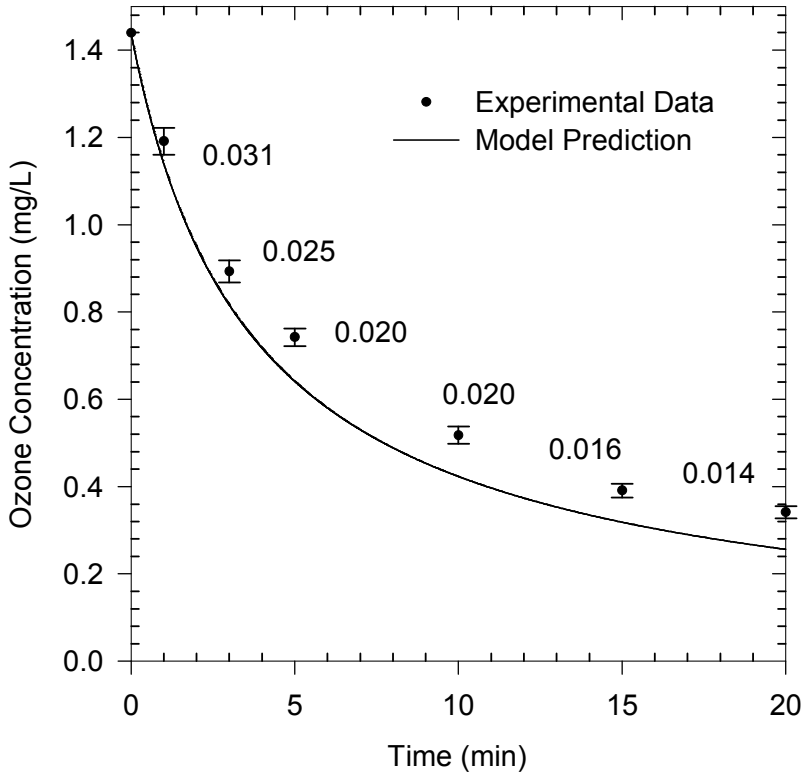

Figure 3.3. Ozone decay kinetics obtained from five independent runs of the MC-SFR with error bar and standard deviation for each data point and a corresponding model prediction ($[O_3]_0$ = 1.4 mg/L, pH = 7.5, $C_{T,\,PO4} = 10^{-3}$ M, $C_{T,\,CO3} = 10^{-4}$ M, 20°C).

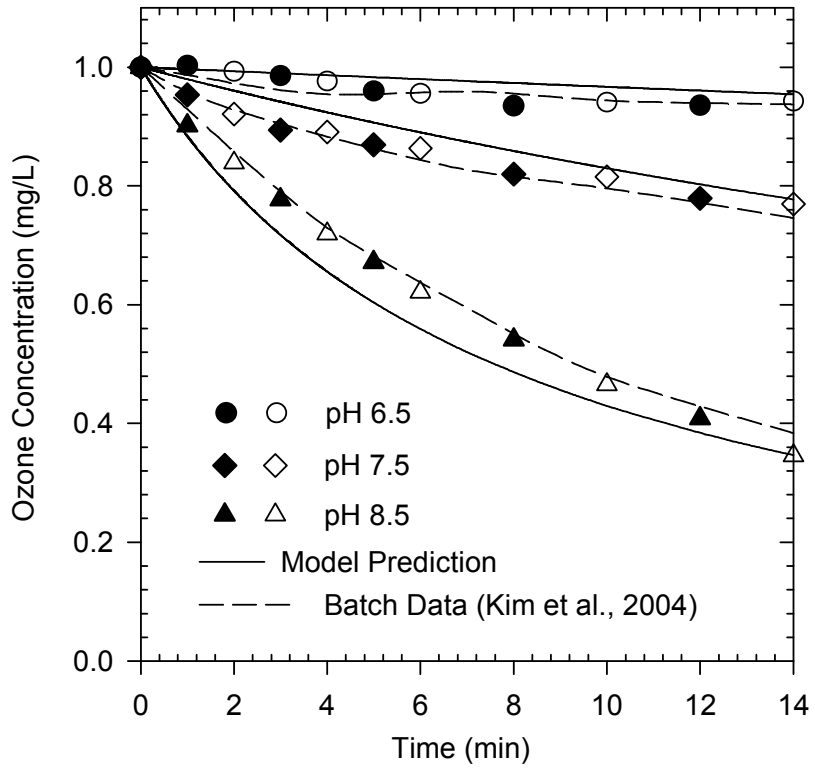

Figure 3.4. Ozone decay kinetics obtained from two independent runs of the MC-SFR for each organic-free solution at different pH. ($[O_3]_0$ = 1.0 mg/L, pH = 6.5, 7.5, and 8.5, $C_{T, PO4} = 10^{-3}$ M, $C_{T, CO3} = 10^{-4}$ M, 20°C).

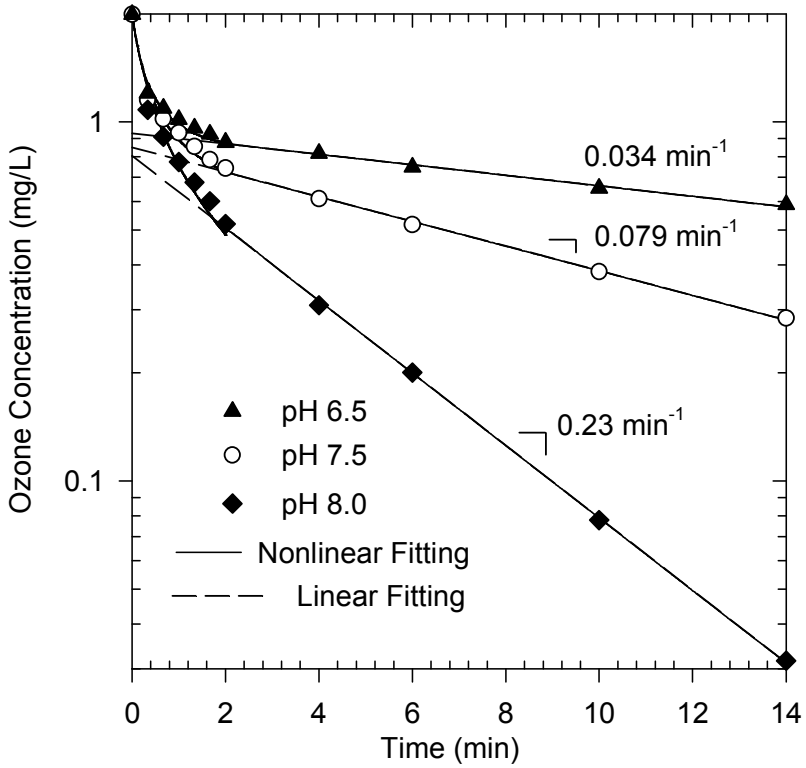

Figure 3.5. Ozone decay kinetics obtained from two independent runs of the MC-SFR for each model natural water at different pH. ($[O_3]_0$ = 2.0 mg/L, [SRNOM] = 2.0 mg-C/L, pH = 6.5, 7.5, and 8.0, $C_{T,PO4} = 10^{-3}$ M, [*t*-Butanol] = 10^{-4} M, [*p*CBA] = 5×10^{-6} M, 20°C).

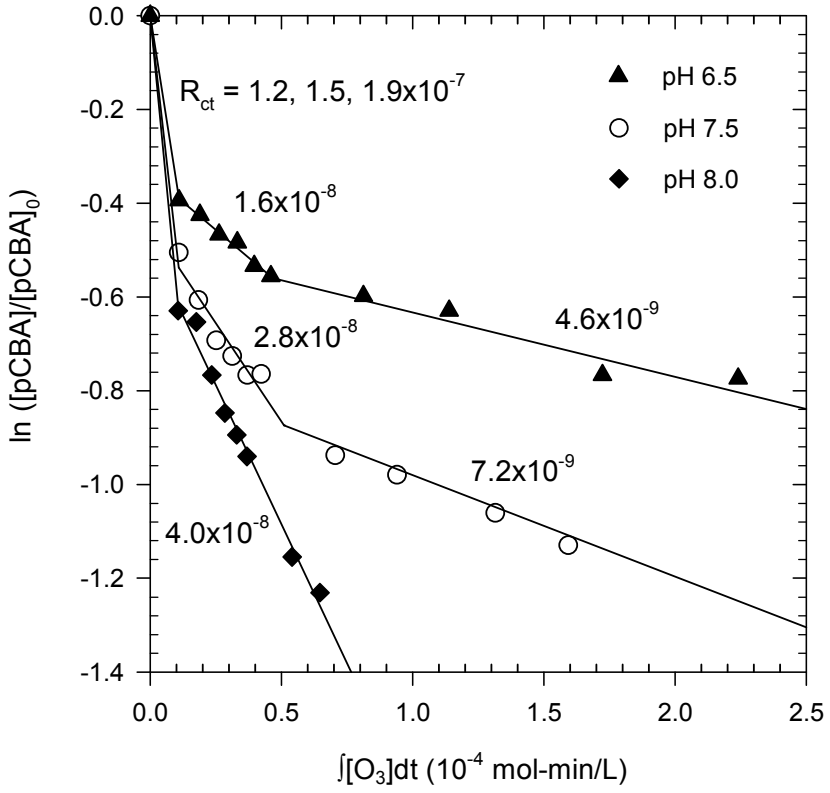

Figure 3.6. *p*CBA decay kinetics in the model natural water for the same experimental conditions in Figure 3.5.

CHAPTER 4

SIMULTANEOUS SIMULATION OF PATHOGEN INACTIVATION AND BROMATE FORMATION IN FULL-SCALE OZONE CONTACTORS BY COMPUTER SOFTWARE

4.1. Introduction

The presence of the pathogen *Cryptosporidium parvum* in drinking water is of major concern and is addressed in the recent Long Term 2 Enhanced Surface Water Treatment Rule (USEPA, 2006a). Although ozone is most effective in treating *C. parvum* oocysts among chemical disinfectants (Gyürék *et al.*, 1999; Rennecker *et al.*, 1999, 2000; Driedger *et al.*, 2000, 2001), its wide application has often been limited by formation of bromate (BrO_3^-) from bromide (Br^-). Due to the prevalence of bromide in natural waters (USEPA, 2003), the regulatory level of 10 μg/L specified for bromate in the recent Stage 2 Disinfectants and Disinfection Byproducts Rule (USEPA, 2006b) might be challenging to meet for many water treatment utilities practicing ozonation. Therefore, much research has been focused on balancing *C. parvum* oocyst inactivation and bromate formation in ozone disinfection processes (Pinkernell and von Gunten, 2001; Kim *et al*., 2004; Kim *et al*., 2005; Tang *et al*., 2005). These studies suggested that, in addition to water quality parameters such as pH and concentration of ammonia, mixing conditions in the ozone contactor might also play a critical role in achieving sufficient level of *C. parvum* oocyst inactivation with minimal production of bromate.

Predictive models have been proposed as a promising tool to balance *C. parvum* oocyst inactivation and chemical reactions leading to bromate formation that are coupled with complex hydrodynamic and mass transfer processes in ozone contactors. Recent work by Kim *et al*. (2002a, 2002b, 2005) has successfully demonstrated that the one-dimensional axial dispersion reactor (ADR) model accurately represents the dissolved

ozone concentrations and *C. parvum* oocyst inactivation levels in both lab- and pilot-scale flow-through ozone bubble-diffuser contactors. This model was further developed by Tang *et al*. (2005) to simultaneously account for bromate formation in a full-scale ozone contactor. The validity of this ADR-based predictive model has been confirmed by full-scale experiments for dissolved ozone concentration, bromate formation, and *C. parvum* oocyst inactivation (*i.e.*, using fluorescence-dyed microspheres as surrogate for *C. parvum* oocysts) (Tang *et al*., 2005).

A user-friendly *Ozone Contactor Model* (*OCM*) software based on the abovementioned predictive models (Kim *et al*., 2002a, 2002b, Kim *et al*., 2005, Tang *et al*., 2005) was developed in the present study. The *OCM* is targeted for engineers involved in the design and operation of ozone disinfection systems, plant operators responsible for optimizing system operation and demonstrating regulatory compliance, and government officials in charge of developing drinking water regulations who are not necessarily familiar with formulations and numerical analyses involved in these mathematical models. The *OCM* software is designed to work on a personal computer equipped with Microsoft Windows® (*i.e.*, Windows 2000® or higher version) and to provide graphical user interfaces that are familiar to Windows users.

The *OCM* software performs simulation of full-scale ozone bubble-diffuser contactor performance in drinking water treatment. Specifically, the software is capable of simultaneously predicting the distributions of dissolved ozone concentration, inactivation efficiency of pathogenic microorganisms such as *C. parvum* oocysts, and bromate formation throughout ozone contactors. The *OCM* software provides simulation results as profiles throughout the ozone contactor (*i.e.*, at any location within the reactor) and has the capability of comparing the available field data to as many as five model predictions obtained under different design configuration and operating condition options to available field data. The *OCM* software also allows performing simulations for any

pathogenic microorganism, other than *C. parvum* oocysts for which the corresponding ozone inactivation kinetic data is available.

The purpose of this paper is to introduce the newly developed *OCM* software and demonstrate its application with a case study on the full-scale ozone contactors of the Linnwood Water Plant Ozone Facility (LWPOF) at Milwaukee Water Works, Milwaukee, WI. Ozone and bromate concentrations obtained from full-scale experiments were compared with the model simulation results. The predictions were performed with ozone decay and bromate formation kinetic parameters obtained from separate bench-scale tests performed with the source water. The *OCM* software was also used to predict the level of *C. parvum* oocyst inactivation. Additional model simulations were performed to illustrate how the *OCM* software can be used for plant design and optimization.

4.2. *OCM* Software – Background and Usage Guidance

Table 4.1 summarizes the steady-state governing equations for the concentrations of dissolved ozone, fast ozone demand (*i.e*. portion of water constituents that consumes dissolved ozone at a relatively fast rate during initial phase of ozonation), gas phase ozone, viable microorganisms, and bromate employed in the *OCM* software. The following assumptions were made to formulate these equations: 1) hydrodynamics in each chamber of the ozone contactor can be represented with the one-dimensional ADR model (Kim *et al*., 2002a, 2002b; Kim *et al*., 2005; Tang *et al*., 2005), 2) dissolved ozone decays according to a first-order rate law after a relatively faster initial loss by a second order reaction with fast ozone demand (Lev and Regli, 1992; Chen, 1998), 3) bromate formation increases in proportion to *CT* (*i.e.*, exposure or integrated to dissolved ozone concentration over time) (Tang *et al*., 2005), and 4) pathogen inactivation curves can be represented with a pseudo-first order Chick-Watson kinetic law either in the presence or absence of initial lag phase (Rennecker *et al.*, 1999; USEPA, 2006a). This group of equations was solved for each chamber of the ozone contactor assuming ideal closed

vessel boundary conditions (Kim *et al*., 2002a) at each boundary between adjacent chambers. These boundary conditions are summarized in Table 4.2. Numerical integration was performed following the algorithm previously described by Kim *et al*. (2002a). Mass transfer coefficient, k_La, and Henry's law constant for ozone, m, at different temperatures were obtained using the empirical equations also previously described by Kim *et al*. (2002a).

Figure 4.1 shows a snapshot of the *OCM* software running on the Microsoft Windows® XP operating system. The software is designed to be user-friendly and consistent with most other Windows® applications. The software consists of a menu, tool bar, document space, and several dialog boxes (shown in Figure 4.1) for input of site-specific parameters necessary for simulations. These required parameters are summarized in Figure 4.2 and described in subsequent sections.

Source water characteristics. The user specifies the name of the source water, concentration of fast ozone demand ($[D]_0$), second order rate constant between fast ozone demand and dissolved ozone (k_R), first-order ozone decay rate constant (k_D) at specific temperature, bromate formed by initial fast reaction ($[BrO_3^-]_0$) and bromate formation rate constant (k_{BrO3-}) at a specific temperature using the *Source Water Characteristics* dialog box shown in Figure 4.1. Activation energies for ozone decay and bromate formation are required if model simulation is to be performed at different temperatures. These parameters should be obtained from independent bench-scale batch experiments as described in a subsequent section.

Ozone Contactor Configuration. Designing an ozone contactor in the *OCM* software involves the use of three different dialog boxes (Figure 4.1). In the first dialog box, *Contactor Configuration Dialog Box*, the user can specify the contactor name, total number of chambers, total design volume, design flow rate, and operating temperature.

Next, the volume, cross-sectional area, flow direction, and dispersion number for each chamber are input in the *Chamber Configuration Dialog Box*. Then, contacting chambers where the ozone bubbles are applied are specified and the corresponding gas flow rate, inlet gas phase ozone concentration, and average diameter of ozone bubbles are inserted in the *Diffuser Configuration Dialog Box*.

Microorganism Kinetics. The *OCM* software provides a tool to manage the database for the inactivation kinetics of various microorganisms. In the *Target Microorganism Dialog Box*, the user can specify the name of the microorganism, inactivation rate constant, and other relevant information such as the strain of microorganism used for the kinetics experiments, experimental method and conditions by which inactivation kinetics were determined, and the reference can be recorded. From the drop down menu, the users can select the target microorganisms for each simulation run.

Once all the necessary information is provided and the simulation is completed, the simulation results are automatically presented in the document window as illustrated in a subsequent section. The names of source water and ozone contactor first appear in the uppermost part of the window followed by three graphs, ozone concentration profile, microorganism inactivation level profile, and bromate concentration profile, respectively from top to bottom. Values are plotted versus the normalized cumulative volume of the contactor. Normalized cumulative volume is defined as the volume up to a selected point from the inlet of the contactor divided by the total volume of the contactor. Vertical lines inside each graph show the separation between chambers. As many as five individual simulation results can be compared to any set of experimental data using a *Plot Data Dialog Box* and an *Experimental Data Dialog Box* (Figure 4.1).

4.3. Experimental Methods

Bench-Scale Batch Experiments. The kinetics of ozone decay and bromate formation in the target source water (*i.e.*, Lake Michigan Water) were obtained by performing bench-scale experiments using a water sample from the LWPOF collected the day of the field experiments. Relevant water quality parameters of the source water were: pH = 8.0, bromide = 24.8 μg/L, total organic carbon concentration = 1.94 mg/L, turbidity = 0.07 NTU, and alkalinity = 102 mg/L as $CaCO_3$. Batch experiments were performed using a recently developed Multi-Channel Stopped-Flow Reactor (MC-SFR) (Kim *et al.*, 2005). The MC-SFR automatically measures ozone decay kinetics and serves as a batch reactor to determine bromate formation kinetics. Briefly, ozone stock solution was prepared by bubbling the ozonated gas prepared from pure oxygen using a Wedeco Model GSO 10 ozone generator (Herford, Germany) through Mili-Q water of pH 5 (adjusted by adding H_2SO_4) in a 500-mL gas-washing cylinder. The stock solution was nearly instantaneously mixed with the source water at a ratio of 0.097 to 0.1 and transferred into the reactor. After allowing the reaction to proceed for a predetermined amount of time, the solution was instantaneously mixed with potassium indigo trisulfonate solution and ozone residual was measured at different reactions times (2, 4, 6, 10, 15 min) by a modified version (Chiou *et al.*, 1995) of the indigo colorimetric method (Bader and Hoigné, 1981). For bromate concentration analysis, 2-3 mL of samples were mixed with a 0.1 mL of 0.5 M ethylenediamine solution. Processes involving stock solution transport, reaction initiation and termination, absorbance measurement, and sample collection were executed automatically and repeatedly by the MC-SFR. Concentrations of bromate and bromide ions were measured by ion chromatography according to EPA method 317.0 (USEPA, 2001). Experiments were first performed at 7^{o}C, a temperature at which the full-scale experiments were performed, with an initial ozone concentration of 1.0 mg/L. Additional experiments were performed at 20^{o}C with initial ozone concentration of 2.0 mg/L.

Field Experiments. The LWPOF is equipped with four identical ozone contactors, each consisting of twelve chambers. A schematic of the cross-section of one of the ozone contactors is shown in Figure 4.3. The overall contactor volume is 128,000 ft^3 or 0.957 MG. The first (8,280 ft^3 or 0.062 MG) chamber is equipped with 83 ceramic bubble diffusers installed at the bottom, and serve as a contacting chamber. The contacting chamber is operated in a counter-current mode (*i.e.*, water flowing downward). The following 11 chambers are identical in volume (11,282 ft^3 or 0.084 MG each) except for the fifth (6,840 ft^3 or 0.0512 MG) and water flows in alternating directions, either upward or downward, and serve as reactive chambers.

Tracer tests were performed with all four contactors at several combinations of water and gas flow rates using fluoride ion as a conservative tracer. Experimental conditions for the tracer tests are summarized in Table 4.3. A tracer test was started by injecting a pulse input containing approximately 4,500 g of fluoride ion at the inlet of the ozone contactor. The concentration of fluoride was measured at the sampling point located at the 10th chamber of the contactor by the EPA Method 300.1 (USEPA, 1997) using an ion chromatography system (Dionex, Sunnyvale, CA). The samples were taken at 1.5 to 4 min intervals for a period of time approximately 2.5 times the theoretical hydraulic residence time.

Three replicate ozonation experiments were performed using contactor #1 to obtain dissolved ozone and bromate concentrations during steady-state operation. Experiments were performed at the following conditions: water flow rate = 29.5 ± 0.2 MGD; gas flow rate = 15.1 ± 0.4 scfm; gas phase ozone concentration = 12.4 ± 0.005 %w/v (*i.e.*, 174 mg/L); water temperature = 7.0 ± 0.02^oC; and gas temperature = 16.6 ± 0.01^oC. Ozone gas was introduced into the first chamber at a flow rate of 15.1 standard cubic feet per minute (scfm). Inlet gas phase ozone concentrations were measured by a PCI-Wedeco

Ozone Monitor (West Caldwell, NJ). Water samples were taken at sampling ports located at 2nd, 5th, 10th, 12th chambers and dissolved ozone concentrations were measured by an Orbisphere Laboratories Dissolved Ozone Monitor (Geneva, Switzerland). Samples for bromate analysis were collected at all the sampling ports available (1st, 2nd, 4th, 5th, 6th, 8th, 10th, and 12th chambers). Bromate concentrations were measured by the EPA Method 326.0 (USEPA, 2002) using a Dionex Ion Chromatograph Model DX-500 (Sunnyvale, CA).

4.4. Results and Discussion

4.4.1. Batch Experimental Results and Kinetic Analysis

Figure 4.4-a) shows ozone decay curves determined experimentally at 7°C (*i.e.*, water temperature at which full-scale experiments were performed) and 20°C. Ozone decay curves were characterized by initial faster decay followed by slower first-order decay, which can be mathematically represented as:

$$\frac{d[O_3]_l}{dt} = -k_D[O_3]_l - k_R[D]\cdot[O_3]_l \tag{4.12}$$

$$\frac{d[D]}{dt} = -k_R[D]\cdot[O_3]_l \tag{4.13}$$

In order to obtain the unknown parameters (*i.e.*, k_D, k_R, and $[D]_0$) from the experimental results, the following steps were developed: 1) determine k_D from the slope of the linear part of the experimental curve when logarithmic concentrations were plotted versus time (*i.e.*, using the data points at 6, 10, and 15 min for both temperatures); 2) determine the amount of fast ozone demand ($[D]_0$) from the intercept of the same line; 3) solve Equations (4.12) and (4.13) simultaneously by a stepwise integration. The numerical integration (*e.g.*, between time t_i and t_{i+1}) could be performed as follows:

$$\Delta[O_3]_t = [O_3]_{t,t_{i+1}} - [O_3]_{t,t_i} = (-k_D[O_3]_{t,t_i} - k_R[D]_n[O_3]_{t,t_i}) \times \Delta t \quad (4.14)$$

$$\Delta[D]_t = [D]_{t,t_{i+1}} - [D]_{t,t_i} = (-k_R[D]_{t_i}[O_3]_{t,t_i}) \times \Delta t \quad (4.15)$$

where $\Delta t = t_{i+1} - t_i$. Then k_R that results in the lowest least-square deviations of the model curve from the experimental data can be found by a trial-and-error approach. This method was based on the assumption that contribution by the fast ozone demand to overall ozone decay becomes negligible after passing the initial fast loss period. This approach, which could be performed relatively easily with a commercially available spreadsheet program, was developed to obtain a unique and fairly accurate estimate of kinetic parameters without complex numerical optimization algorithms. Resulting fitted values were k_D = 0.039 min^{-1}; k_R = 0.34 L/(mg-min); and $[D]_0$ = 0.20 mg/L at 7^{o}C; and k_D = 0.055 min^{-1}; k_R = 0.17 L/(mg-min); $[D]_0$ = 0.50 mg/L at 20^{o}C.

Figure 4.4-b) shows bromate concentrations versus *CT* (*i.e.*, exposure to ozone concentration over time) determined from batch experiments at 7^{o}C and 20^{o}C. The *CT* values were calculated by integrating the ozone decay experimental curves in Figure 4.4-a) using a trapezoidal rule. In general, bromate concentration linearly increased as *CT* increased, but a closer inspection suggested that there was an initial fast formation of bromate at relatively low *CT*s (*i.e.*, *CT*s up to 5 and 6.5 mg-min/L for 7^{o}C and 20^{o}C data, respectively) followed by a slight decrease in the formation rate. Initial faster formation of bromate might be related to the initial faster decay of ozone due to the reaction with fast ozone demand. As the fast ozone demand is consumed during the initial stage of ozonation, the concentration of hydroxyl radical may increase as a result of the reaction of ozone with organic matter (Elovitz and von Gunten, 1999). Consequently, higher concentration of hydroxyl radical during this phase could enhance the bromate formation. For modeling purposes, a single line was fitted to each set of data. The slope of the fitted lines were 0.24 μg BrO_3^-/(mg O_3-min) at 7^{o}C and 0.62 μg BrO_3^-/(mg O_3-min) at 20^{o}C. Note that the lines did not go through the origin, and they intercepted the y-axis at 0.2 μg-

BrO_3^- at 7°C and 1.7 μg-BrO_3^- at 20°C. The level of bromate at *CT* = 0 in batch experiments was assumed to correspond to relatively instantaneous formation of bromate in the inlet of the full-scale ozone contactor (*i.e.*, initial formation, or $[BrO_3^-]_0$ in the *Source Water Characteristics* dialog box).

4.4.2. Full-Scale Demonstration

Experimental tracer curves obtained with the four ozone contactors in the LWPOF are shown in Figure 4.5. Each tracer curve was analyzed to obtain a corresponding dispersion number, *d*, following the methods previously described by Tang *et al*. (2005). It was found that the experimental tracer curves could not be matched with model simulations until dispersion numbers were assumed to be very high. This observation suggested that hydrodynamics in each chamber was close to that in an ideal continuous-flow stirred tank reactor (CSTR). Accordingly, the portion of the reactor in which the tracer tests were performed (*i.e.*, 1st to 10th chambers) was best represented with a series of 10 CSTRs (note that tracer tests were performed for 1st to 10th chambers). Because each chamber is represented with the ADR model in the *OCM* software, the CSTR cascade was simulated by using a high dispersion number (*d* = 10,000). The resulting model predictions for the tracer curves are compared to the experimental data in Figure 4.5. As depicted in the figure, there was generally good agreement between experimental data and model predictions. A slight misorientation in the center of the tracer curves resulted since the overall contactor volume used in model prediction did not account for the volume displaced by the baffle walls. It is estimated that the theoretical hydraulic residence time was overestimated by approximately 5% which was considered minor for the purpose of this study. No difference could be observed when plotting the tracer curves corresponding to an ideal CSTR cascade and those based on the ADR model using *d* = 10,000, and therefore this dispersion number was found to be adequate and was used for all predictions presented subsequently.

Figure 4.6 shows the actual window display of the *OCM* software demonstration run for contactor #1 at LWPOF. The experimental data obtained from the field tests are shown with open circles. Model predictions obtained using 1) the kinetic information determined from the batch tests, 2) dispersion number determined from the tracer tests, and 3) the reactor configuration and operation conditions collected from the field, are also plotted as red solid lines. The model predictions were in an excellent agreement with the experimental data for ozone. Bromate concentrations in the contactor effluent were underestimated by up to 13%. These levels of deviation are considered within experimental error taking into account possible errors in bromate concentration from sampling and analysis in both batch and full-scale tests, as well as limitations of the current model in accurately representing bromate formation kinetics especially at the early stage of ozonation when bromate is formed at a relatively faster rate.

The inactivation level of *C. parvum* oocyst, also predicted by the model is shown in the middle plot of Figure 4.6. Note once again that inactivation efficiency predicted by this model has been verified experimentally in previous studies (Kim *et al*., 2002a, 2002b, Kim *et al*., 2005, Tang *et al*., 2005). In this study, a pseudo-first order Chick-Watson expression (*i.e.*, without an initial lag phase) with a second order inactivation rate constant, k_N in L/(mg-min), corresponding to *CT* requirements in the LT2ESWTR (USEPA, 2006a) was used to represent the inactivation kinetics of *C. parvum* oocysts with ozone:

$$k_N = 0.0917 \times 1.097^T \tag{4.14}$$

where T = temperature (^oC). The *OCM* simulation results suggested that the LWPOF would achieve overall *C. parvum* oocyst inactivation level approximately at 1.07 logs (91.5%) at 7^{o}C. Note that the value of CT_{10} calculated by multiplying average ozone

concentration and T_{10} (*i.e.*, the time required for ten percent of the fluid elements to reach the chamber outlet) equals 10.2 mg-min/L. This CT_{10} value, if applied to a plug-flow of *C. parvum* oocysts (*i.e.*, calculated using the Chick-Watson kinetic expression), would result in 0.78 log (83%) inactivation of *C. parvum* oocysts using the rate constant given by Equation (4.14). If theoretical hydraulic residence time is used instead of T_{10}, the CT value equals 16.0 mg-min/L which would result in 1.22 log (94%) inactivation. This finding suggests that CT_{10} is a conservative design parameter and would result in a significant underestimation of inactivation efficiency and consequently significant over-design of the system capacity. On the contrary, the prediction without accounting for the back-mixing of *C. parvum* oocysts would lead to overestimation of inactivation efficiency or under-design of the capacity.

4.4.3. Software Application

Additional model simulation results obtained using the kinetic information at 20°C are also shown in Figure 4.6 (blue solid lines). These predictions were obtained using the ozone decay and bromate formation kinetic parameters determined from the batch tests performed at that temperature, and assuming that the contactor operating conditions were the same as those at the lower temperature. Consistent with the previous observation by Kim *et al*. (2002b), dissolved ozone concentration decreases as temperature increases since ozone decays faster and becomes more volatile at higher temperature. However, the temperature dependence of the *C. parvum* oocyst inactivation rate constant is more pronounced than that of the ozone decay and thus a higher overall inactivation is obtained at higher temperature despite the lower ozone concentration and corresponding exposure. For example, approximately 1.83 logs (98.5%) inactivation of *C. parvum* oocysts could be expected in this ozone contactor at 20 °C, which is significantly higher that 1.07 logs (91.5%) previously estimate for 7°C. Likewise, the temperature dependence of bromate formation is also relatively more pronounced than that of ozone decomposition, and the model prediction revealed that bromate formation would increase with increasing

temperature despite the decrease in ozone exposure. For the LWPOF ozone contactor, bromate concentration of approximately 7.7 μg/L was predicted at 20°C, a value nearly twice that of 4.0 μg/L predicted at 7°C. This finding suggested that meeting inactivation requirements for *C. parvum* oocysts would be more challenging at relatively lower temperatures, while control of bromate could be more challenging at relatively higher temperatures for this reactor. However, it is important to recognize that the trends observed for the effects of temperature on *C. parvum* oocyst inactivation and bromate formation in LWPOF are not generally applicable to other microorganisms or different water matrixes.

Another important observation is that the conversion of inactivation efficiency of *C. parvum* oocysts is 98.5% at 20°C, while the conversion of bromide to bromate is only 19.4% at the same temperature. Since back-mixing has a more pronounced effect on reactions with relatively high conversion than on reactions with low conversions (Kim *et al*., 2004; Tang *et al*., 2005), it might be possible to increase the inactivation efficiency while not greatly affecting bromate formation if the hydrodynamics of the reactor could be properly modified. Model simulation results for 20°C obtained using a much lower dispersion number (*i.e.*, $d = 0.01$) that would result in conditions much closer to an ideal plug flow reactor are shown in Figure 4.7 (green lines). In the modified hydrodynamic condition, the bromate formation level would be approximately the same, while additional 0.59 log inactivation of *C. parvum* oocysts would be achieved. It is interesting to note that, compared to the simulation results in Figure 4.6, ozone and bromate concentrations and *C. parvum* oocyst inactivation level in the contacting chamber (*i.e.*, 1st chamber) were lower than those predicted assuming CSTR condition. Additional model results thus obtained by assuming CSTR conditions for contacting chamber (d = 10,000) and low dispersion conditions for reactive chambers ($d = 0.01$) are also shown in Figure 4.7 (red lines). Even though the CSTR conditions in the contacting chamber

would result in higher ozone concentrations within this chamber, the effluent ozone concentrations from these chambers would be lower than those estimated with low dispersion conditions. Therefore, ozone concentrations and *C. parvum* oocyst inactivation in the subsequent chambers (*i.e.*, 2nd to 12th chambers) would be lower. This suggested that additional 0.41 log inactivation could be achieved by designing the contacting chamber closer to a plug flow reactor (PFR) than CSTR. If the same inactivation level in the original design (*i.e.*, 1.83 logs as shown in Figure 4.6) is targeted with lower dispersion condition (blue lines), it is possible to lower the inlet gas phase ozone concentration from 174 mg/L to 140 mg/L at the same gas flow rate. This 19.5% reduction in total ozone dosage would also result in approximately 1.44 μg/L reduction in effluent bromate concentration. This finding suggested that current ozone contactor design could be much improved by preventing extended back-mixing in each chamber.

Similar model applications were performed for 7^{o}C as shown in Figure 4.8. In general, the same trends were observed as 20^{o}C for the modified hydrodynamic conditions. When low dispersion condition (d = 0.01) was assumed for all chambers, the *C. parvum* inactivation level was increased by 0.16 log while bromate formation remains the same (green lines), compared to model simulation results in Figure 4.6 (*i.e.*, d = 10,000). Note that this gain in inactivation level was much smaller than the additional 0.59 log obtained at 20^{o}C for the same change in hydrodynamic conditions. Almost identical results were obtained by assuming contacting chamber to be close to CSTR (*i.e.*, d = 10,000) and the reactive chambers to be close to PFR (*i.e.*, d = 0.01) (red lines). When the same level of inactivation was targeted as the original design (*i.e.*, 1.07 log in Figure 4.6) by reducing the gas phase concentration from 174 mg/L to 156 mg/L at the same flow rate (i.e., 15.1 scfm), bromate formation was reduced by 0.45 μg/L. Once again, this level of reduction was much smaller than that predicted at 20^{o}C. This analysis suggests that changes in hydrodynamic conditions have greater effects at higher

temperatures since overall conversions achieved are higher (*i.e.*, higher level of inactivation and higher level of bromate formation).

The additional simulation results shown in Figure 4.9 further highlight the fact that hydrodynamics have greater impact when ozonation processes is operated with higher target inactivation. These simulations were performed to achieve 1 log (90%) and 3 log (99.9%) inactivation of *C. parvum* oocysts under two extreme hydrodynamic conditions (d = 0.01 versus d = 10,000) at 20^{o}C with varying inlet gas phase ozone concentrations and the same flow rate (i.e., 15.1 scfm). The gas phase ozone concentrations required were 85 mg/L (d = 0.01) and 98 mg/L (d = 10,000) for 1 log inactivation and 206 mg/L (d = 0.01) and 283 mg/L (d = 10,000) for 3 log inactivation, respectively. The reduction in required ozone concentration by modifying hydrodynamic conditions from close to CSTR toward close to PFR was much larger when the process was targeted for 3 log inactivation. This large reduction in ozone dosage was reflected by greater reduction in bromate formation.

One of the operating options that LWPOF as well as other ozone contactors in similar design might consider is the number and position of contacting chambers. The previous modeling predictions shown in Figures 4.6 to 4.9 were performed with the operating options of introducing entire ozone gas into 1st chamber at the flow rates of 15.1 scfm. Figure 4.10 compares this original design (blue lines) with an operating option available at LWPOF where ozone gas is introduced separately into both 1st (11.0 scfm) and 5th (4.1 scfm) chambers (red lines). The differences in final ozone concentration, *C. parvum* oocyst inactivation level and bromate concentration were minor. This simulation suggests that ozonation of water in the midway to the ozone contactor might not be beneficial for overall system performance as long as the mass transfer of gas phase ozone to water is not a limiting factor.

4.5. Conclusions

The *OCM* software developed in this study provides a useful tool for the simultaneous prediction of pathogenic microorganism inactivation and bromate formation in full-scale ozone contactors. As shown by the full-scale demonstration part of this study, the *OCM* software is also useful for evaluating and optimizing existing ozone contactors. Design of a new ozone contactor could be another possible application of the *OCM* software. Figure 4.2 summarizes the required tasks to perform model simulations using the *OCM* software.

Table 4.1. Mass balance equations for dissolved ozone, fast ozone demand, gas phase ozone, viable microorganism, and bromate, which are solved in the *OCM* software.

Dissolved ozone

$$E_L \cdot \frac{d^2[O_3]_l}{dx^2} \mp U_L \frac{d[O_3]_l}{dx} + k_L a \cdot \left(\frac{[O_3]_g}{m} - [O_3]_l \right) - k_d \cdot [O_3]_l - k_R \cdot [O_3]_l \cdot [D] = 0 \qquad (4.1)$$

Fast ozone demand

$$E_L \cdot \frac{d^2[D]}{dx^2} \mp U_L \frac{d[D]}{dx} - k_R \cdot [O_3]_l \cdot [D] = 0 \qquad (4.2)$$

Gas phase ozone

$$U_G \frac{d[O_3]_g}{dx} - k_L a \cdot \left(\frac{[O_3]_g}{m} - [O_3]_l \right) = 0 \qquad (4.3)$$

C. parvum oocyst

$$E_L \cdot \frac{d^2 N}{dx^2} \mp U_L \frac{dN}{dx} - k_N \cdot N \cdot [O_3]_l = 0 \qquad (4.4)$$

Bromate

$$E_L \cdot \frac{d^2[BrO_3^-]}{dx^2} \mp U_L \frac{d[BrO_3^-]}{dx} + k_{BrO3^-} \cdot [O_3]_l = 0 \qquad (4.5)$$

$[O_3]_l$ = dissolved ozone concentration [ML^{-3}]; [D] = fast ozone demand concentration [ML^{-3}]; $[O_3]_g$ = gas phase ozone concentrations [ML^{-3}]; N = number density of viable microorganisms [L^{-3}]; [BrO_3^-] = bromate concentration [ML^{-3}]; E_L = liquid phase dispersion coefficient [L^2T^{-1}]; x = distance from the top of each chamber in the axial direction regardless of liquid flow direction [L]; k_La = volumetric mass transfer coefficient [T^{-1}]; m = Henry's law constant [dimensionless]; k_D = first-order ozone decay rate constant [T^{-1}]; k_R = second order rate constant for ozone reaction with fast ozone demand [$L^3M^{-1}T^{-1}$]; k_N = second-order inactivation rate constant [$L^3M^{-1}T^{-1}$]; k_{BrO3-} = first-order bromate formation rate constant [T^{-1}]; U_L, U_G = liquid and gas phase approach velocities [LT^{-1}]

Table 4.2. Bounday conditions for the governing equations presented in Table 4.1.

	Counter-current mode		Co-current mode	
Dissolved species	$C\big\vert_{z=0} = C_0 + d \cdot \left.\frac{dC}{dz}\right\vert_{z=0}$	(4.6)	$\left.\frac{dC}{dz}\right\vert_{z=0} = 0$	(4.9)
	$\left.\frac{dC}{dz}\right\vert_{z=1} = 0$	(4.7)	$C\big\vert_{z=1} = C_0 - d \cdot \left.\frac{dC}{dz}\right\vert_{z=1}$	(4.10)
Gas phase ozone	$[O_3]_g\big\vert_{z=1} = [O_3]_{g,0}$	(4.8)	$[O_3]_g\big\vert_{z=1} = [O_3]_{g,0}$	(4.11)

$C = [O_3]_l$, [D], N, or $[BrO_3^-]$, $z=x/L$ = distance from top of contactor [dimensionless]; L = depth of the water column [L]; and $d = E_L/(L \cdot U_L)$ = dispersion number or inverse of Péclet number [dimensionless]

Table 4.3. Experimental matrix for tracer tests.

Test #	Contactor	Water Flow Rate (MGD)	Gas Flow Rate (scfm)	Fluoride Recovery (%)
1	#1	15.5	12.5	96
2	#1	22.5	20.6	N/A
3	#1	42.9	61.6	100
4	#2	15.5	14.7	97
5	#2	22.8	21.1	101
6	#2	42.9	65.0	99
7	#3	32.1	33.7	92
8	#4	32.1	37.9	106

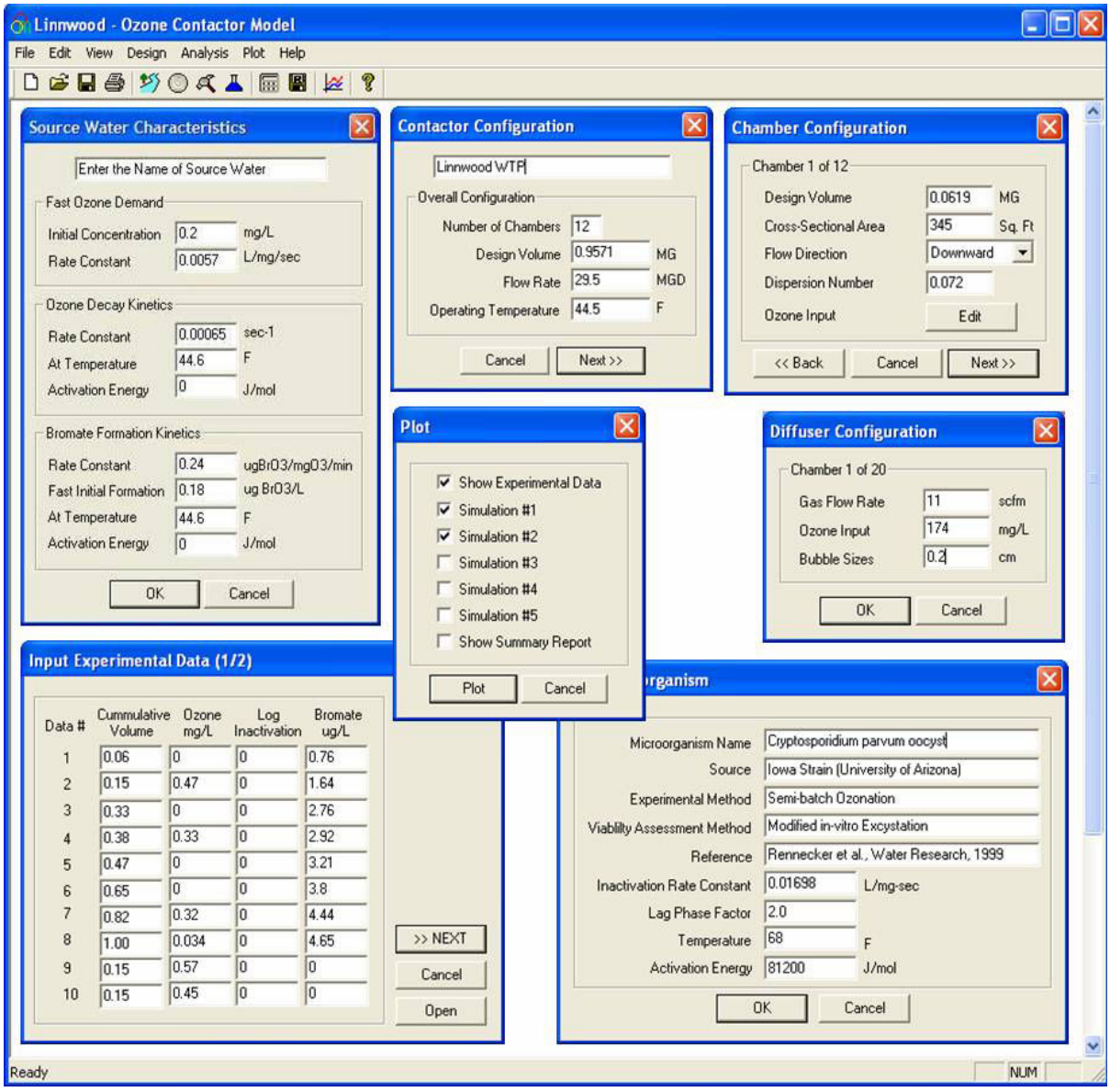

Figure 4.1. Main window of the *OCM* software with various input dialog boxes.

STEP 1. Perform bench-scale batch experiments at target temperature to determine the parameters related to ozone decay and bromate formation kinetics in the target source water. Refer to Kim *et al*. (2005) for details about the experimental setup and corresponding operation procedures, and refer to main text for analytical procedures and Figure 4 for presentation of experimental results.

Fast Ozone Demand ($[D]_0$ in mg/L): Portion of water constituents that consumes dissolved ozone at a relatively fast rate during initial phase of ozonation.
Second-Order Rate Constant (k_R in L/(mg-s)): Rate constant between fast ozone demand and dissolved ozone
First-Order Rate Constant (k_D in s^{-1}): Rate constant for first-order ozone decay after the fast ozone demand is consumed
Bromate Formation Rate Constant (k_{BrO3-} in μg BrO_3^-/(mg O_3-min)): Rate constant for bromate formation when bromate concentration is plotted versus *CT* (mg-min/L)
Initial Formation ($[BrO_3^-]_0$ in μg/L): y-intercept of linear regression line obtained when bromate concentration is plotted versus *CT*. This represents the relatively fast formation of bromate during early stage of ozonation that is consider in the model as initial amount present in the source water
Activation Energy (E_a in J/mol): A parameter that characterizes temperature dependence of ozone decay and bromate formation kinetics. Needed when modeling at varying temperature. Batch experiments should be performed at a minimum of two (optimum of three) different temperatures to determine E_a.

STEP 2. Specify ozone contactor configuration and operating conditions. Parameters such as number of chambers, design volume, flow rate, operating temperature, design volume for each chamber, chamber cross section, flow direction, ozone gas flow rate, inlet gas phase ozone concentration are readily available for existing contactors. These parameters can be changed for simulations under different design and operation options. The following two parameters should be determined experimentally.

Dispersion Number (*d*, dimensionless): A parameter that determines mixing condition in each chamber. To obtain *d* for existing contactor, perform tracer tests under flow conditions identical to those used in actual operations using a conservative tracer chemical (e.g., fluoride). It is desirable to perform individual tracer test for each chamber and analyze each tracer curve following the procedure by Mariñas *et al*. (1993). However, if tracer tests are to be performed for the entire contactor, additional analysis is needed to estimate *d* for each chamber (refer to Tang et al., 2005).
Bubble Size (d_B in cm): If possible, measure the size distribution of a large number of bubbles photographically and determine the average value. If not possible, consult with the manufacturer of the diffuser to obtain estimate value.

STEP 3. Specify the characteristics of target microorganisms. Use the existing database or perform a literature search for the kinetics of target microorganisms and manually input the kinetic information.

Inactivation Rate Constant (k_N): Rate of pathogen inactivation under exposure to dissolved ozone. The rate constant is based on pseudo-first order Chick-Watson inactivation kinetic law.
Lag Phase Factor (N_1/N_0): The extent of lag phase during which little or no inactivation is observed. The value is based on the delayed Chick-Watson kinetic law described by Rennecker *et al*. (1999).
Activation Energy (E_a in J/mol): A parameter that characterizes temperature dependence of pathogen inactivation. Needed when modeling at varying temperature.

STEP 4. Perform simulation. Input full-scale experimental results if available and compare with the model predictions. Perform simulations under different design and operation options and compare simulation results.

Figure 4.2. Glossary for the required parameters and procedures to perform model simulations using the *OCM* software.

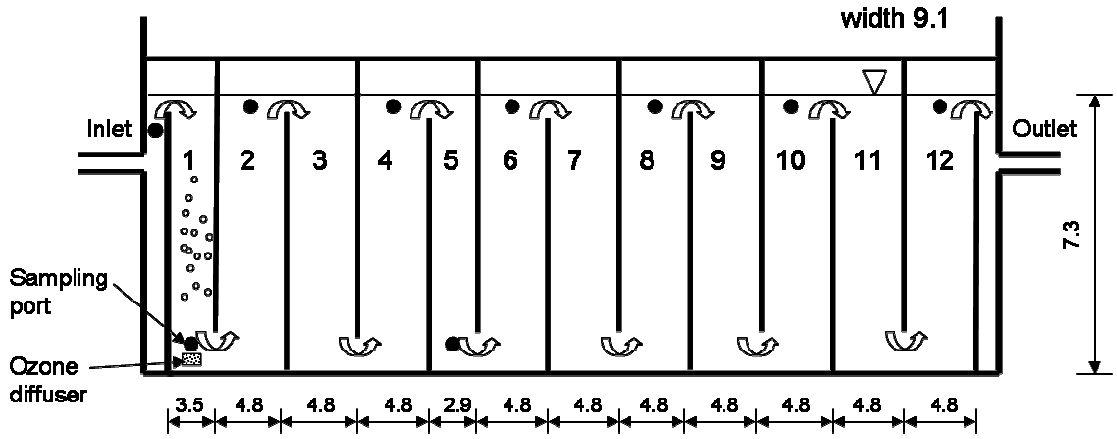

Figure 4.3. Schematic diagram of one of four parallel ozone contactors at the Linnwood Water Plant Ozone Facility (LWPOF) at Milwaukee Water Works, Milwaukee, WI (units in meter).

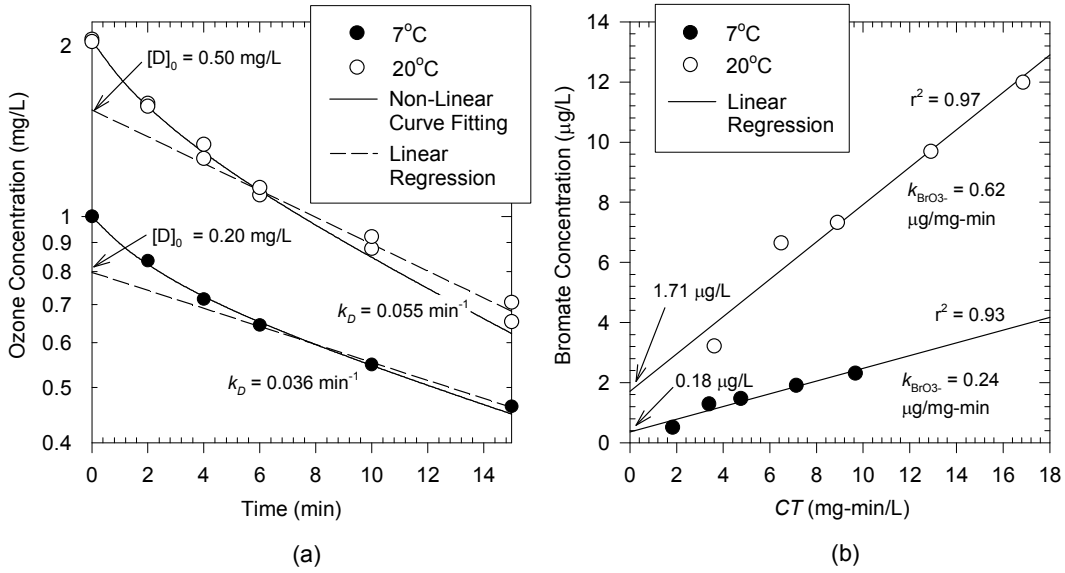

Figure 4.4. Batch experimental results and analysis for (a) ozone decay and (b) bromate formation in the target source water at 7°C and 20°C.

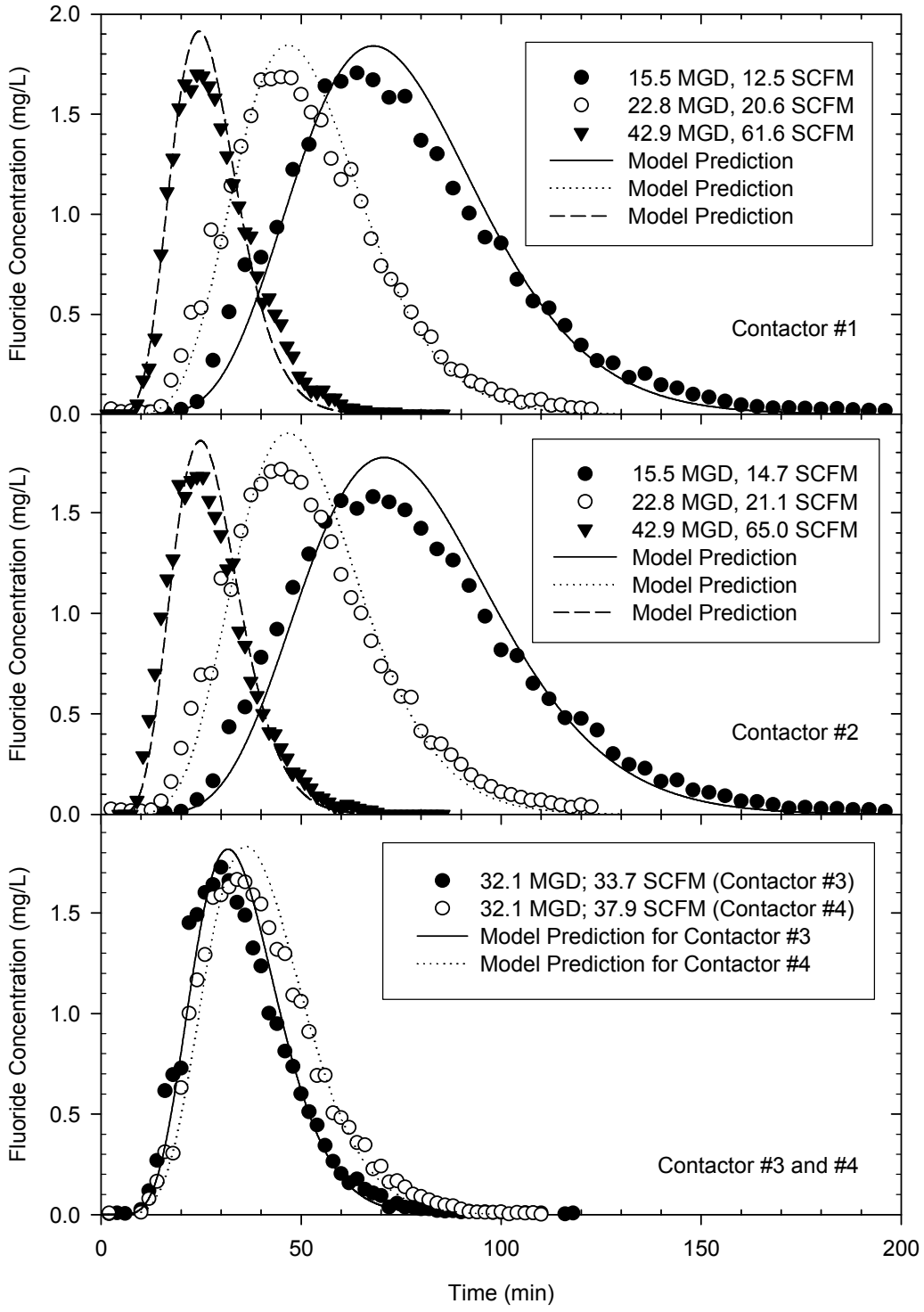

Figure 4.5. Tracer test curves determined experimentally and predicted with the ADR model (d = 10,000).

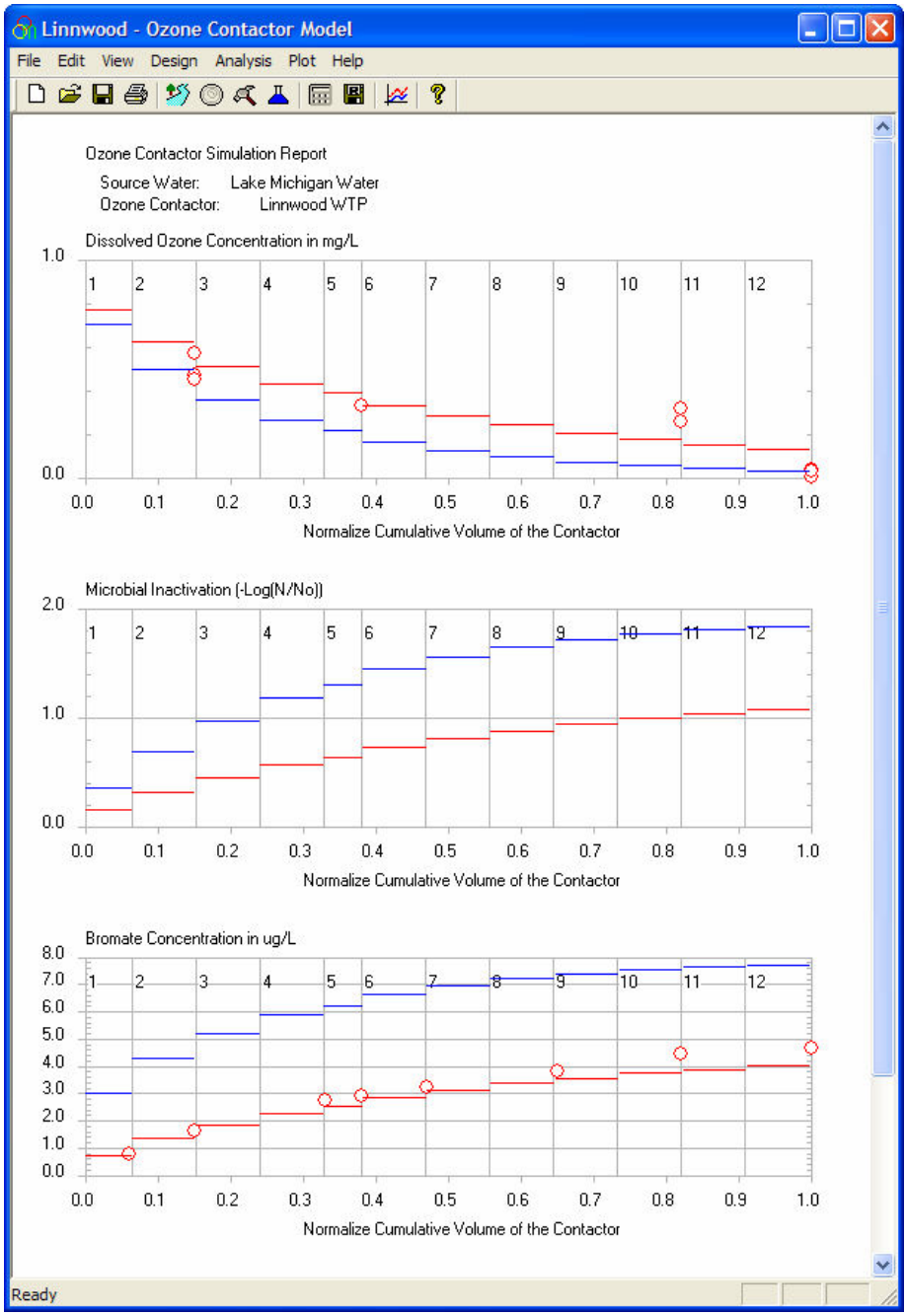

Figure 4.6. Full-scale simulation of LWPOF ozone contactor performance at two different temperatures (red lines for 7°C and blue lines for 20°C) and comparison to field experimental results at 7°C.

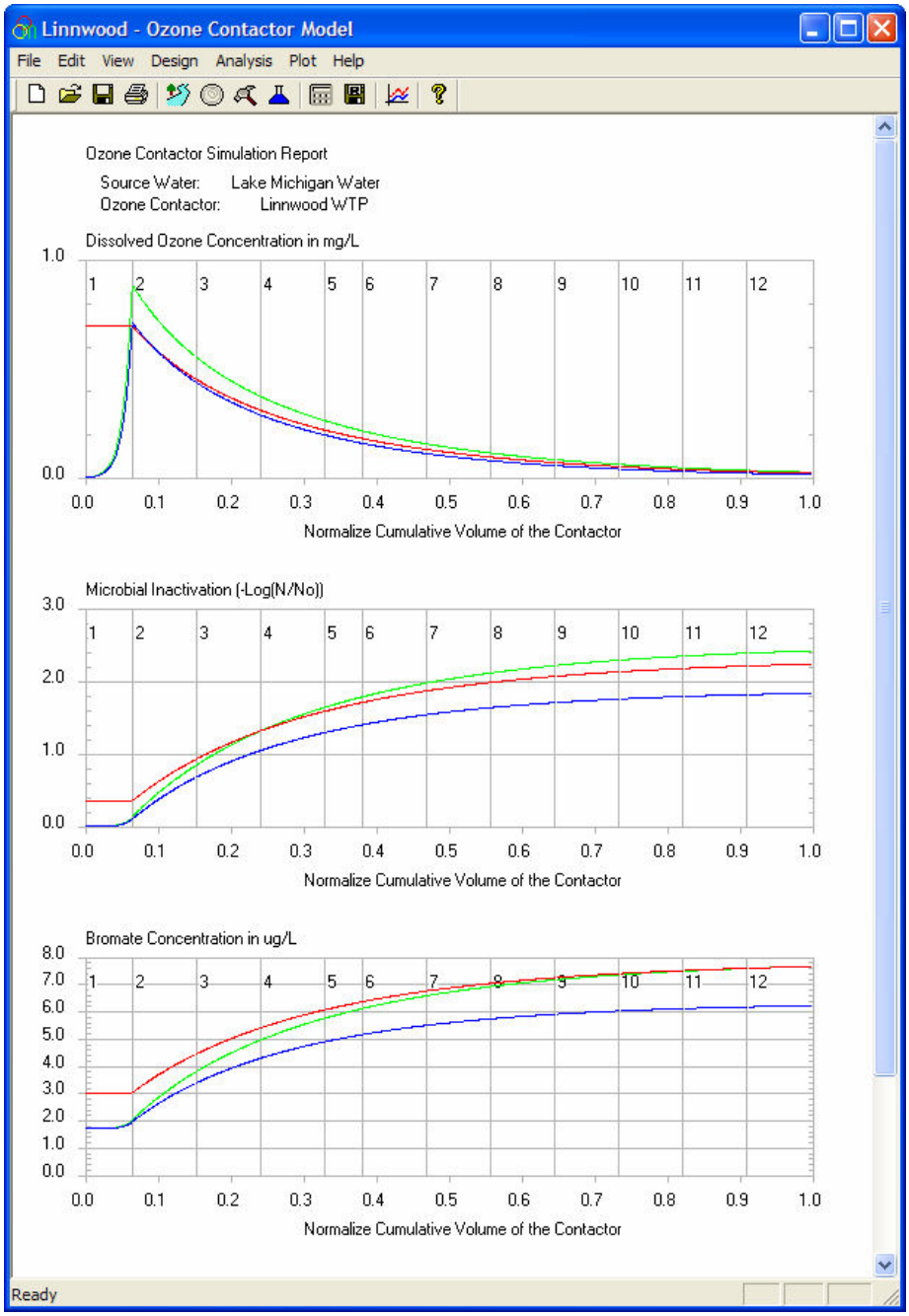

Figure 4.7. Full-scale simulation at modified hydrodynamic conditions at 20°C. Green lines represent model simulation results obtained by assuming $d = 0.01$ for all chambers; red lines by assuming CSTR (d = 10,000) for contacting chamber and $d = 0.01$ for reactive chambers; and blue lines by using $d = 0.01$ for all chambers and reduced ozone input (to achieve the same target inactivation shown in Figure 4.6).

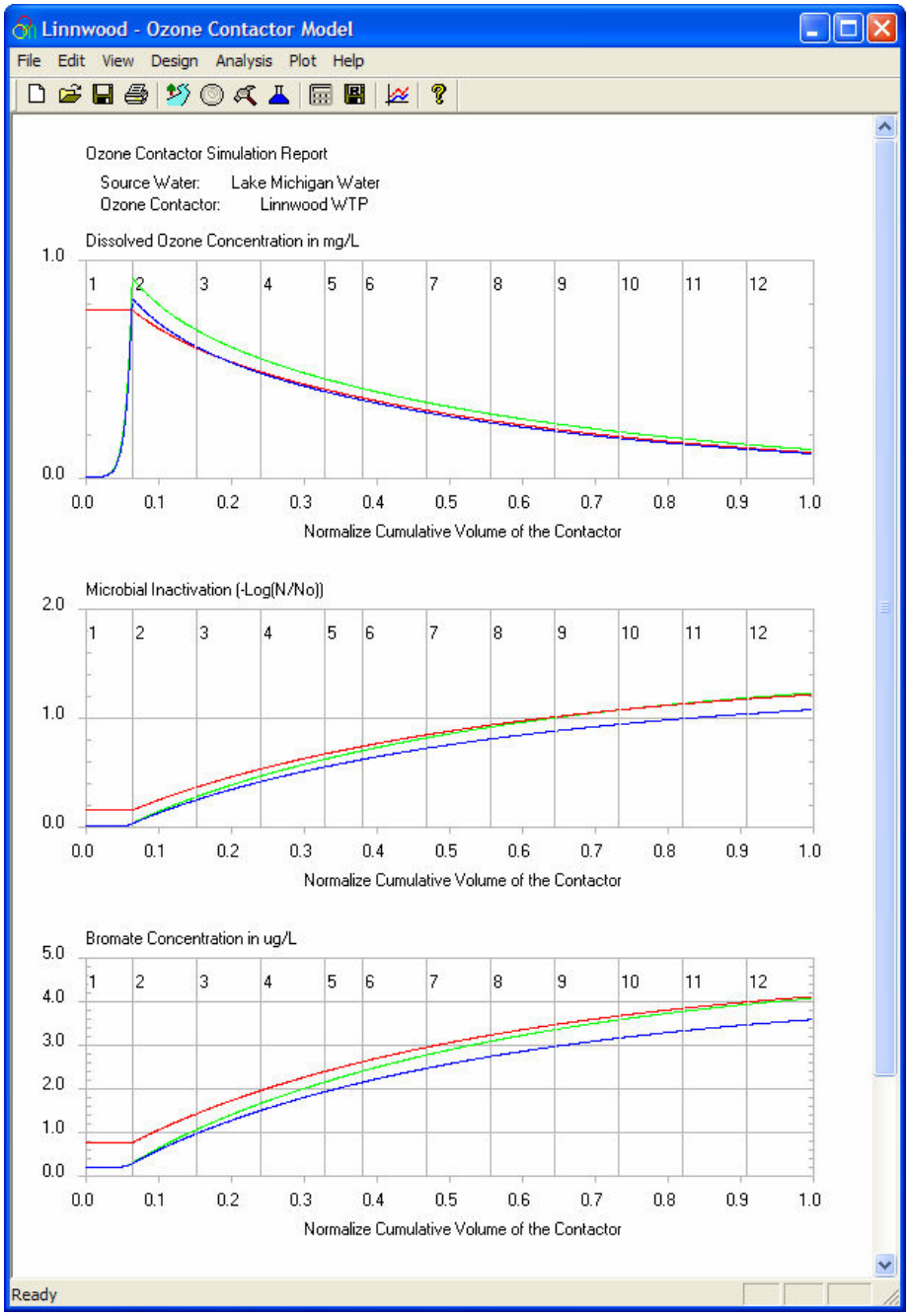

Figure 4.8. Full-scale simulation at modified hydrodynamic conditions at 7°C. Green lines represent model simulation results obtained by assuming $d = 0.01$ for all the chambers; red lines by assuming CSTR ($d = 10{,}000$) for contacting chamber and $d = 0.01$ for reactive chambers; and blue lines by using $d = 0.01$ for all the chambers and reduced ozone input (to achieve the same target inactivation shown in Figure 4.6).

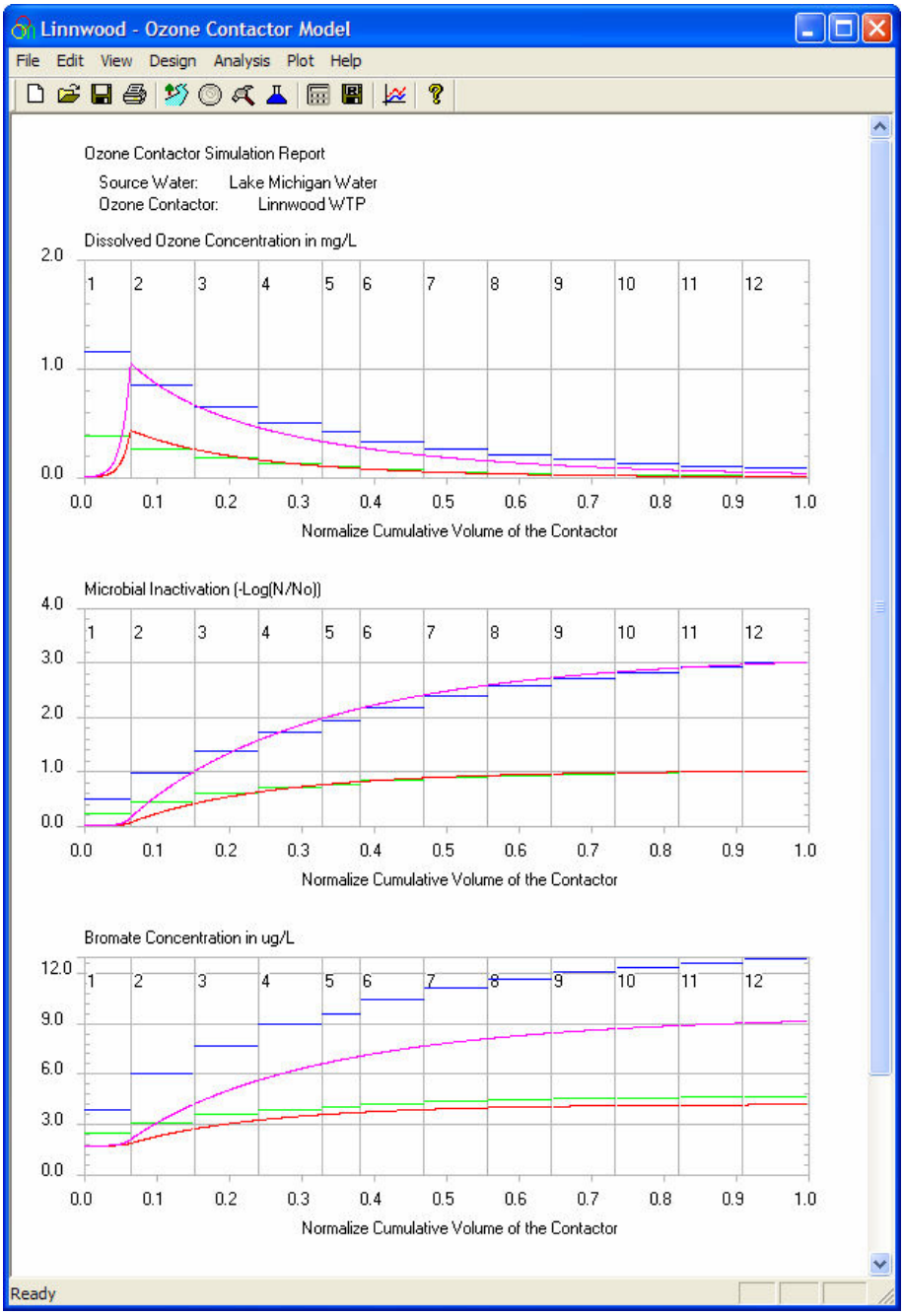

Figure 4.9. Model simulations at different target *C. parvum* oocyst inactivation with different hydrodynamic conditions at 20°C. Purple lines: target inactivation level = 3 logs and d = 0.01; blue lines: target inactivation level = 3 logs and d = 10,000; red lines: target inactivation level = 1 log and d = 0.01; green lines: target inactivation level = 1 log and d = 10,000.

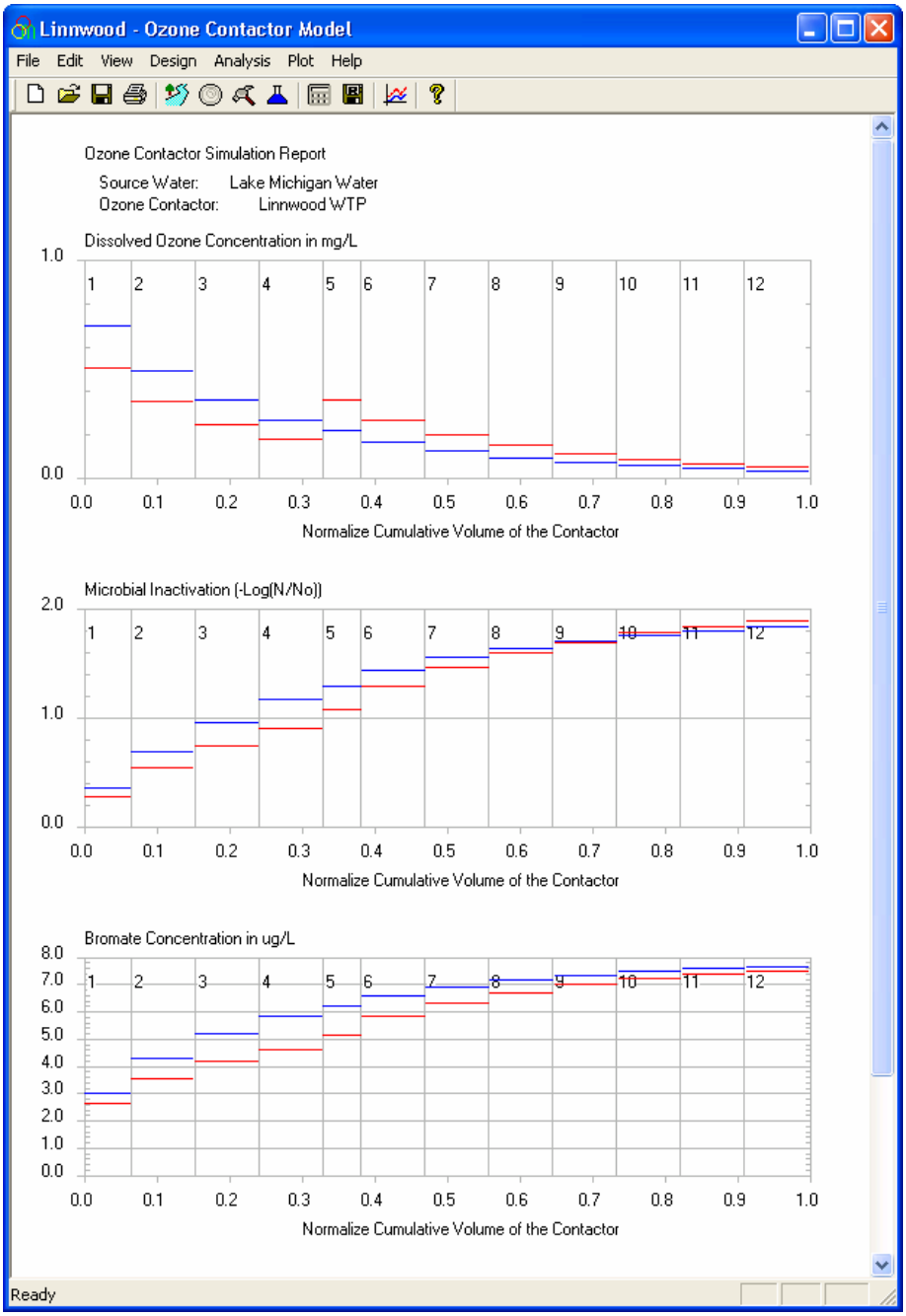

Figure 4.10. Simulation results comparing modes of ozone gas injection. Red lines: gas phase ozone was introduced into 1st and 5th chambers at flow rates of 11.0 and 4.1 scfm. Blue lines: all ozone was injected into 1st chamber at flow rate of 15.1 scfm

CHAPTER 5

OZONE CONTACTOR FLOW VISUALIZATION AND DESIGN IMPROVEMENTS FOR DISINFECTION ENHANCEMENT USING THREE-DIMENSIONAL LASER-INDUCED FLUORESCENCE (3D-LIF)

5.1. Introduction

Ozone disinfection has been considered to be one of the most promising alternatives to chlorine based dinsfection since it has much higher *Cryptosporidium parvum* oocyst inactivation efficiency and produces much less halogenated DBPs (Gyürék, et al, 1999;Rennecker, et al, 1999;Rennecker, et al, 2000). The number of water treatment facilities using ozone as a primary disinfectant is growing in places where surface water is used as a source. Ozone disinfection in drinking water treatment facilities is carried out in an ozone contactor with multi- vertical or horizontal chambers where ozone is fed by fine bubble diffusers (FBD) or side-stream venturi injectors (SVI). The SVI system is preferred when ozone is generated from pure oxygen, since volumetric flow rate is typically not sufficient for the bubble diffuser (Schulz, et al, 1995). In addition, influent momentum in the SVI system, which provides turbulent mixing in the ozone contactor, provides more enhanced mass transfer. The SVI system uses kinetic energy of influent discharged from inlet pipe for mixing in the ozone contactor and provides efficient hydrodynamics as long as it is properly designed (Schulz & Bellamy, 2000).

The hydrodynamics of an ozone contactor strongly affect the overall conversion of all the chemical and inactivation reactions (Roustan, et al, 1993;Henry & Freeman, 1995;Do-Quang, et al, 2000a;Do-Quang, et al, 2000b). The integrated disinfection design

framework (IDDF) categorized the hydraulic characteristics of a disinfection tank as major components (Bellamy, et al, 2000) of a water disinfection system. Its effect is more pronounced for reactions with relatively higher conversion (e.g., inactivation of *C. parvum* oocysts up to 99 to 99.9 percent) compared with reactions with lower conversion (e.g., bromate formation from bromide is typically below 30 percent). Consequently, the reactor hydrodynamics could be optimized to minimize bromate formation while achieving target inactivation efficiency for *C. parvum* oocysts (Tang, et al, 2005; Kim, et al, 2006).

Ozone disinfection in a drinking water treatment facility is currently regulated by a guideline based on CT_{10} values proposed by the Surface Water Treatment Rule (USEPA, 1991), where C is the ozone concentration and T_{10} is defined as the time needed for 10% of the total accumulated tracer to pass through the ozone contactor. Disinfection could be enhanced by increments of T_{10} with the same amount of disinfectant. T_{10} is obtained from a one-dimensional residence time distribution (RTD) curve using a conservative tracer test and affected by the hydrodynamic condition within the reactor. Hydrodynamic condition can be quantitatively represented by various ways. One of the more common approaches employs a dispersion number as a single one-dimensional parameter (Bellamy, et al, 2000). Dispersion number (d) is defined as:

$$d = \frac{D}{UL} \tag{5.1}$$

where D, U, and L represent diffusivity (L^2T^{-1}), axial velocity(LT^{-1}), and characteristic length (L), respectively. The dispersion number, which is the inverse of the Péclet Number, is calculated using the following expression:

$$2d - 2d^2\left(1 - \exp\left(-\frac{1}{d}\right)\right) = \frac{\sigma^2}{\tau^2} \qquad (5.2)$$

where σ^2 and τ are the variance and the mean residence time, respectively. Back-flow, short-circuiting, and the stagnant zone in the ozone contactor also play very important roles in T_{10} (El-Din & Smith, 2001;Greene, et al, 2004). However, one-dimensional tracer analysis is limited at explaining three-dimensional complex flow motion induced by the geometry of a contactor and influent momentum energy.

As a result, more sophisticated tools such as computational fluid dynamics (CFD) have been used to analyze three-dimensional mixing conditions in ozone contactors (Henry & Freeman, 1995;Murrer, et al, 1995;Huang, et al, 2002). CFD simulations have suggested that a hydrodynamic condition closer to an ideal plug flow might be achieved by optimizing the width of the channel and the height and the width of the baffling opening (Henry & Freeman, 1995). However, such CFD predictions have not been empirically verified either in the laboratory or on a large scale. The impact of hydrodynamic conditions determined by such design variables on inactivation efficiency, which is a primary concern in ozone contactor design, also needs to be quantitatively investigated. The traditional method of determining the impact of such conditions has been the direct measurement of flow and its concentration with a probe or by sampling. However, this method may cause flow disturbance and allows only a limited number of samples in two or three dimensions. A more non-intrusive technique that does not interfere with flow is therefore required. The three-dimensional laser-induced fluorescence (3D-LIF) for flow visualization is a useful tool with which mixing in various types of reactor systems can by empirically observed by quantifying the entire instantaneous tracer concentration field at very high resolution in three-dimensional space (Tian & Roberts, 2003).

3D-LIF technology for analyzing the hydrodynamics of an ozone contactor is carried out using a physical model ozone contactor, which is a miniature of the proto-scale ozone contactor under construction in South Korea. The primary purpose of this ozone contactor is to mitigate the taste and odor problem, but it can also serve as a secondary disinfection barrier. The full-scale ozone disinfection system is composed of two parallel ozone contactors, each of which has two chambers in the series and treats 95,000 m^3 per day (25 MGD). Ozone is directly fed into influent pipe using a side-stream venturi injection (SVI) system. Influent from an 1.35 m diameter pipe directly discharges the mixture of ozone and raw water into the first ozone chamber. Flow is horizontal in the first and second contactors, which are divided by a baffle, shown in Figure 5.1. Treated water flows out of the ozone contactor through an overflow weir, installed at the end of the second chamber, and into a sump tank.

A physical model of the ozone contactor is generally scaled down with similitude with a dimensionless Froude or Reynolds number. However, since it is impossible to maintain complete similitude, the scale-down is done using partial similitude with a dominant parameter. A Froude number is preferred to a Reynolds number in an open channel (Ettema, et al, 2000). The Reynolds number of a physical contactor model is much smaller than that of a full-scale contactor model because of reduced length and velocity. This, however, is not a serious constraint if flow is fully turbulent (i.e., the Jet Reynolds number is larger than 2,000) (Ferrier, et al, 1993). It is plausible to use a Froude number similitude since mixing in the first ozone contactor is caused by an inflow jet-like injection (the physical model has a Jet Reynolds number of 6,290 at 14L/min and a 45mm influent diameter) in the open channel. Scale-down using Froude number similitude was already used for the design of an ozone contactor (Heathcote & Drage, 1995) and a water storage reservoir (Grayman, et al, 1996).

The objective of this study is to analyze the hydrodynamics of new ozone contactor and achieve optimization using the 3D-LIF technology for a new ozone contactor design. The hydrodynamics include the effects of the discharge jet diameter, the influent velocity, and the diffusion wall installed in the first ozone chamber to stabilize flow turbulence and evenly distribute the raw water and ozone mixture. As a result, more enhanced design options will be available.

5.2. Material and Methods

5.2.1. 3D-LIF System

The principles of the 3D-LIF system are explained in detail by Tian and Roberts (2003). Briefly, scanning planar laser sheets are created by sequentially reflecting an Argon-ion laser beam (1.75 W in power) using two orthogonal axis oscillating scanning mirrors and a plano-convex lens with a 250 mm diameter and a 940mm focal length, as shown in Figure 5.2. Forty laser slices complete a set of spatial scans within 0.4 seconds. A laser dye, Rhodamine 6G, in the path of the laser slice, excited by a 514 nm laser beam, emits fluorescent light. The planar sheet of fluorescent light, which is proportional to the tracer concentration, is captured using a high-speed CCD camera (Dalsa® CA-D6, Ontario, Canada) at the rate of 100 frames per second with 256 gray levels and then stored in a high-capacity storage device. The CCD camera is equipped with a sensor with a resolution of 532 by 526 pixels, a lens with a focal length of 25mm (Fujinon, Saitama, Japan), and a filter of 530 nm filter (Schott glass 530, Reynard Corporation, San Clemente, CA) between the lens and the CCD sensor. The captured images are further processed to correct both their darker margin (i.e., vignetting) caused by the optical error of the lens and the loss of laser intensity during travel through water (i.e., attenuation), pixel by pixel, according to Tian and Roberts (2003). These processes are done by *TFlook* software developed by Tian and Roberts (2003).

5.2.2 Physical Scale Ozone Contactor

A proto-ozone contactor is scaled down to a physical scale reactor with Froude number similarity. Each physical parameter is related by the Buckingham π-theorem (Munson, et al, 1998), as in Equation (5.3).

$$\frac{t \times U}{H} = \varphi\left(\frac{U}{\sqrt{gH}}, \frac{W}{H}, \frac{D}{H}\right) \tag{5.3}$$

where *t, U, H, g, W, D,* and *L* represent residence time (T), velocity (LT^{-1}), height (L), gravitational acceleration (LT^{-2}), width (L), and length (L), respectively. The physical model and the proto-ozone contactor share each term in equation (5.3) for Froude number similitude. Physical model scales are obtained by multiplying the following scale factors by those of the proto-scale: length scale = 1/30, velocity scale = $(1/30)^{1/2}$, time scale = $(30)^{1/2}$.

5.2.3 Conservative Tracer Test with a 3D-LIF System

Conservative tracer tests using 3D-LIF were carried out with the physical model ozone contactor. Tap water was fed after de-chlorination at room temperature (20±2°C). 2mL of a laser-dye stock solution (i.e., 100 mg/L of Rhodamine 6G, Sigma-Aldrich, St. Louis, MO) was pulse-injected directly into influent pipe of a model ozone contactor using a syringe. Image capture was initiated instantaneously after the dye pulse injection for about 180 seconds. Captured images were processed with the methods described at section 5.2.1. The residence time distribution curves could be obtained from any point and slices in three dimensions. Generally, RTD curve data were extracted from three dimensional data set using Tecplot® statistical tool kit (*Tecplot* Inc., Bellevue, WA).

The image was calibrated using the acrylic calibration column (33 mm D × 70 mm W × 45 mm H) filled with the 50 μg/L Rhodamine 6G solution.

5.3. Results and Discussion

5.3.1. Flow Analysis Using 3D-LIF Visualization

Conservative dye transport through a new ozone contactor was experimentally visualized using 3D-LIF. Representative mixing and dye transport behavior over time are shown in Figure 5.3 for the first chamber and Figure 5.4 for the second chamber with the design flow rate, 95000 m^3/day, and an influent jet diameter of 1.35 m. These figures, illustrated in three dimensions, show a 12.5 μg/L iso-surface, which is depicted in gray shading. Figure 5.3 (30 sec.) shows that the influent turbulent jet is redirected by the opposite wall and thus split into and upward and downward flows. The split flows are developed into two upper and lower longitudinal spirals swirling in the ozone contactor in Figure 5.3 (60 sec). As a result, two plums exist in the upper and lower regions of the first ozone chamber from Figure 5.3 (90 sec). As the plums move into the second chamber, distinctive two plums are almost diminished as shown at the Figure 5.4.

The jet discharge of the influent into the first ozone chamber was originally expected to cause irregular, intense turbulent mixing near the inlet and thus presents hydrodynamic characteristics similar to those of the continuous stirred tank reactor (CSTR). However, the normalized residence time distribution (RTD) curve at the end of the first and second chambers in the ozone contactor fit well with that of the axial dispersion reactor (ADR) model, as shown in Figure 5.5. The dispersion number (*d*) is 0.168 in the first chamber, which is less than the dispersion number, 0.2, considered as an approximate plug flow (Khudenko & Shpirt, 1986;Makinia & Wells, 2005). The reasons for the unexpected approximate plug flow in the first chamber could be explained by flow visualization using 3D-LIF. Figure 5.6 shows the contour slices obtained at 90 seconds

after the pulse injection in the middle of the longitudinal direction of the first ozone contactor. From this figure, two spirals that rotate counter-clockwise at the upper region and clockwise at the lower region are shown. These spirals, caused by influent kinetic energy, are thought to render lateral mixing and play an important role in preventing short-circuiting and back-flow, and the creation of a stagnant zone.

5.3.2. Effects of Jet Diameter and Flow Rate on Dispersion and Mixing

Influent momentum (i.e., flow rate times jet diameter) is shown to have significant impacts on mixing behavior of a tank because this provides initial kinetic energy for mixing (Rossman & Grayman, 1999;Martinson & Lucey, 2004) but little is known for its effects on dispersion number (*d*) when it is directly discharged into reactors like an ozone contactor. It is hard to decide optimal influent momentum to minimize dispersion number and maximize lateral mixing because of the limitation in the experimental methods and fluctuating flow rate. 3D-LIF system, however, provides a very useful and efficient tool to study three dimensional hydrodynamics of an ozone contactor characterized by the turbulent influent momentum.

Three different influent diameters are compared with RTD from conservative tracer tests using the 3D-LIF. The influent jet diameters are 25, 45, and 65 mm in the physical model scale, equivalent to 0.75, 1.35, 1.95 m in the proto-scale, respectively. Flows are 10, 14, and 18 L/min in the physical model scale, equivalent to 71,000, 95,000, 130,000 m^3/day in the proto-scale, respectively.

The dispersion numbers of the first ozone chamber are compared for each flow rate and influent jet diameter as summarized at Table 5.2. For the 0.75 and 1.35 m diameter jets, the overall dispersion numbers are low and close to the approximate plug flow at three flow rates. Specifically, the dispersion numbers of 0.75 m diameter jet

range from 0.21 to 0.26 and show negligible difference according to flow rate, as shown in Figure 5.7-a). For the 1.35 m diameter jet, the dispersion numbers are 0.16 and 0.17 for 71,000 m^3/day and 95,000 m^3/day, respectively, but the increased up to 0.27 for 130,000 m^3/day, which results in more dispersion than the other flow rates as shown in Figure 5.7-b).

The 1.95 m diameter jet shows quite different results from 0.75 m and 1.35 m as shown Figure 5.7-c). It has low dispersion number at 71,000 m^3/day and 130,000 m^3/day but very high dispersion number at 95,000 m^3/day. Higher dispersion number at 95,000 m^3/day could be explained using 3D-LIF observations as shown at Figure 5.8. This flow develops minor swirling and dye flows fast in the longitudinal direction along the lower side of horizontal baffle, which causes severe short-circuiting. On the contrary, 130,000 m^3/day develops swirling flow to avoid short-circuiting flow at the lower part. 71,000 m^3/day is thought to lack enough momentum to lead to neither short-circuiting nor swirling flow. From this, spiral swirling is confirmed to play an important role to prevent short-circuiting in an ozone contactor.

T_{10}/HDT values at Table 5.2 ranges from 0.30 to 0.51, which are almost equivalent to 2 or 6 CSTR in series, respectively. Note that these T_{10}/HDT values are from only one chamber. This result also confirms that direct discharge into the first ozone chamber could bring very good hydrodynamics for ozone contactor design.

Figure 5.9 compares normalized residence time distribution curve with different discharge jet diameter at design flow rate (95,000 m^3/day) at five sampling slices (P1, P2, P3, P4, and P5 which are designated at Figure 5.1). P1 is one thirds of the first chamber, P2 is two thirds of the first chamber, P3 is the end of the first chamber, P4 is the middle of the second chamber, and P5 is the end of the second chamber. RTD curves are

obtained by averaging concentration in each slice at each time for the whole experimental time periods. 1.95 m jet does not exhibit notable difference from 0.75 m and 1.35 m jet at P1 slices but begin to show short-circuiting peak at P2 and P3 slices. 1.95 m jet results in slightly higher dispersion than 0.75 m jet at P4 and P5.

The dispersion numbers at each slice and design flow rate are summarized at Table 5.3. 1.35 m shows lowest dispersion at any slice among three influent jets. 0.75 m jet shows highest dispersion number at P1 and P2, which is thought to be related to its highest momentum flux. Effluent dispersion numbers at P5 show similar number regardless of jet diameter because of the buffering effect of the second chamber. Axial diffusivity (D) is obtained by multiplying axial velocity (U) and characteristics length (L) to the dispersion number using Equation (5.1). Diffusivity at each slices are summarized at Table 5.4. From this table, it is shown that the lowest diffusivity is obtained from 1.35 m jet. Diffusivities are relatively higher at influent slice for the 0.75 and 1.35 m jet but almost constant for 1.95 m jet. It is also interesting to note that diffusivities for 0.75 m jet are relatively higher up to P2 because of its highest momentum flux.

Analysis of influence of inflow momentum flux (M) on dispersion in the first chamber is shown at Figure 5.10. Momentum flux is defined as:

$$M = Q \times U = \frac{4}{\pi}\left(\frac{Q}{\phi}\right)^2 \tag{5.4}$$

where Q is flow (m^3/hr), U is discharge velocity (m/hr), and ϕ is discharge jet diameter (m). Discharge jet diameters, 0.75 and 1.35 m, are only used for linear regression with momentum flux without 1.95 m because it has severe short-circuiting at design flow rate. Dispersion numbers shows tendency to increase as the momentum flux increases, which

is reversal fashion of mixing time. Mixing time is inversely proportional to the square of momentum flux (Rossman & Grayman, 1999). As momentum flux is inversely proportional to the square of discharge jet diameter, 1.95 m diameter could have the lowest momentum flux among this experimental matrix. However, the dispersion numbers are relatively high at design flow rate because of possible short-circuiting. Consequently, 1.35 m seems to be optimal inflow diameter among three discharge jet diameter by dispersion number.

Lateral mixing of an ozone contactor design is critical because localized higher ozone concentration, caused by improper mixing, could result in higher ozone demand. Studies on the efficiency of mixing inside the ozone contactor were carried out through the analysis of the fluctuation of effluent ozone concentration in the end of each chamber (Schulz & Bellamy, 2000). The limitation of this method was that it does not consider concentration variations inside an ozone contactor. However, the 3D-LIF system can utilize complete spatial and dynamic data to analyze its mixing behavior. The efficacy of lateral mixing is analyzed with a coefficient of variation (COV). The COV is defined as:

$$COV = \frac{\text{Standard Deviation of Tracer Concentrations}}{\text{Mean Tracer Concentration}} = \frac{\sqrt{\frac{1}{n-1}\times\sum_{i,j,k}\left(C(x_i,y_j,z_k,t)-\frac{1}{n}\times\sum_{i,j,k}C(x_i,y_j,z_k,t)\right)^2}}{\frac{1}{n}\times\sum_{i,j,k}C(x_i,y_j,z_k,t)} \tag{5.5}$$

where n is the number of data samples at a given time, t (T) and C (ML^{-3}) are the time and the dye concentration, respectively. The COV changes of four slices (P1, P2, P3, and P4) over time with different influent jet diameter are shown at Figure 5.11. From this figure, 0.75 m shows the fastest lateral mixing and reaches to complete mixing (10% COV) among three discharge jet diameter because of the highest momentum flux. The

mixing behavior in the first ozone chamber is visually represented in Figure 5.12, which illustrates the distribution of dye concentration after 60 seconds from dye injection.

The identification of the optimal jet diameter of design flow is complex as 0.75 and 1.35 m are preferred from lateral mixing and dispersion, respectively. Thus, the optimal efficacy of lateral mixing and dispersion could not be satisfied with a single jet diameter. Based on the current T_{10} concept, although the 1.35 m influent jet is preferred for lower dispersion, it lacks the advantage of faster lateral mixing when compared with the 0.75 m jet. Therefore, to gain the advantage of faster lateral mixing, more chambers might be required to compensate for higher dispersion number.

5.3.3. Effects of Optional Diffusion Wall

To stabilize turbulence and evenly distribute flow in the ozone contactor, a diffusion wall, a multi-porous baffle, was installed in the channel (Hannoun & Boulos, 1997). From Figure 5.10, it is shown that axial dispersion number decrease as the momentum flux decrease, which is inversely proportional to square of discharge jet diameter. Therefore, as momentum flux is decreased if discharge jet diameter is increased without accompanying short-circuiting, it would results in more beneficial low dispersion. Note that diffusivity is highest at influent discharge region and decreased at the downstream region of ozone contactor. Furthermore, hydrodynamic effects by influent jet diameter and fluctuating flow could be diminished. Two types of diffusion walls are attempted at the first chamber of ozone contactor as shown at Figure 5.1. One has fifty evenly spaced pores (5×10) of 7 mm diameter and the other has eighteen (3×6) of 13 mm diameter. The diameter of the pores has been arbitrary chosen, but the opening area is the same (i.e., 22 cm^2), which is bigger than opening area of 45 mm (16 cm^2). The pore diameters of 7mm and 13mm are equivalent to those of 0.21 and 0.38 m in the proto-scale, respectively.

The effect of the diffusion wall is compared using normalized RTD curves, shown in Figure 5.13. Figure 5.13-b) shows clear short-circuiting when the diffusion wall with 0.21 m pores is installed. Figure 5.13-c) shows slightly better T_{10} with the diffusion wall of 0.38 m pores than without it (Figure 5.13-a)), but the dispersion number of the former is slightly higher. This discrepancy is caused because the normalized RTD curves do not match those of the ADR model well when the porous diffusion wall is installed because the wall disturbs the spiraling stream and causes back-mixing.

The short-circuiting formation with the 0.21 m pore diffusion wall can be clearly visualized using 3D-LIF, as shown at Figure 5.14. The 3D-LIF results show that the dye plume moves quickly at the bottom of the first ozone chamber. Some of this dye plume flows backward when it reaches the end of the first ozone chamber, forming backward circulation that entraps some of the dye in the first chamber. This non-ideal flow with the 0.21 m diameter pore diffusion wall seems to occur because relatively higher static pressure is required for it to pass through the smaller pores. However, the 0.38 m diameter pore diffusion wall creates less resistance than the 0.21 m wall and thus disperses dye more efficiently. Similar to the 0.21 m wall, the 0.38 m wall shows slight backward circulation. As a result, diffusion walls does not appear to play an important role in the improvement of ozone contactor hydrodynamics because the advantages of the dispersion number and the T_{10} value are minor and the diffusion wall disturbs spiral swirling, which plays an important role in mixing.

5.5. Conclusion

The 3D-LIF technology provides very useful flow visualization for the design of a new ozone contactor, which could not be achieved through conventional flow

visualization technology. Direct discharge into the ozone contactor results in efficient flow hydrodynamics with 0.75 m and 1.35 m influent jets, but it suffers from short circuiting with the 1.95 m influent jet at design flow. Spiral swirling formed by the influent momentum in the ozone contactor plays a significant role for proper lateral mixing and dispersion in the first ozone chamber. Lower dispersion number could be obtained by lowering momentum flux but is inevitable to lose slight lateral mixing. Installation of a diffusion wall for lower momentum flux and better lateral mixing is not recommended because it might hinder the swirling effect, raises capital cost issue, and might cause back-flow in an ozone contactor. To deal with fluctuating flow and provide more flexibility to the operator in the water treatment facility, a sluice gate, which might change the jet diameter, is recommended as a design alternative.

Table 5.1. Experimental matrix. Proto-scale flow and discharge jet diameter are shown in the parenthesis.

	25 mm (0.75 m)	45 mm (1.35 m)			65 mm (1.95 m)
		No DW*	7mm DW*	13mm DW*	
10 L/min (71,000 m^3/d or 18.8 MGD)	AS01	AS04	AS07	AS10	AS13
14 L/min (95,000 m^3/d or 25.1 MGD)	AS02	AS05	AS08	AS11	AS14
18 L/min (130,000 m^3/d or 34.3 MGD)	AS03	AS06	AS09	AS12	AS15

DW* : Diffusion Wall

Table 5.2. Dispersion numbers and T_{10}/HDT value at the first chamber. Proto-scale flow and discharge jet diameter are shown in the parenthesis.

Diameter	25 mm (0.75 m)		45 mm (1.35 m)		65 mm (1.95 m)	
Flow rate	dispersion number	T_{10}/HDT	dispersion number	T_{10}/HDT	dispersion number	T_{10}/HDT
10 L/min (71,000 m^3/d or 18.8 MGD)	0.21	0.43	0.16	0.45	0.17	0.51
14 L/min (95,000 m^3/d or 25.1 MGD)	0.21	0.38	0.17	0.45	0.36	0.30
18 L/min (130,000 m^3/d or 34.3 MGD)	0.26	0.38	0.27	0.37	0.20	0.43

Table 5.3. Axial dispersion numbers at each slice as shown at Figure 5.1. Proto-scale flow and discharge jet diameter are shown in the parenthesis.

Flow rate	P1	P2	P3	P4	P5
25 mm (0.75 m)	0.72	0.43	0.21	0.10	0.07
45 mm (1.35 m)	0.61	0.24	0.17	0.07	0.05
65 mm (1.95 m)	0.69	0.35	0.36	0.13	0.08

Table 5.4. Axial diffusivities (m^2/s) at each slice as shown at Figure 5.1. Proto-scale discharge jet diameters are shown in the parenthesis.

Flow rate	P1	P2	P3	P4	P5
25 mm (0.75 m)	0.19	0.22	0.14	0.12	0.15
45 mm (1.35 m)	0.16	0.13	0.12	0.08	0.11
65 mm (1.95 m)	0.18	0.18	0.25	0.16	0.18

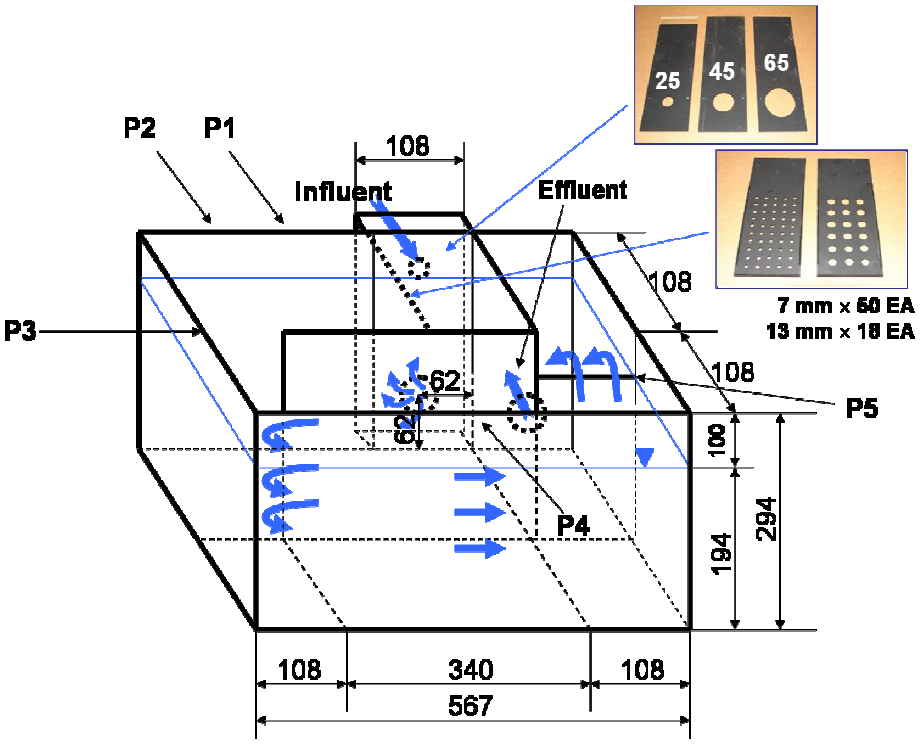

Figure 5.1. Dimension, geometry, and flow direction of the physical scale model ozone contactor. P1, P2, P3, and P4 are the slices for normalized residence time distributions.

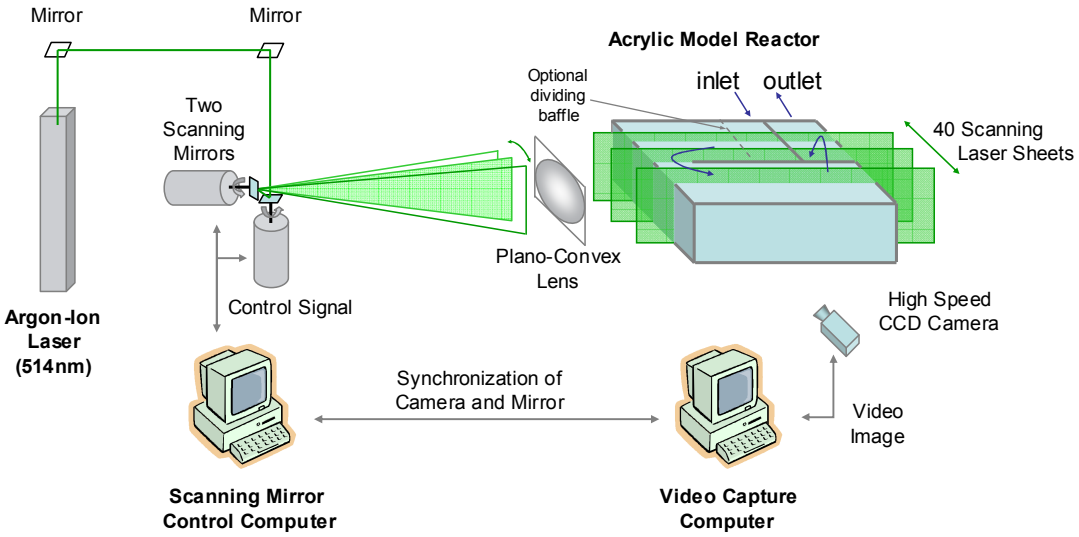

Figure 5.2. Schematic diagram of 3D-LIF system

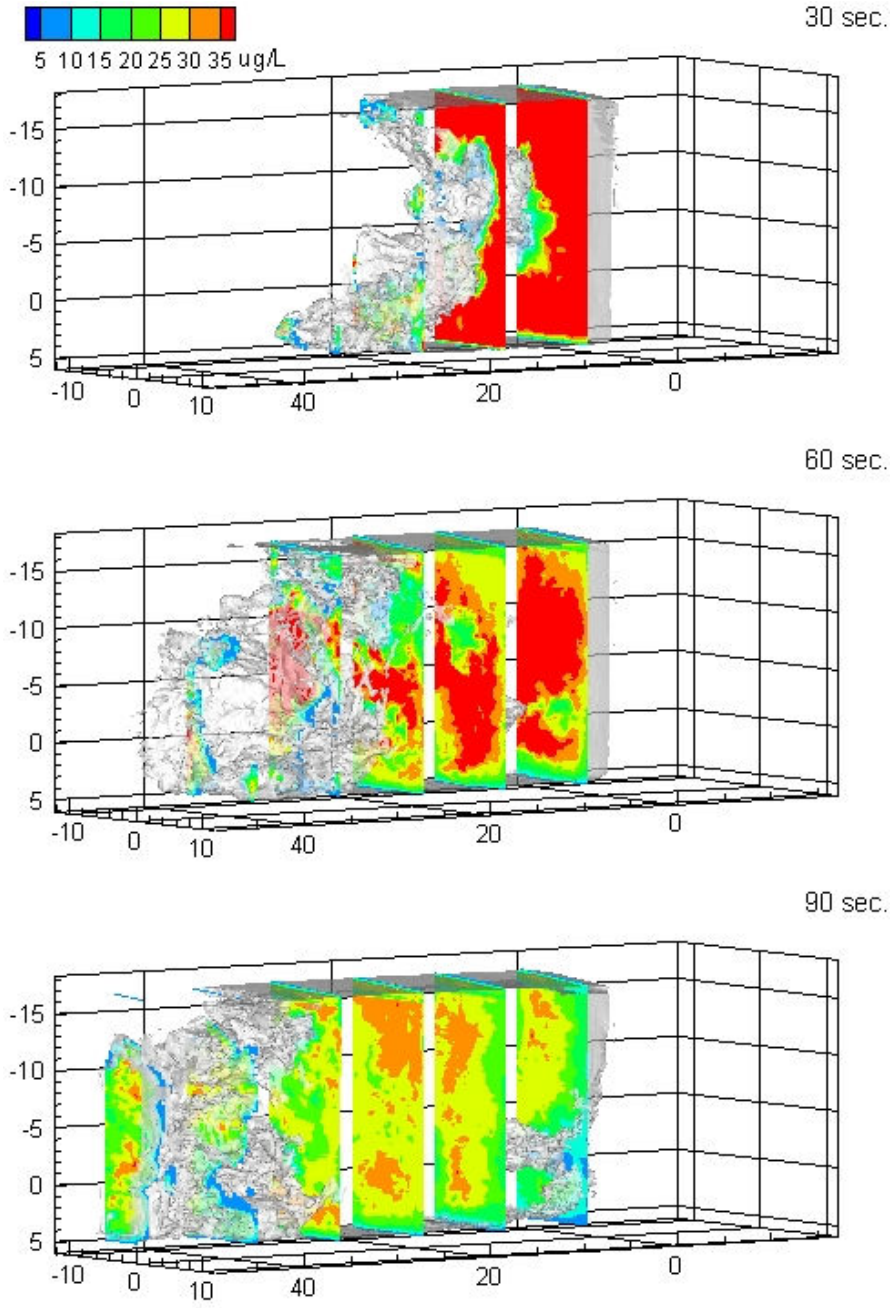

Figure 5.3. Rhodamine 6G transport behavior over time at the first chamber. This figure illustrates three dimensional dye concentration profiles at 30, 60 and 90 seconds after dye pulse injection for 95,000 m^3/day flow and 1.35 m influent jet diameter (AS05). unit: cm

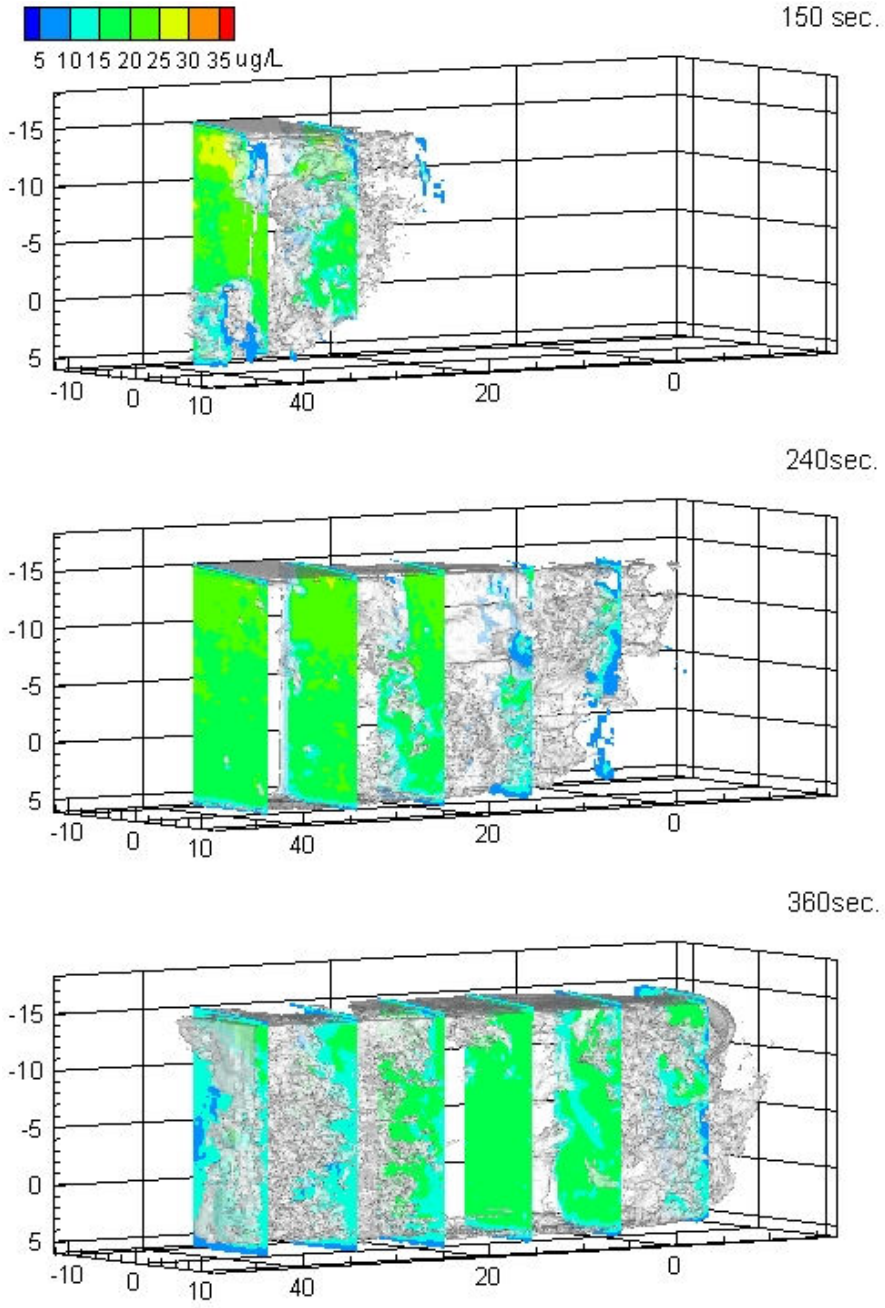

Figure 5.4. Rhodamine 6G transport behavior over time at the first chamber. This figure illustrates three dimensional dye concentration profiles at 150, 240 and 360 seconds after dye pulse injection for 95000 m^3/day flow and 1.35 m influent jet diameter (AS05). unit: cm

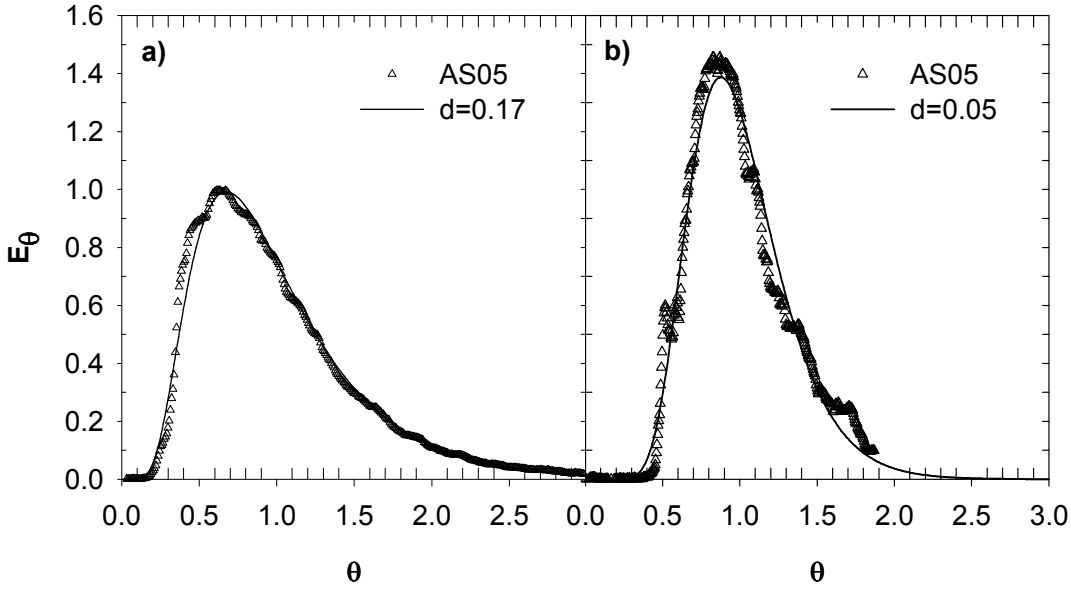

Figure 5.5. Residence time distribution (RTD) curve for AS05 and ADR model plot at the first ozone contactor for a) and the second ozone contactor for b).

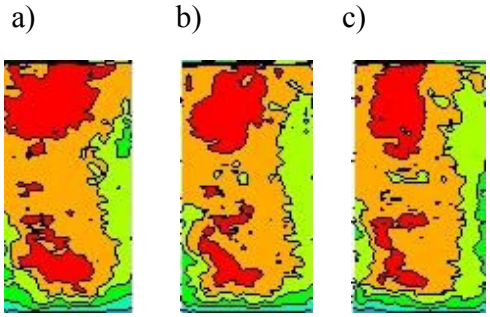

Figure 5.6. Longitudinal swirling flow over time 90 – 0.4 seconds for a), 90 seconds for b), and 90 + 0.4 seconds for c) with experimental condition, AS05. Note that upper swirl rotates counter-clockwise and lower swirl rotates clockwise.

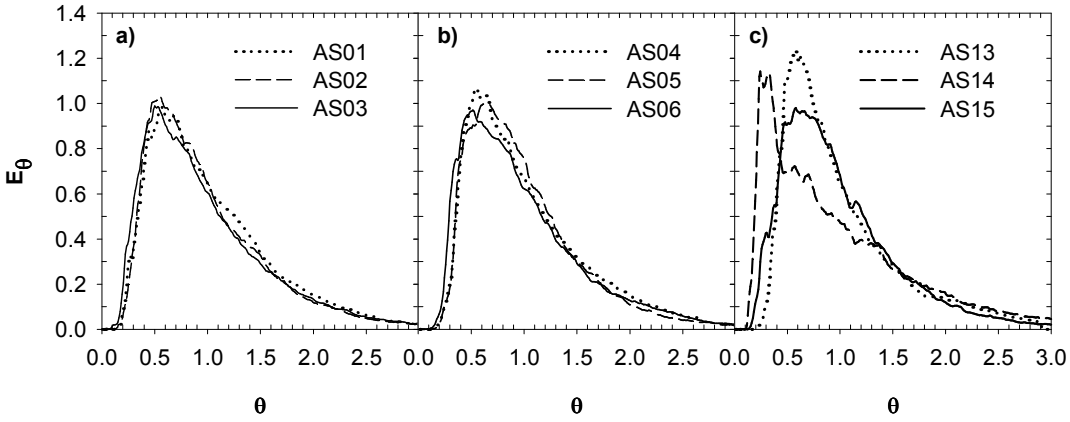

Figure 5.7. Normalized residence time distribution curve influent jet 0.75 m for a); 1.35 m for b); and 1.95 m for c)

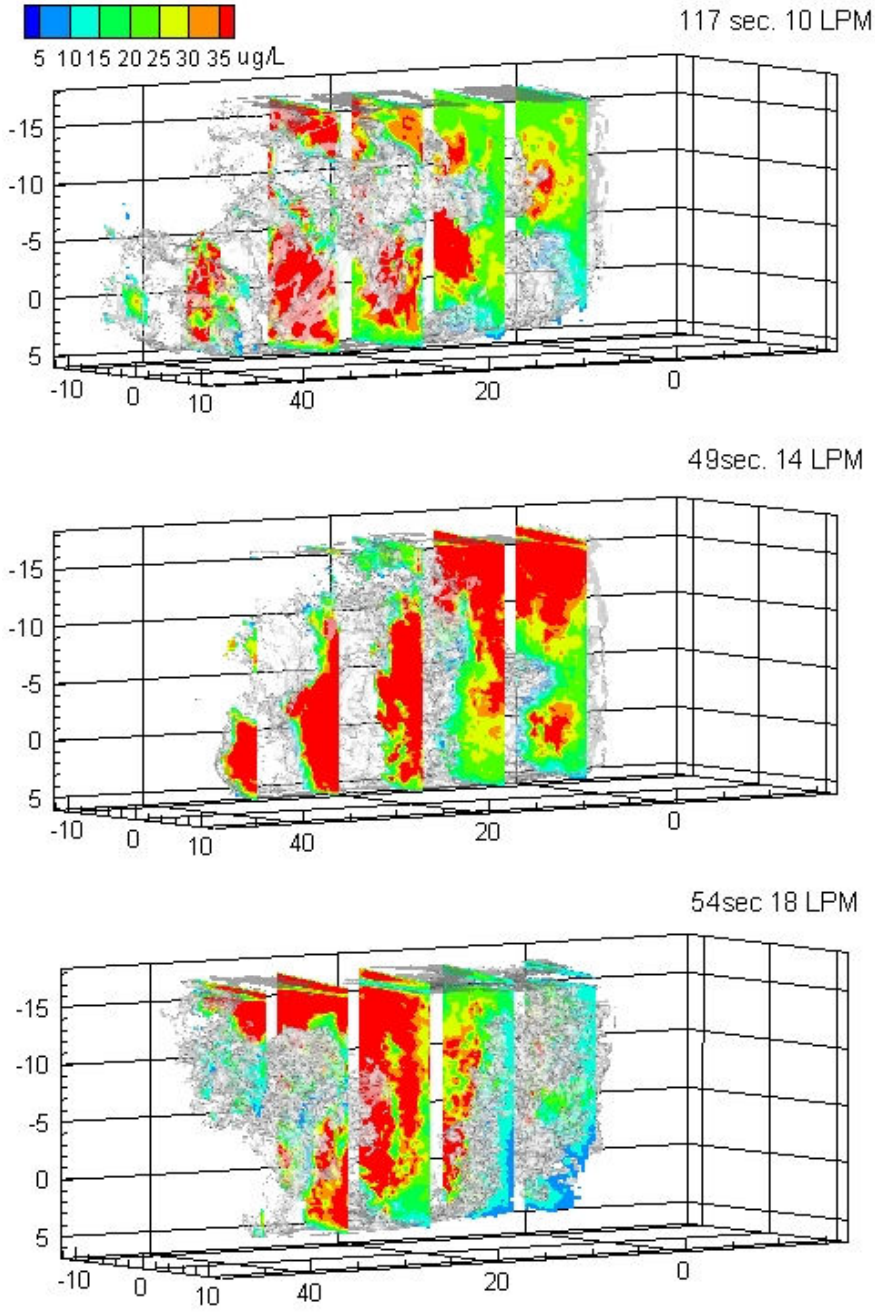

Figure 5.8. Conservative dye transport at the first chamber with three different flow rates and 1.95 m jet at time equivalent to T_1. 10, 14, and 18 LPM is equivalent to 71000, 95000, and 130000 m^3/day, respectively. (unit: cm)

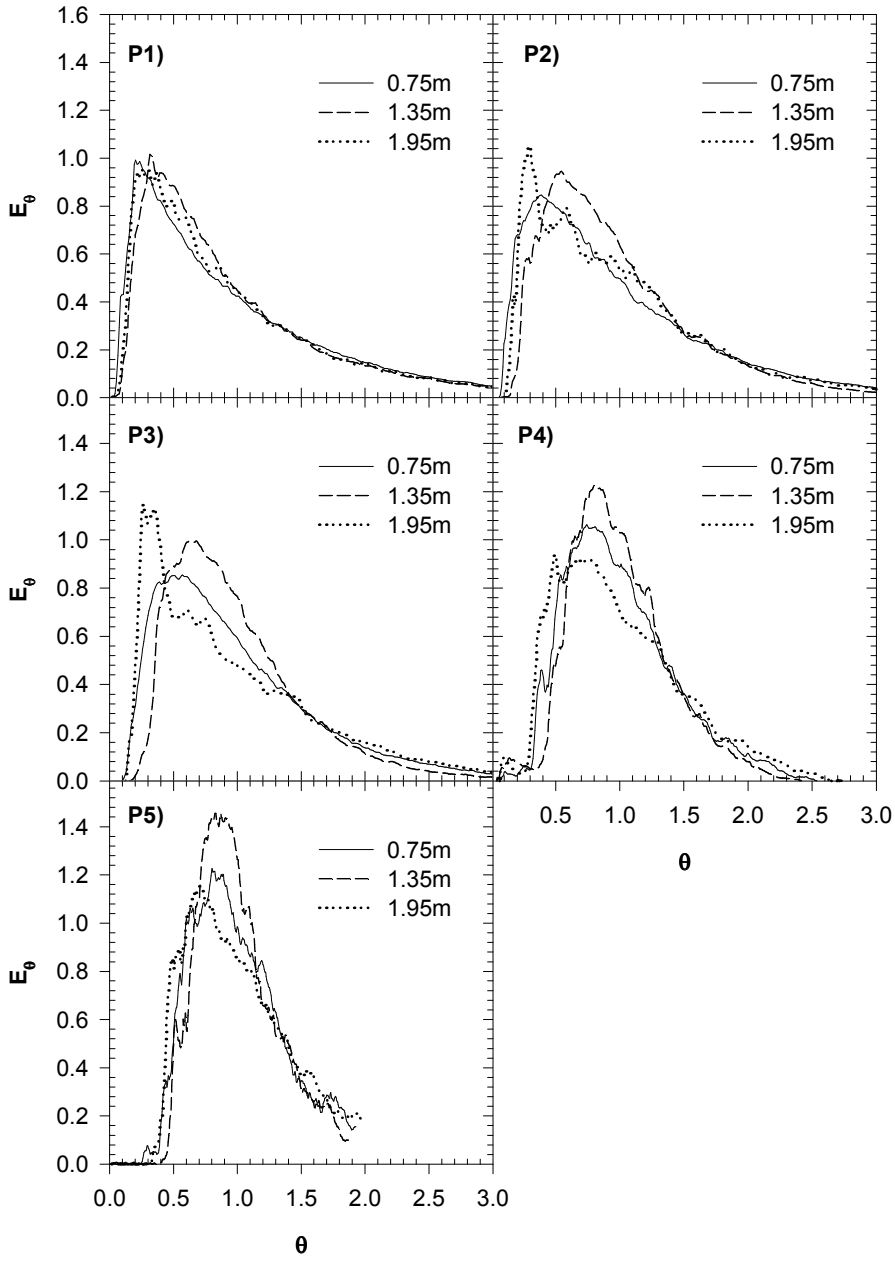

Figure 5.9. Normalized residence time distribution curve for five slices designated at Figure 5.1 with 95,000 m^3/day flow rate

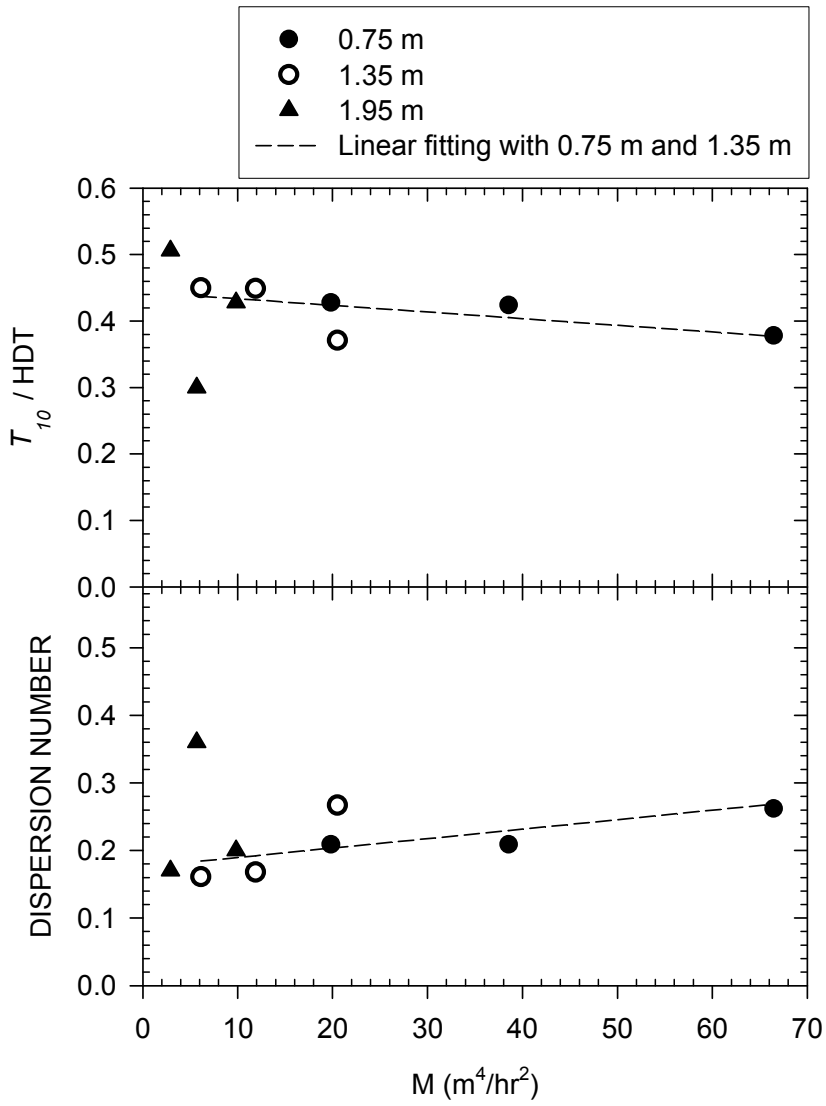

Figure 5.10. Axial dispersion number (d) and T_{10}/HDT over momentum flux (M) at P3 for 0.75, 1.35, and 1.95 m influent discharge jet diameter and design flow rate

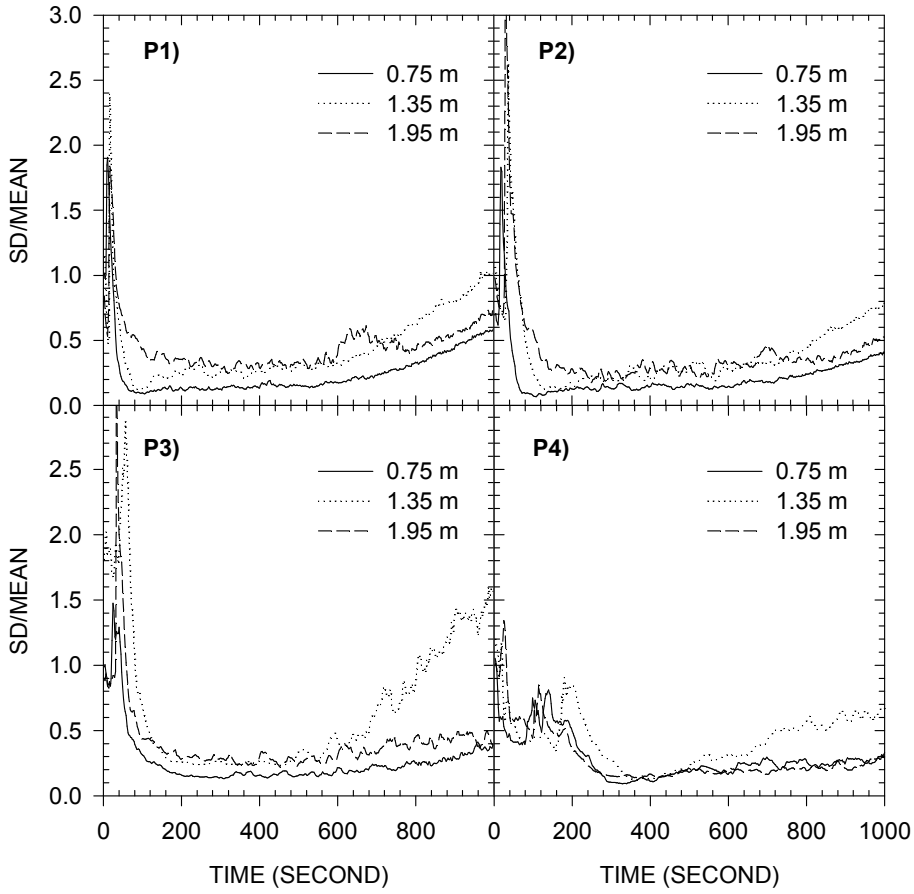

Figure 5.11. The COV changes over time for four slices designated at Figure 5.1 with 95,000 m^3/day flow rate

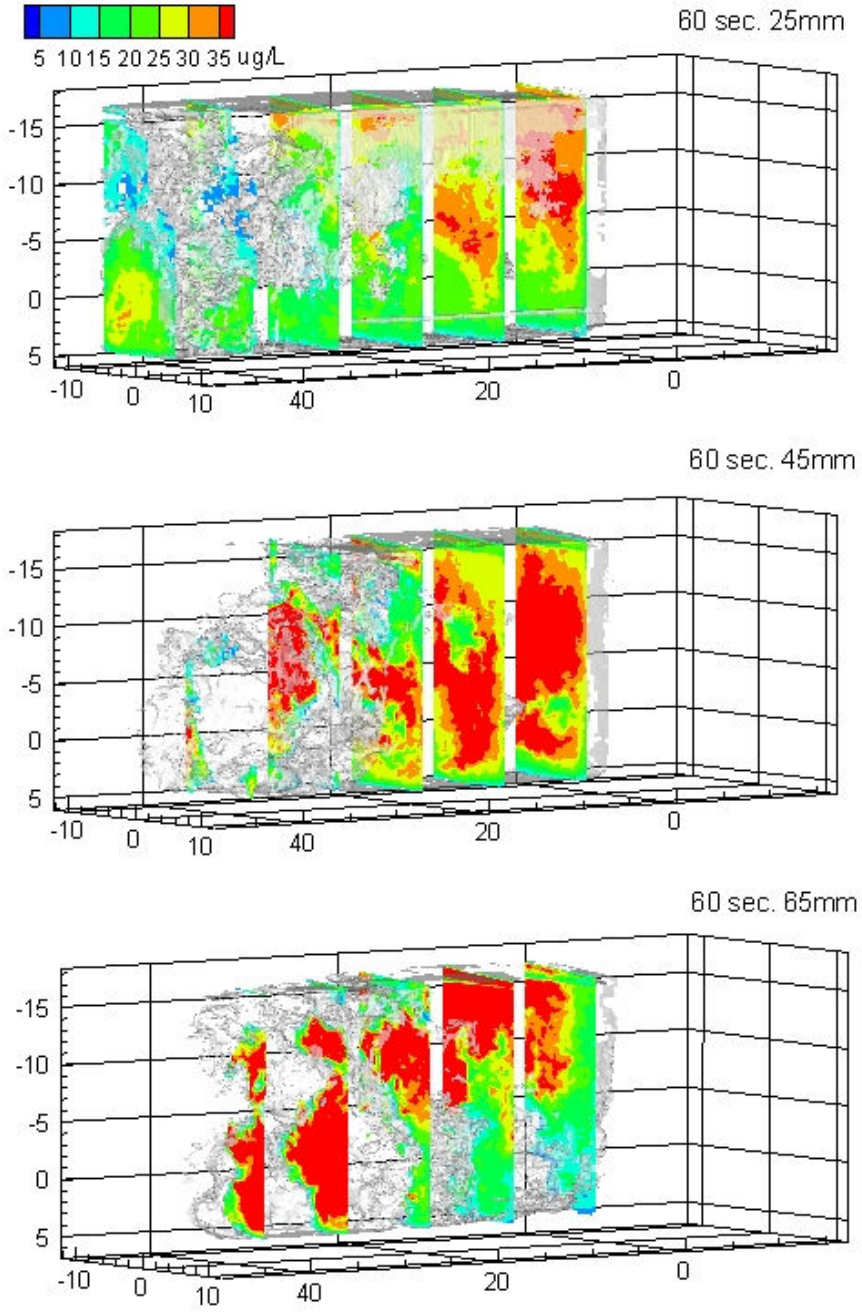

Figure 5.12. Conservative dye transport at the first chamber with three different influent pipe diameters after 60 seconds of dye injection with 95,000 m^3/day flow. 25, 45, and 65 mm jet is equivalent to 0.75, 1.35, and 1.95 m jet in proto-scale, respectively.

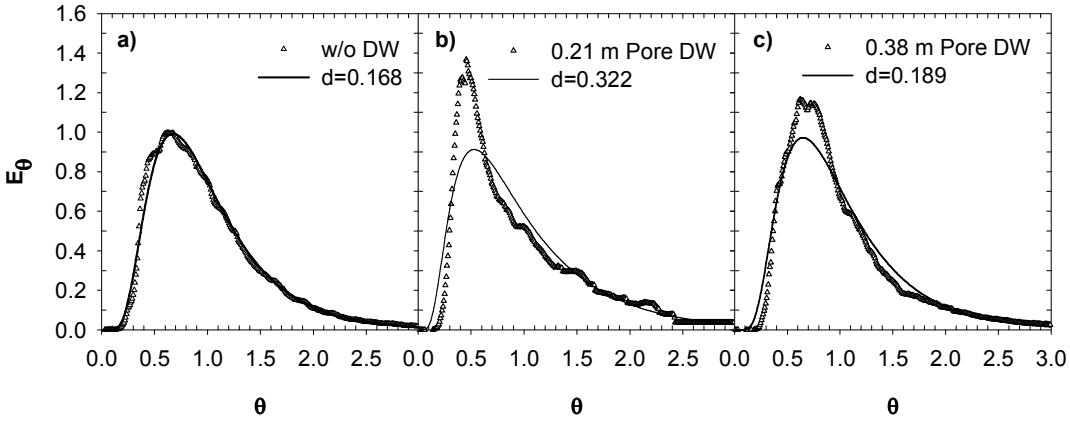

Figure 5.13. Residence time distribution curve for three different diffusion wall (DW) configurations at the first chamber (AS05, AS08, AS11). Without diffusion all for a); 0.21 m pore diffusion wall for b); and 0.38 m pore diffusion wall for c)

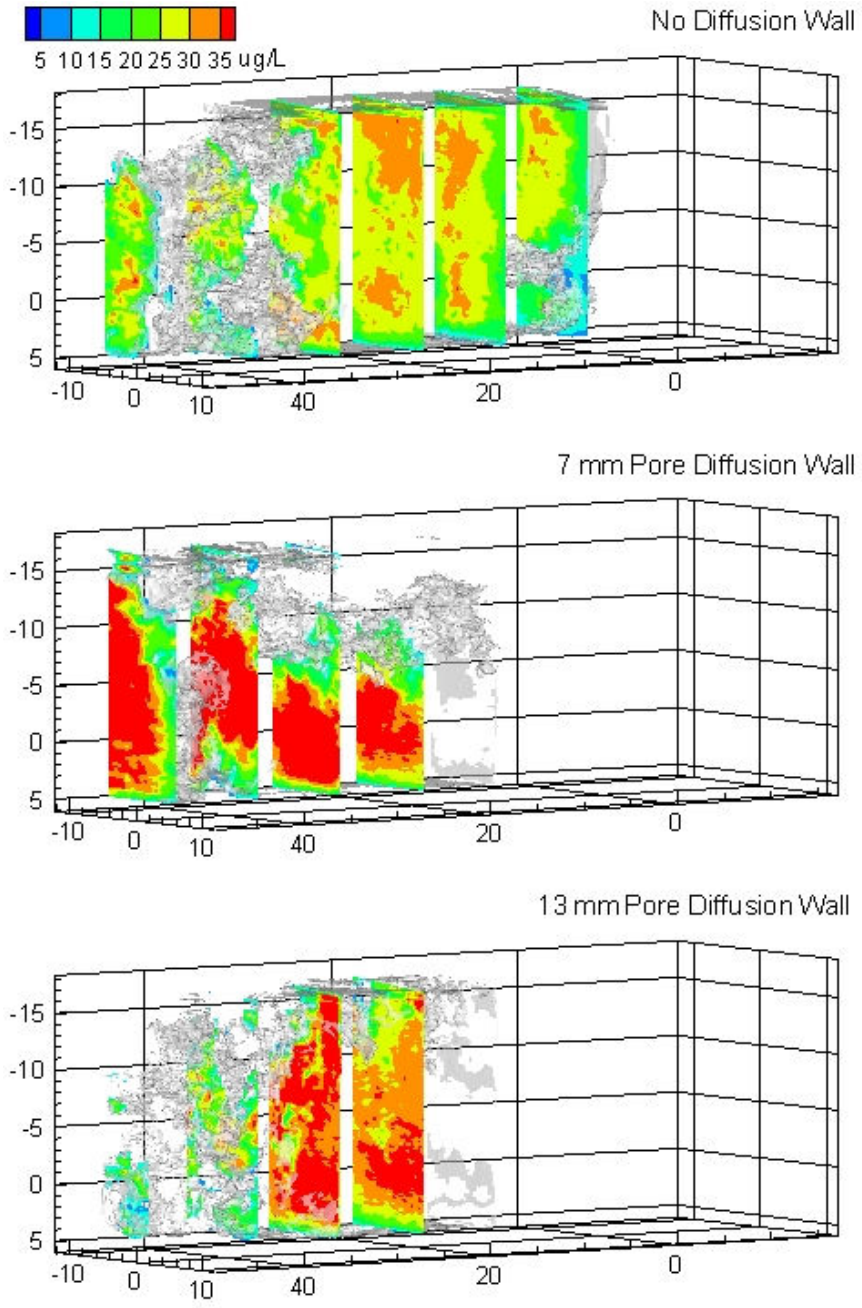

Figure 5.14. Conservative dye transport at the first chamber with different diffusion wall configurations using 95,000 m^3/day flow and 1.35 m inlet pipe diameter after 90 seconds after dye injection. 7 mm and 13 mm is equivalent to 0.21 m and 0.38 m in proto-scale, respectively.

CHAPTER 6

INVESTIGATING MIXING IN MULTI-CHAMBERED OZONE CONTACTORS USING 3-D LASER-INDUCED FLUORESCENCE

6.1. Introduction

The city of Milwaukee, Wisconsin, experienced a massive outbreak of *C. parvum*, which causes severe water-born gastrointestinal disease (*i.e.* Cryptosporidiosis) in humans (Finch & Belosevic, 2001), from its drinking water supply in April 1993 (Widmer, et al, 1996). After the outbreak, the city of Milwaukee retrofitted the Linnwood water treatment plant, which was carefully redesigned to prevent the occurrence of *C. parvum* oocyst in product water through primary disinfection with ozone. The Linnwood Water Plant Ozone Facility (LWPOF) has a maximum capacity of 275 MGD and four identical ozone contactors, each consisting of twelve chambers. A cross-sectional schematic diagram of the ozone contactors is shown in Figure 4.3. The dimension, volume, and flow direction of the contactor are summarized at Table 6.1. The overall contactor volume is 128,000 $ft^{3,}$ or 0.957 MG. The first chamber is equipped with 83 fine bubble diffusers installed at the bottom and serves as a contacting chamber. The second to the twelfth chambers serve as reactive chambers.

The hydrodynamics of the LWPOF is characterized by consecutive downward and upward flows through its twelve chambers. Such a serpentine-like flow pattern is used to achieve the higher number of CSTRs in CSTR-in-series model analysis, lower dispersion number (d) in axial dispersion reactor model analysis, and higher T_{10}/HDT (Roustan, et al, 1993; Do-Quang, et al, 2000). Note that the level of back-flow significantly affects on the disinfection efficacy, disinfection by-product formation, and ozone consumption (Roustan, et al, 1993; Kim, et al, 2007). T_{10}/HDT is one of critical parameters of the

design and operation of the current ozone contactor (USEPA, 1991). However, non-ideal flow characteristics incorporated in a full-scale plant could deteriorate the mixing conditions, resulting in the lower equivalent number of CSTRs in series, higher dispersion number, and lower T_{10}/HDT (El-Din & Smith, 2001;Greene, et al, 2004). Back-flow, stagnant zone, and short-circuiting are major hydrodynamic characteristics causing non-ideal flow in an ozone contactor (Heathcote & Drage, 1995;Henry & Freeman, 1995;Hannoun, et al, 1998;El-Din & Smith, 2001).

Recent studies of ozone contactor hydrodynamics using computational fluid dynamics have also predicted the possible existence of short-circuiting and back-flow in the up and downward flow ozone contactors (Henry & Freeman, 1995; Murrer, et al, 1995). It was shown that short-circuiting could deteriorate the dispersion number and the T_{10}/HDT values, which are keys for an ozone contactor design from their study. Continuous and circulative back-flow could entrap mass, which causes tailing and a lower peak height of the tracer residence time distribution (RTD) curve with pulse injection (Levenspiel, 1999). Thus, non-ideal flow should be avoided so that disinfection efficacy is maximized and disinfection by-product formation is minimized (Kim, et al, 2006).

Conservative tracer tests for RTD curves are commonly carried out at the test run stage of a new ozone contactor. Figure 4.5 shows normalized RTD curves obtained with several flow rates from the ozone contactors of the LWPOF. The results show that measured RTD curves are lower around the peak and higher at the tail than the theoretical ten CSTR in series model. However, understanding the exact mixing conditions within reactor is very challenging with conventional exit tracer studies. The research objective of this chapter is to prove experimentally non-ideal flow in the Linnwood ozone

contactor and to analyze the effect of the baffle opening and the flow rate on non-ideal flow formation using 3D-LIF technique.

6.2. Experimental Method

6.2.1. Physical Model Reactor of the Linnwood Ozone Contactor

The Linnwood ozone contactor is scaled down into a physical model using Froude number similarity on a 1/40 scale, as shown at Figure 6.1. Each physical parameter is related by the Buckingham π-theorem using Equation (5.3) (Munson, et al, 1998). The physical model and the Linnwood ozone contactor share each π-term in Equation (5.3). Physical model scales are obtained by multiplying the following scale factors to the scale of Linnwood: length scale = 1/40, velocity scale = $(1/40)^{1/2}$, time scale = $(40)^{1/2}$.

6.2.2. Conservative Tracer Test with 3D-LIF

Experimental methods described in section 5.2.3 are used for the conservative tracer test with the 3D-LIF system. Briefly, de-chlorinated water is fed into the physical model reactor at room temperature (20±2^{o}C). 1 mL of laser-dye stock solution (i.e., 100 mg/L of Rhodamine 6G purchased from Sigma-Aldrich, St. Louise, MO) is directly pulse-injected using a syringe into an influent pipe. Scanning forty laser slices of a 1.75 W Argon-ion laser (514nm) is created using two oscillating mirrors that are controlled by the computer. The laser sheet excites the fluorescent dye located in their plane. A high-speed CCD camera captures images at the rate of forty frames per second and stores them in a large capacity storage device using Video Savant® Software (IO Industries, Inc., Ontario Canada). Image capture is initiated instantaneously after the dye injection and lasts for 8 to 15 minutes. The size of the captured image stream file ranges from 5.0 to 10 GB, depending on the duration time. Simultaneous image calibration and attenuation error correction are carried out by means of capturing video images of 25 and 50 μg/L rhodamine 6G solutions, which fills the entire physical model reactor, with the same

condition for the conservative tracer tests using 3D-LIF. The entire image is averaged pixel by pixel using Video Savant® software (IO industries Inc., Ontario Canada) and then corrected for the vignetting error using *TFlook* software version 2007, followed by correcting the attenuation error (Tian & Roberts, 2003). The linear correlation coefficient between the Rhodamine 6G concentration and the pixel intensity is expressed by Equation (2.29).

6.2.3. Conservative Tracer Test with Conductivity

The conservative tracer test using a conductivity meter (YSI 3200, Yellow Springs, Ohio) is also carried out with the physical model reactor. The tracer test is initiated by pulse injecting 10 mL of 100 g/L Sodium Chloride stock solution into the influent pipe using a syringe. Conductivity of the reactor effluent is measured every five seconds and transferred to a personal computer and then stored in the storage device for three times the hydraulic detention time.

6.3. Results and Discussion

6.3.1. Attenuation Correction

Attenuation is a loss of laser intensity during travel in water containing laser dye, which is pronounced in a lengthy physical model reactor. Beer's Law, shown at Equation (6.1), fitted well with 50 μg/L Rhodamine 6G solution after vignetting correction as shown at Figure 6.2. In this figure, a downward peak is caused from the acrylic baffle, which has no Rhodamine 6G inside. The attenuation factor used for Rhodamine 6G is 0.00023 L/μg/cm from (Tian & Roberts, 2003) and that for water, 0.0102 cm^{-1}, is obtained as shown at Figure 6.2 after vignetting correction using Equation (6.1). Attenuation for water is much higher than 0.0011 - 0.0045 cm^{-1} suggested by Tian and Roberts (2003). The difference is thought to be caused by variations in water quality from experiment to experiment. The effect of acrylic material on laser attenuation is

unknown. If the acrylic baffle causes significant attenuation, a stepwise decrease will be expected next to each baffle. From Figure 6.2, attenuation by the acrylic baffle is thought to be almost negligible. Overall attenuation by water and Rhodamine 6G could be expressed by Equation (6.2).

$$P = P_0 e^{-a(x-x_0)} \tag{6.1}$$

$$a = a_w + 0.00023 \times C \tag{6.2}$$

where P and P_0 represent relative laser intensity at location x and x_0 (cm), respectively, a is the attenuation factor (cm^{-1}), and a_w is the clear water attenuation coefficient (cm^{-1}), and C is the Rhodamine 6G concentration (μg/l).

6.3.2. Reproducibility of 3D-LIF Experiments

Six tracer tests for reproducibility of the 3D-LIF experiments are carried out using the physical model plant in identical conditions. The dispersion number (d) is compared for the reproducibility of 3D-LIF because it is the most frequently used hydrodynamic characteristics of an ozone contactor, obtained using Equations (6.3) and (6.4). The value of d will be solved iteratively substituting values of τ and σ^2, calculated by Equations (6.3) and (6.5), respectively.

$$\tau = \frac{\int_0^\infty tcdt}{\int_0^\infty cdt} \approx \frac{\sum_{i=0}^{i=\infty} t_i c_i \Delta t}{\sum_{i=0}^{i=\infty} c_i \Delta t} \tag{6.3}$$

$$2d - 2d^2\left(1 - \exp\left(-\frac{1}{d}\right)\right) = \frac{\sigma^2}{\tau^2} \ , \tag{6.4}$$

where Δt is the time interval between samples. The corresponding second moment about the mean, the variance σ^2, is:

$$\sigma^2 = \frac{\int_0^\infty (t-\tau)^2 c\,dt}{\int_0^\infty c\,dt} \approx \frac{\sum_{i=0}^{i=\infty} t_i{}^2 c_i \Delta t}{\sum_{i=0}^{i=\infty} c_i \Delta t} - \tau^2 \tag{6.5}$$

The third moment about the mean, the skewness, γ^3, is:

$$\gamma^3 = -\frac{\int_0^\infty (t-\tau)^3 c\,dt}{\int_0^\infty c\,dt} \approx \frac{\sum_{i=0}^{i=\infty} t_i{}^3 c_i \Delta t}{\sum_{i=0}^{i=\infty} c_i \Delta t} - 3\bar{t}\,\sigma^2 - \tau^3 \tag{6.6}$$

Another measure of experimental reproducibility is the coefficient of variation (COV). The COV, a measure of the degree of mixing in the reactors, is defined as the ratio of the standard deviation of the tracer concentrations to the mean concentration:

$$COV = \frac{\text{Standard Deviation of Tracer Concentrations}}{\text{Mean Tracer Concentration}} = \frac{\sqrt{\frac{1}{n-1} \times \sum_{i,j,k}\left(C(x_i, y_j, z_k, t) - \frac{1}{n} \times \sum_{i,j,k} C(x_i, y_j, z_k, t)\right)^2}}{\frac{1}{n} \times \sum_{i,j,k} C(x_i, y_j, z_k, t)} \tag{6.7}$$

where n is the number of data and i, j , and k are pixel index.

Tables 6.2 shows the dispersion numbers of ten chambers from the six tracer tests with pulse injection with syringe. Dispersion numbers are acquired up to the tenth chamber because dispersion numbers from the tenth chamber is available from full scale plant and the image covers only from the first to the tenth chamber for the width of the physical model scale pant and limitation of distance between the object and the camera. The average, the standard deviation (σ^2), the skewness (γ^3), and the COV of the dispersion number are analyzed for each chamber using six experimental results. The highest covariance (COV), 7%, is observed at the first ozone chamber and decreases as the number of the chamber increases. Figure 6.3 shows a normalized RTD for the representative second, sixth, and tenth chambers with error range represented with standard deviation (σ). These results show that conservative tracer tests using the 3D-LIF system are very reliable and reproducible for dispersion number and residence time.

6.3.3. Comparing Physical Model Plant with the Linnwood Plant Using Residence Time Distribution (RTD) Curves

Hydraulic model study scaled down from the full scale plant needs to be verified through comparison with results from both plants. Normalized RTD curves of the Linnwood plant and the physical model plant are compared at two flow rates in Figure 6.4. 6 L/min and 12 L/min in the physical model reactor is equivalent to 23 MGD and 45 MGD of the Linnwood plant respectively. RTD curves from the full scale plant are shown at Figure 4.5. The tracer test method is described in detail in Section 4.3. The normalized RTD curve from the physical model shows a slight discrepancy around the peak compared to that from the Linnwood ozone contactor, but it matched well at the other regions for two flow rates. From these comparisons, scale down with Froude number is quite affordable to simulate RTD of the full scale plant. However, as this comparison only carried with the results from the tenth chamber, the limitation should not be underestimated to extend this result to each chamber.

6.3.4. Hydrodynamic Characteristics of Each Chamber from the Physical Model Contactor

Conservative laser dye mixing and transport behavior over time from the first to the tenth chambers is shown at Figure 6.5, 6.6, and 6.7. The images are obtained after dye pulse injection using syringe. Figure 6.5 shows that as the dye is introduced through the overflow weir into the first chamber, the dye plume flows fast along the surface and is then redirected downward by the opposing baffle. It is then split into two portions, one part of which flows through the underflow baffle in the second chamber, forming short-circuiting, and the other of which flows back, forming back-flow circulation. These flow characteristics persist to the last chamber, as shown in Figures 6.6 to 6.7.

The existence of non-ideal flow of the Linnwood ozone contactor could be expected by comparing the normalized RTD curves and the ten CSTR in series model as shown at Figure 4.5. However, it is nearly impossible to analyze non-ideal flow condition in each individual chamber by only tracer results obtained at the tenth chamber. Therefore, normalized RTD curves from each chamber could be constructed from the data obtained using the 3D-LIF at 12 L/min flow with the physical scale model reactor, as shown at Figure 6.8. Two clear peaks appear from the first to fifth chamber, which is related to the non-ideal flow such as short-circuiting and back-flow (Levenspiel, 1999).

Although all the chambers share similar hydrodynamics, a noticeable short-circuiting peak appears only on the RTD curves of the first to the fifth chambers, but it does not appear on the remaining chamber. This is because the dye concentration within the first five chambers is relatively high enough to be identified as a peak while the dye concentration from the later chambers is quite dispersed and low. A single peak from the

sixth chamber implies that the short-circuiting effect is almost compensated if the number of ozone chambers is greater than six.

As the results of non-ideal flow (i.e. short-circuiting and back-flow) the observed dispersion number of the Linnwood ozone contactor is larger than the theoretical dispersion number obtained from N CSTR in series model expressed as Equation (6.8). Figure 6.9 compares observed dispersion numbers obtained from the physical model reactor using 3D-LIF at 12 L/min and those from N CSTR in series model. Dispersion numbers of N CSTR in series is acquired using Equation (6.4) by fitting normalized RTD curves expressed by Equation (6.8). Equation (6.9) proposed by Villermaux (1982) could also be used to obtain dispersion number of N CSTR in series model but produces slightly lower values. After careful calculation, Equation (6.9) is recommended to be replaced with Equation (6.10) for better fitting. Considerable discrepancy between theoretical and observed dispersion number is shown at Figure 6.9. This could result in decreased disinfection efficacy and require more ozonation chambers for the same efficiency. For example, if the target dispersion number is 0.2, three chambers in series are required if chambers are fully CSTR from Figure 6.9 but five tanks are practically needed because of non-ideal flow. Likewise, if the target dispersion number is 0.1, the Linnwood plant would require four more chambers than the ideal CSTR in series. This discrepancy could be reduced by switching each chamber closer to the ideal CSTR through various design options.

$$E(\theta) = J\frac{(J\theta)^{J-1}}{(J-1)!}e^{-J\theta} \tag{6.8}$$

where E is the normalized concentration, θ is the normalized time, and J is the number of chambers.

$$Pe = \frac{1}{d} = 2.0 \times N + 1 \quad (6.9)$$

$$Pe = \frac{1}{d} = 1.73 \times N + 1 \quad (6.10)$$

where Pe is Péclet number and N is the number of chambers.

6.3.5. Effect of the Flow Rate

Effects of three flow rates, 6, 12, and 18 L/min, equivalent to 23, 43, and 68 MGD for the Linnwood plant, respectively, were compared with the key hydrodynamic parameters for disinfection (i.e. dispersion number (d) and T_{10}/HDT values). The normalized RTD curves from the representative first, second, fourth, sixth, and tenth chambers of physical model reactor are compared in Figure 6.10. From this figure, three different flow rates show similar peaks for most cases. Normalized RTD from the tenth chamber of the Linnwood plant is also shown to be similar from the tenth chamber of this figure. Dispersion numbers, however, are quite different especially at the second chamber as shown at Table 6.3. Dispersion numbers increase with flow rate and their dependence on flow rate becomes smaller as the number of chambers increase because of buffering effect of multi-chamber design. Unlike dispersion number, T_{10}/HDT remains almost constant regardless of flow rate.

Diffusivity at each chamber, as shown at Figure 6.11, increases with flow rate because it is proportional to axial velocity from Equation (6.11). It is interesting to note that diffusivities of four chambers (i.e. the second, fourth, sixth, and tenth chamber) are almost the same at 6 L/min but it becomes quite different at 12 L/min and 18 L/min. Diffusivities of ideal CSTR in series could be expressed by Equation (6.12) and increase

with the number of chamber (*N*) at a given flow rate and axial length. The observed diffusivities, however, decrease with the number of chamber (*N*) because observed dispersion number (*d*) is much larger than theoretical dispersion number with the smaller number of chamber and the difference decrease with the number of chamber as shown at Figure 6.9. Therefore, higher diffusivity from smaller number of chamber at 12 L/min and 18 L/min is attributable to non-ideal flow hydrodynamics (i.e., short-circuiting and circulative back-flow). At higher flow rate (12 and 18 L/min), relatively stronger back-flow circulation is formed at each chamber, which creates clearer double peak as shown at the first and second chamber of Figure 6.10. But lower flow rate (6 L/min) creates relatively weaker back-flow while short circuiting still exists. Figure 6.12 compares the mixing behavior of Rhodamine 6G at the second chamber and time equivalent to T_5 of the second chamber. T_5 is defined as time required for 5% of total dye pass through the reactor. Note more active back-flow at the second chamber at 12 and 18 L/min than 6 L/min, as evidenced by larger region with higher dye concentration at the second chamber wall facing the third chamber. Dispersion number is defined as:

$$d = \frac{D}{UL} \tag{6.11}$$

where *d* is dispersion number, *D* is diffusivity (L^2T^{-1}), *U* is axial velocity (LT^{-1}), and *L* is axial length (L). Diffusivity could be expressed as Equation (6.12) from equation (6.10) and (6.11).

$$D = d \times U \times L = \frac{1}{1.73N + 1} \times U \times N \times L_{each\ chamber} = U \times L_{each\ chamber} \times \frac{N}{1.73N + 1} \tag{6.12}$$

where *N* is the number of chamber, $L_{each\ chamber}$ is the axial length of each chamber(L).

6.3.6. Effect of Baffle Opening Size

The baffle opening size is defined as the distance between the bottom and the underflow weir or the depth between the free surface and the overflow weir. Three baffle opening sizes are compared: wide, normal, and narrow. "Normal" is the current size of the Linnwood ozone contactor, "wide" is twice the "normal" size, and "narrow" is half of current size. The opening size was thought to affect the mixing behavior because it affects on the influent momentum into the subsequent chamber. However, three different opening sizes show a minor difference when they are compared (Figure 6.13). The results for the dispersion number (d) and the T_{10}/HDT, summarized in Table 6.4, also confirm that the baffle openings did not affect on these parameters. The baffle opening size also does not affect COV at the second chamber from Figure 6.14. The reason why baffle opening does not affect these parameters could be explained using the specific energy defined as Equation (6.13):

$$E = h_1 + \frac{q^2}{2gh_1^2} = h_2 + \frac{q^2}{2gh_2^2} + \Delta E \qquad (6.13)$$

where E is specific energy (ML^2T^{-2}), h_1 and h_2 are water depth (L) before and after baffle respectively, q is flow rate per unit width (L^2T^{-1}), g is specific gravitational acceleration (LT^{-2}), and ΔE is specific energy loss (ML^2T^{-2}). Figure 6.15 illustrates the case where the left side of the baffle is filled with water and the water flow into the right side across the underflow weir. Note that water depth after underflow weir would be decided by specific energy regardless of baffle opening size. Therefore flow path after underflow weir is thought to be contracted or expanded according its specific energy. These contraction and expansion is observed at the fourth chamber of Figures 6.16, which shows dye mixing and transport behaviors for three different baffle opening sizes after 60 seconds from dye injection.

6.4. Conclusion

3D-LIF with a physical model reactor is proved to be a useful tool to analyze flow hydrodynamics of multi-chambered ozone contactor with fine bubble diffuser with high reliability and reproducibility. Visual observation of flow of each chamber using 3D-LIF clearly confirmed the existence of short-circuiting and internal recirculation due to back-flow. Experimental verification on such flow conditions in this popular reactor design is unprecedented to the author's knowledge. Because of non-ideal flow, the Linnwood ozone contactor has a larger dispersion number and lower T_{10}/HDT even compared to the ideal CSTR in series model, which might result in lower disinfection efficacy and more ozone consumption. Non-ideal flow resulting from this design would be more significant at the higher flow rate and especially when the number of chamber is smaller. Non-ideal flow in this design was not eliminated by relatively simple modification, including flow rate adjustment and baffle opening change. However, as this particular plant consists of large number of chambers, contribution of non-ideal conditions from each chamber to the overall hydrodynamics was "buffered" such that relatively low dispersion condition was achieved by the overall reactor. This study suggested that the reactor with smaller size with less number of chambers might be possible if the flow characteristics are optimized to yield more plug-flow like conditions.

Table 6.1 Dimension and flow direction of Linnwood Water Plant Ozone Facility

Chamber #	Physical Dimension					Water Flow Direction
	Length (ft)	Width (ft)	Depth (ft)	Cross Sectional Area(ft^2)	Design Vol. (ft^3)	
1	11.5	30	24	345.0	8280.0	downward
2	15.67	30	24	470.1	11282.4	upward
3	15.67	30	24	470.1	11282.4	downward
4	15.67	30	24	470.1	11282.4	upward
5	9.5	30	24	285.0	6840.0	downward
6	15.67	30	24	470.1	11282.4	upward
7	15.67	30	24	470.1	11282.4	downward
8	15.67	30	24	470.1	11282.4	upward
9	15.67	30	24	470.1	11282.4	downward
10	15.67	30	24	470.1	11282.4	upward
11	15.67	30	24	470.1	11282.4	downward
12	15.67	30	24	470.1	11282.4	upward
sum					127944	

Table 6.2 Dispersion number (*d*) and its standard deviation, skewness, and cov of six repeated tracer tests at 12 L/min.

	1st	2nd	3rd	4th	5th	6th	7th	8th	9th	10th
1	-	0.73	0.32	0.22	0.18	0.14	0.12	0.10	0.08	0.07
2	-	0.75	0.35	0.22	0.17	0.14	0.12	0.10	0.08	0.07
3	-	0.71	0.34	0.21	0.17	0.14	0.11	0.09	0.08	0.06
4	-	0.79	0.35	0.22	0.17	0.14	0.12	0.10	0.08	0.07
5	-	0.68	0.34	0.22	0.18	0.14	0.12	0.10	0.08	0.07
6	-	0.83	0.33	0.22	0.17	0.14	0.12	0.10	0.08	0.06
avg.	-	0.75	0.34	0.22	0.17	0.14	0.12	0.10	0.08	0.07
std. dev.	-	0.05	0.01	0.00	0.00	0.00	0.00	0.00	0.00	0.00
skewness	-	0.49	-0.67	-1.89	-0.45	-2.02	-0.68	-0.85	-1.62	0.32
cov	-	0.070	0.036	0.018	0.015	0.017	0.013	0.012	0.011	0.013

Table 6.3 Dispersion number (d) and T_{10}/HDT at the second, fourth, sixth, and tenth chamber for three flow rates.

Flow L/min	2nd		4th		6th		10th	
	d	T_{10}/HDT	D	T_{10}/HDT	d	T_{10}/HDT	d	T_{10}/HDT
6 (23 MGD)	0.36	0.25	0.21	0.36	0.14	0.44	0.07	0.56
12 (45 MGD)	0.62	0.22	0.23	0.36	0.15	0.44	0.08	0.54
18 (68 MGD)	0.80	0.25	0.29	0.35	0.17	0.43	0.09	0.53

Table 6.4 Dispersion number (d) and T_{10}/HDT at the second, fourth, sixth, and tenth chamber for three different baffle opening size at 12 L/min

Baffle Opening	2nd		4^{th}		6^{th}		10th	
	d	T_{10}/HDT	d	T_{10}/HDT	d	T_{10}/HDT	d	T_{10}/HDT
Wide	0.64	0.22	0.22	0.36	0.14	0.46	0.08	0.54
Normal	0.62	0.22	0.23	0.36	0.15	0.44	0.08	0.54
Narrow	0.48	0.23	0.21	0.36	0.14	0.45	0.08	0.54

a)

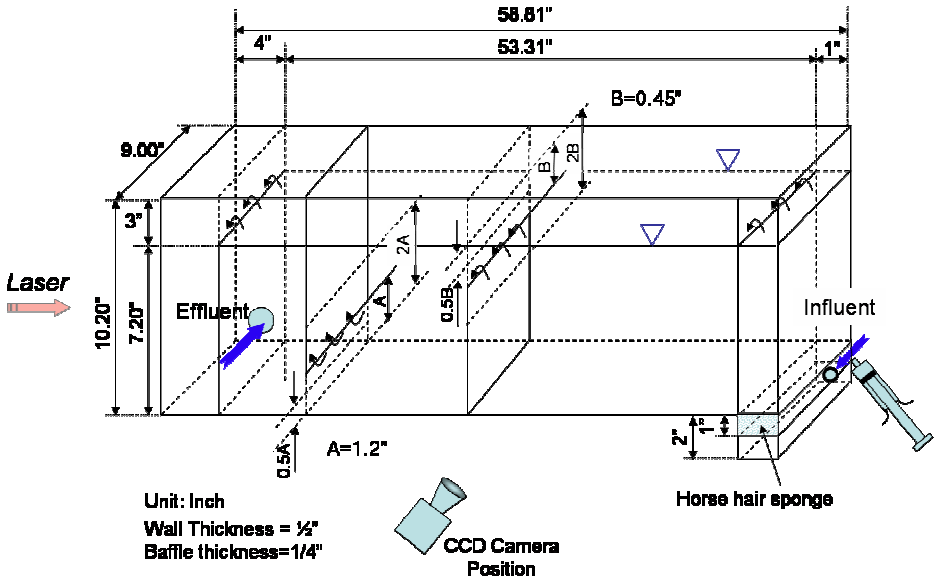

b)

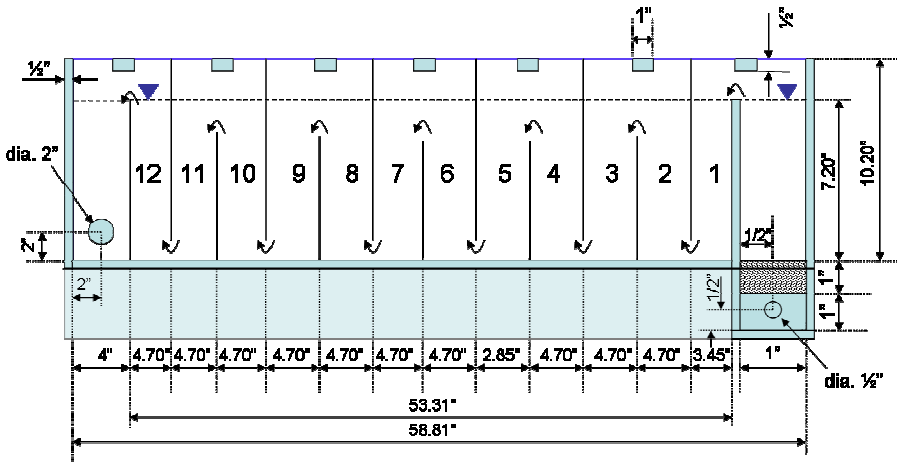

Figure 6.1. Dimension and shape of physical model reactor of the Linnwood ozone contactor for a), and cross sectional diagram for b)

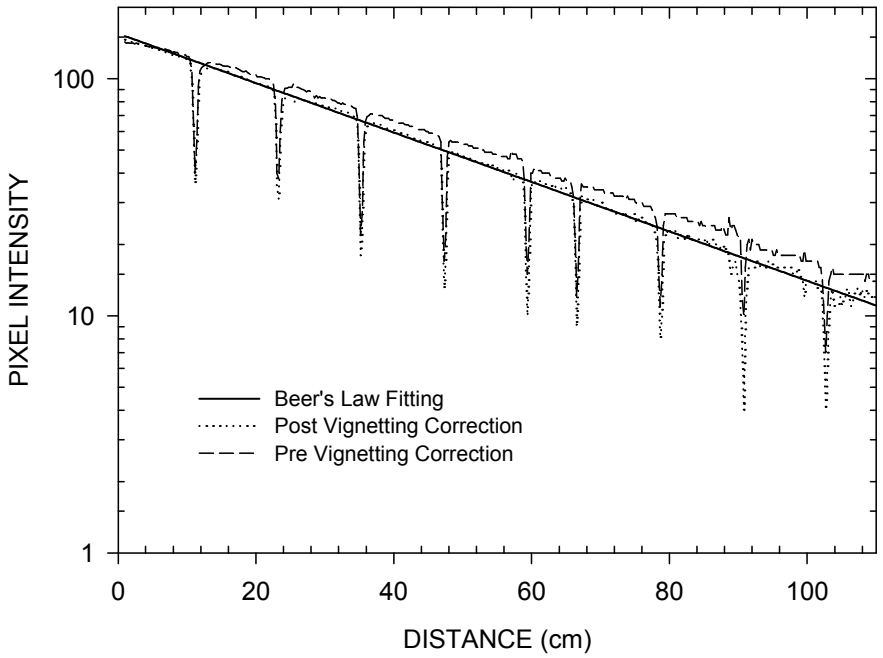

Figure 6.2. Attenuation after vignetting correction with 50 μg/L standard solution

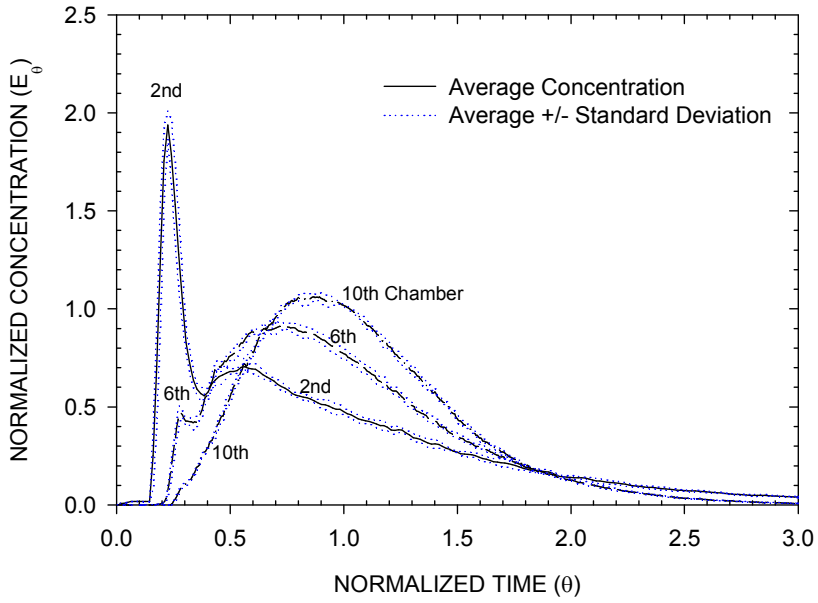

Figure 6.3. Normalized RTD curve represented with average concentration and standard deviations for the second, sixth, and tenth chamber

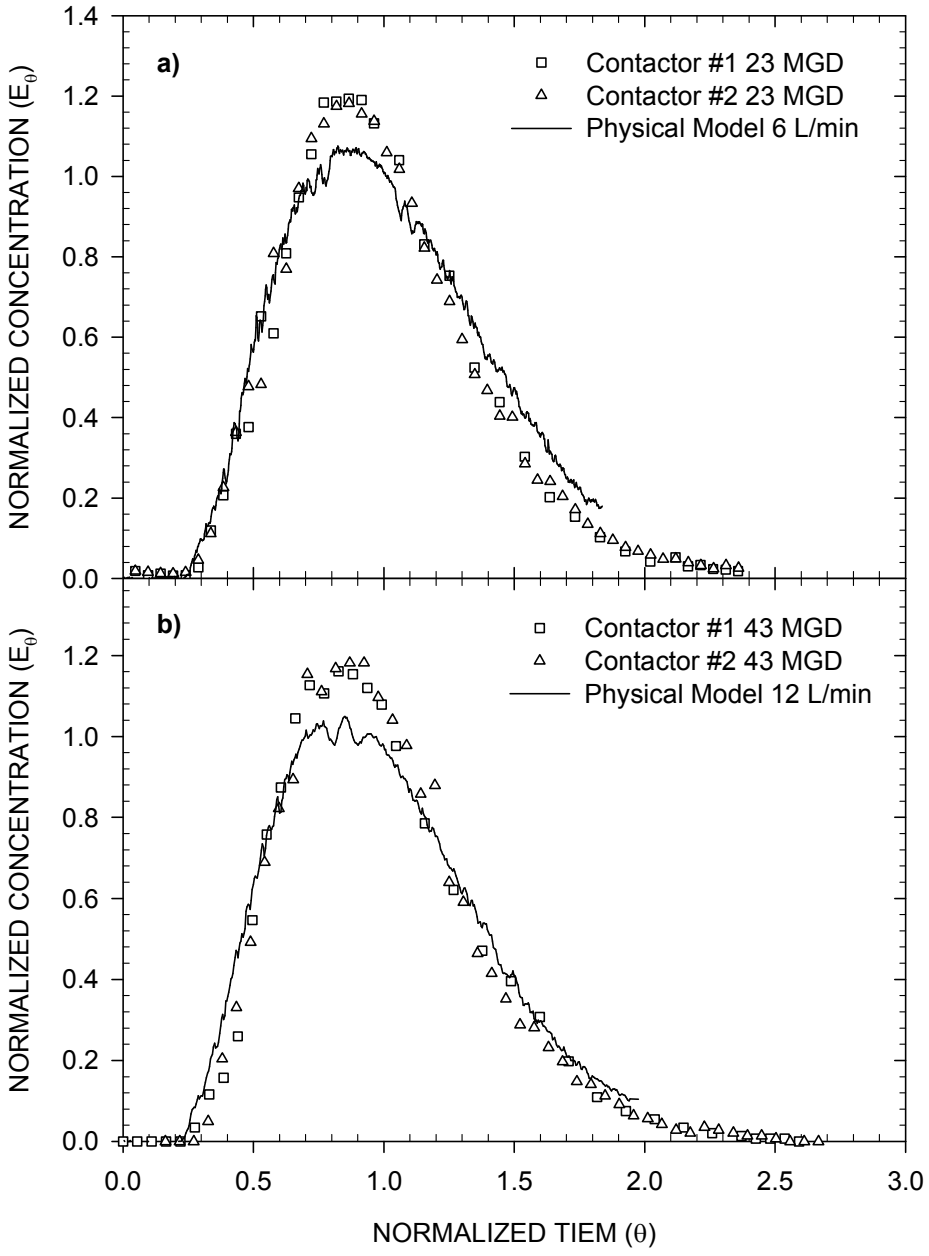

Figure 6.4. Comparing normalized RTD curves of the Linnwood plant with physical model reactor at each equivalent flow rate. 6 L/min for a); 12 L/min for b)

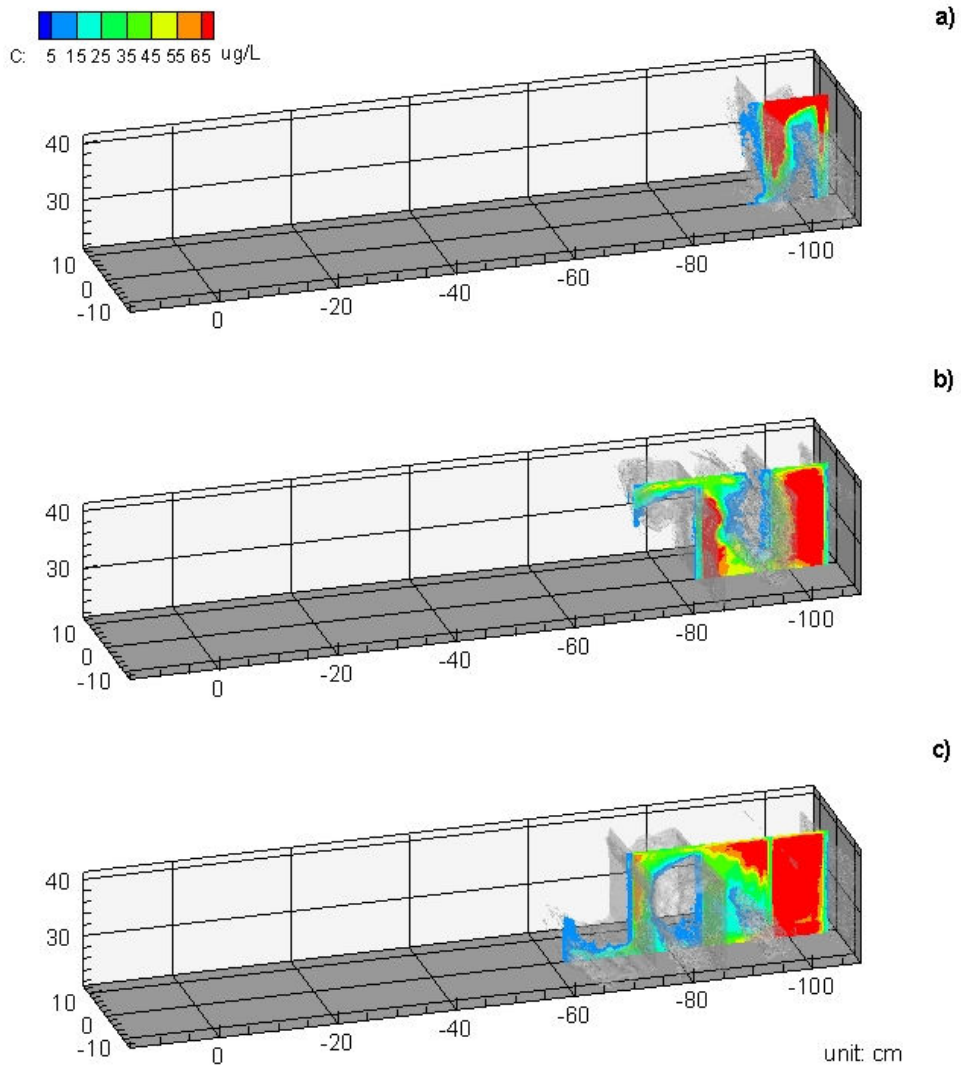

Figure 6.5. LIF images with contour slices at the center at 12 L/min: 30 seconds for a), 90 seconds for b), and 150 seconds for c)

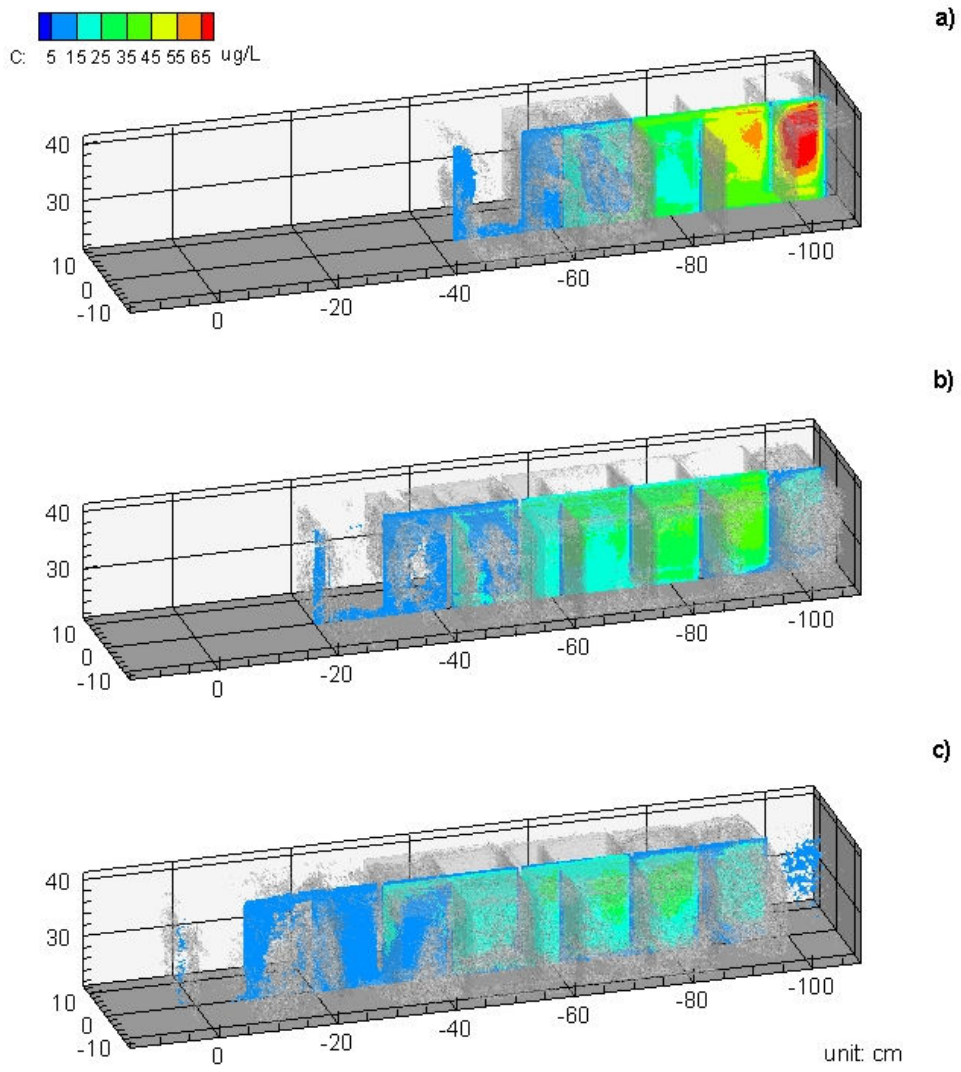

Figure 6.6. LIF images with contour slices at the center at 12 L/min: 300 seconds for a), 600 seconds for b), and 900 seconds for c)

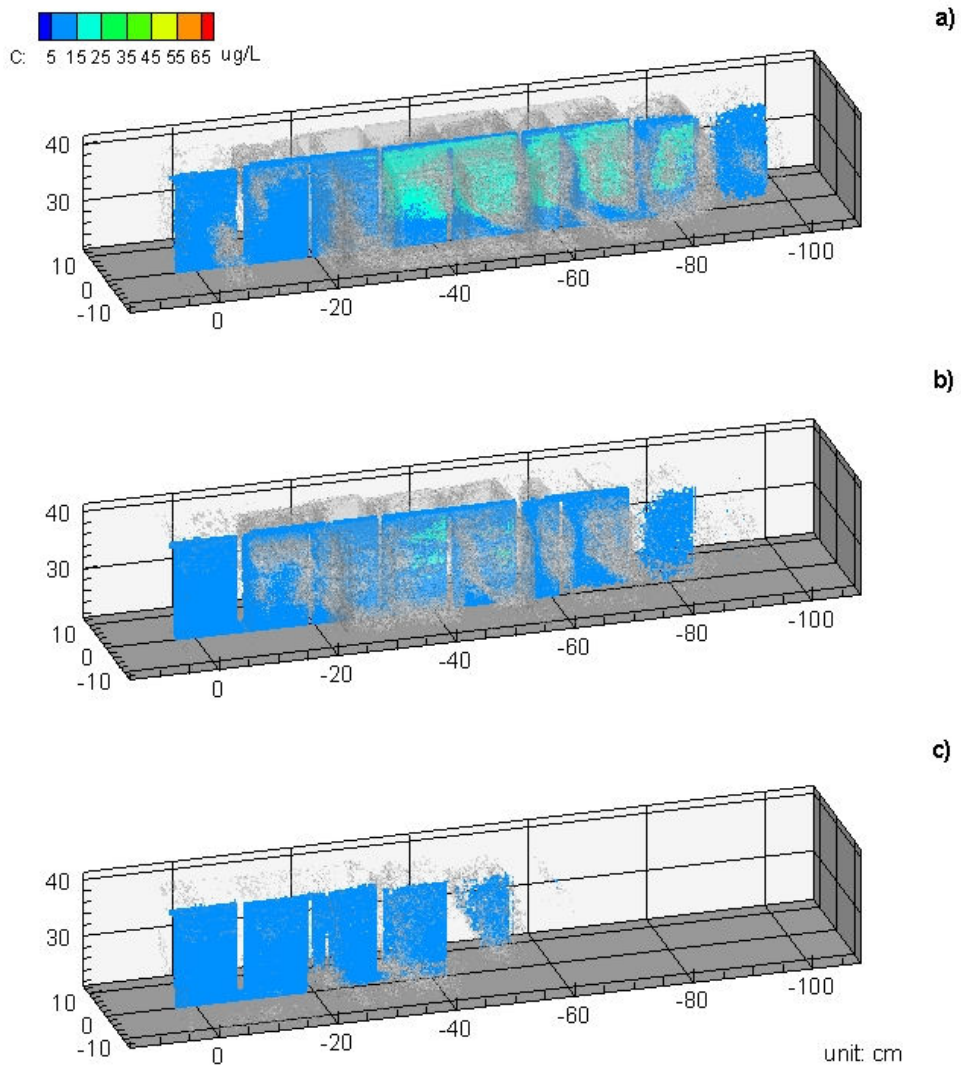

Figure 6.7. LIF images with contour slices at the center at 12 L/min: 1200 seconds for a), 1500 seconds for b), and 2100 seconds for c)

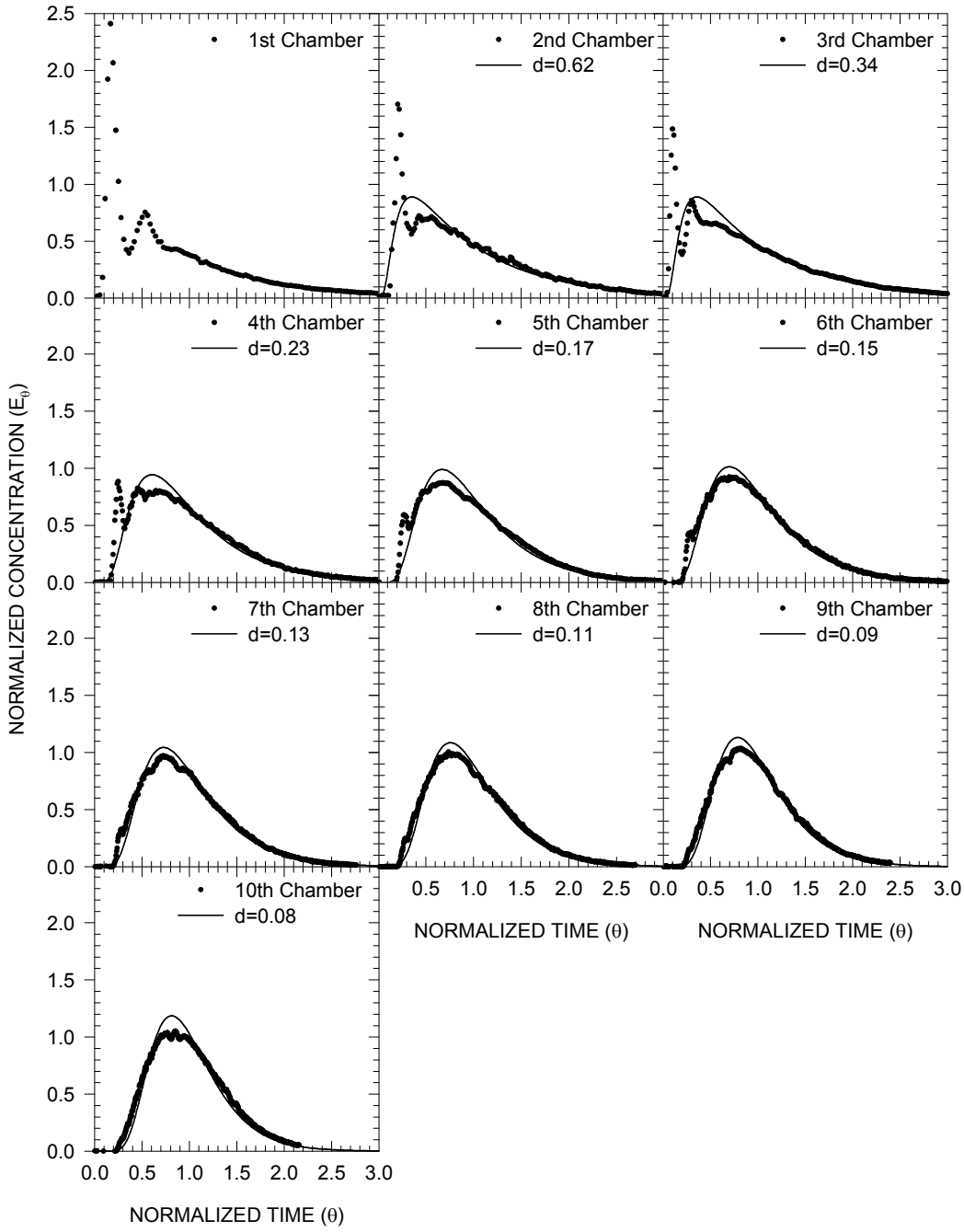

Figure 6.8. Normalized RTD curves and dispersion model at each chamber at 12 L/min.

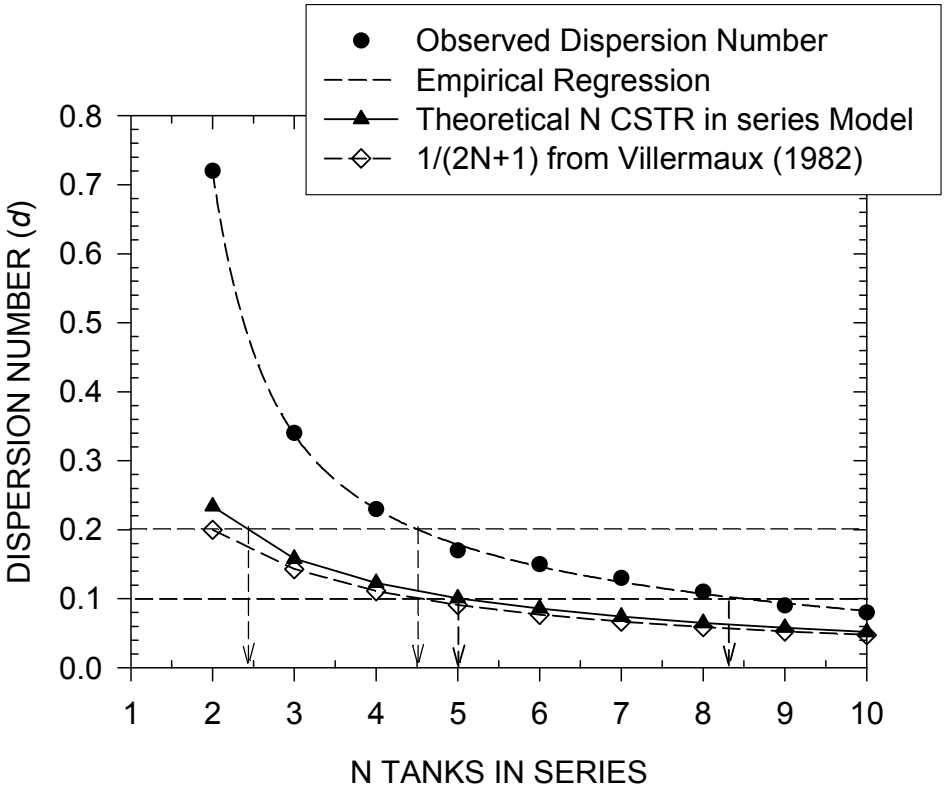

Figure 6.9. Comparing theoretical dispersion number for N CSTR in series and observed dispersion number of N tanks in series

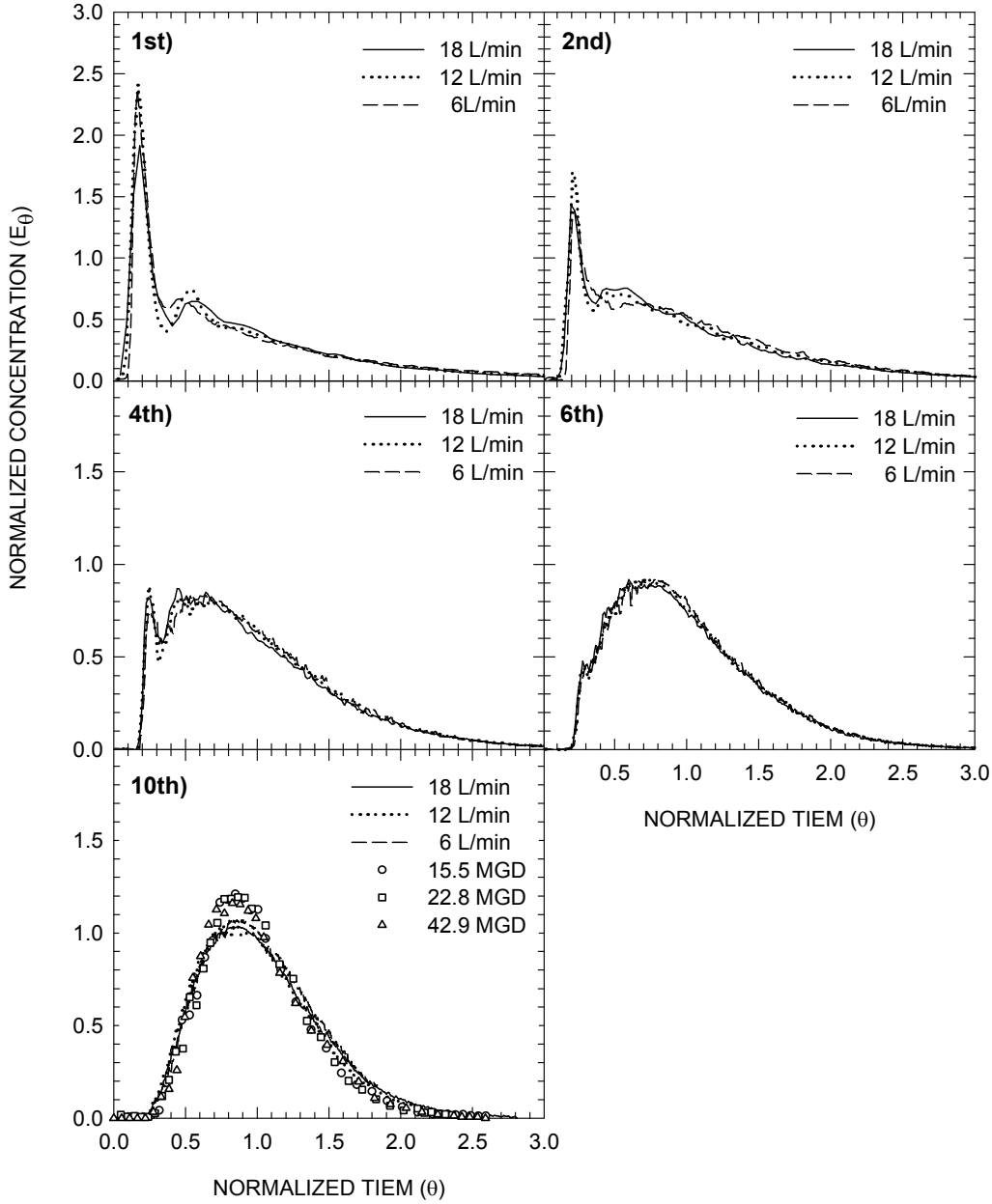

Figure 6.10. The normalized RTD from physical model reactor at three flow rates at each chamber. The normalized RTD from contactor #1 of the Linnwood ozone contactor is shown at the tenth chamber.

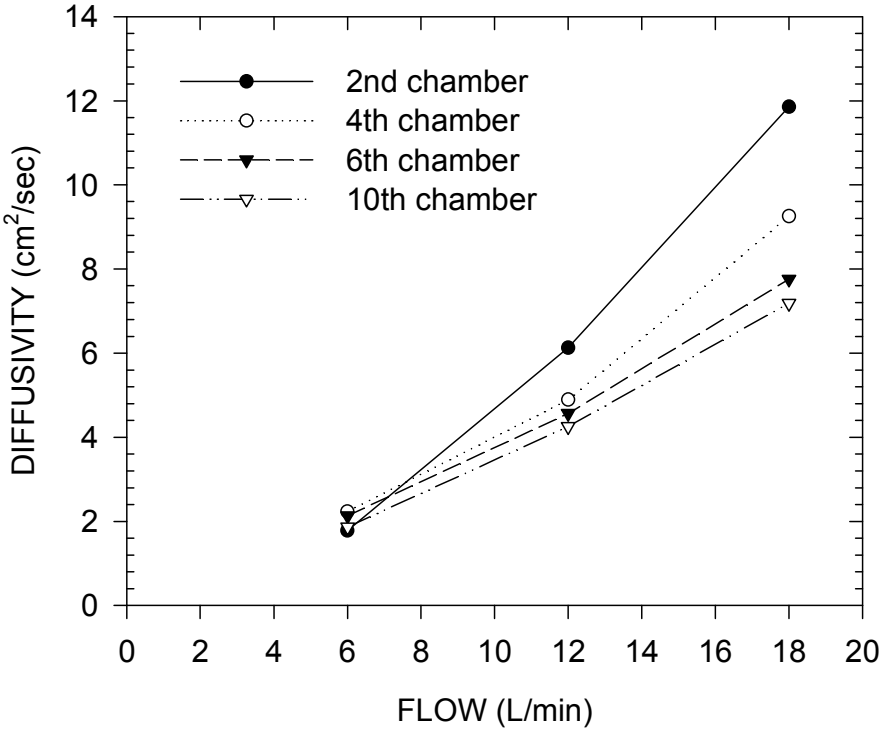

Figure 6.11. Observed diffusivity from observed dispersion number at the second, fourth, sixth, and tenth chamber with three different flow rate

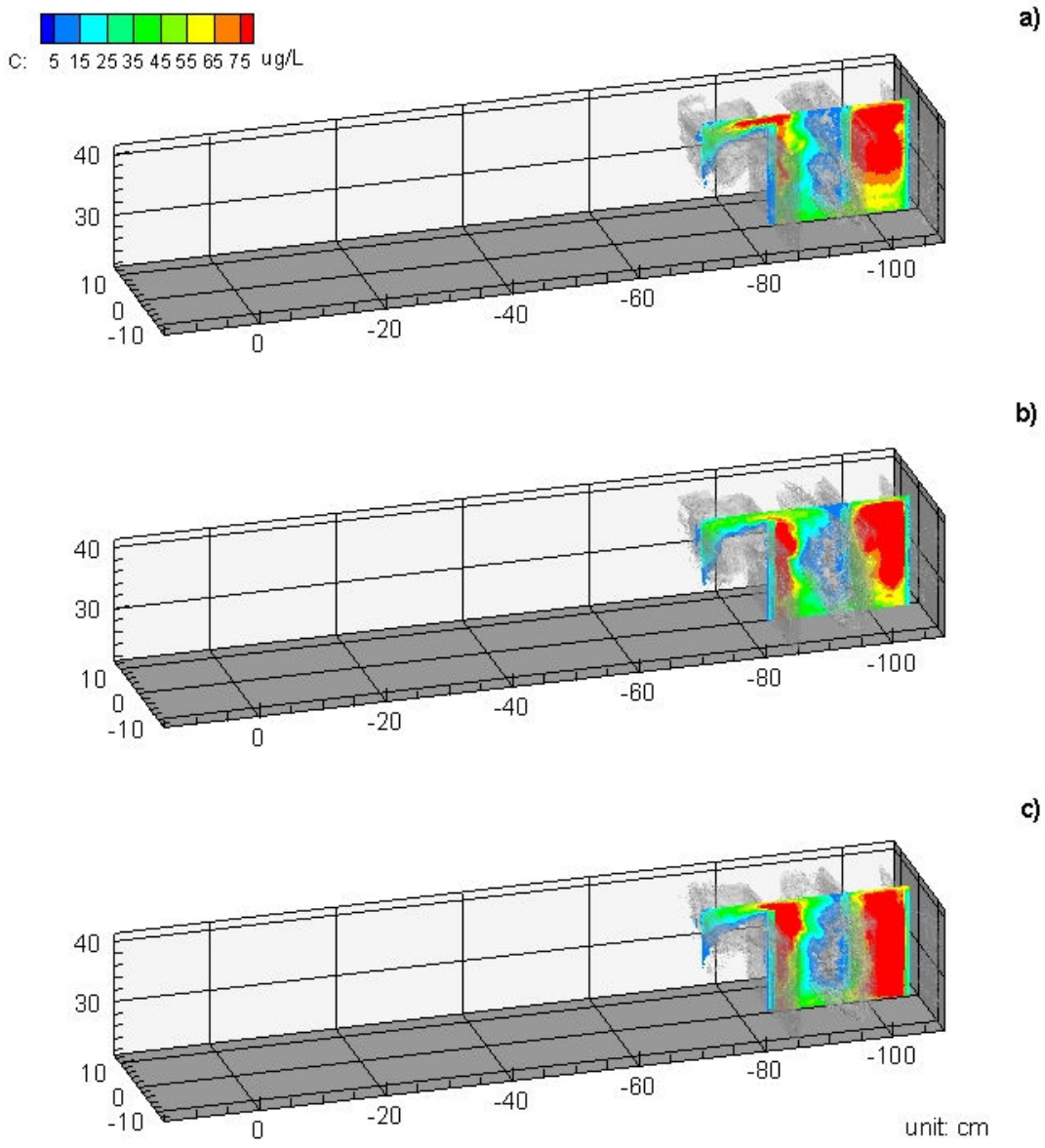

Figure 6.12. Laser dye mixing behavior with different flow rate at the outlet of the second chamber and time equivalent to T_5.

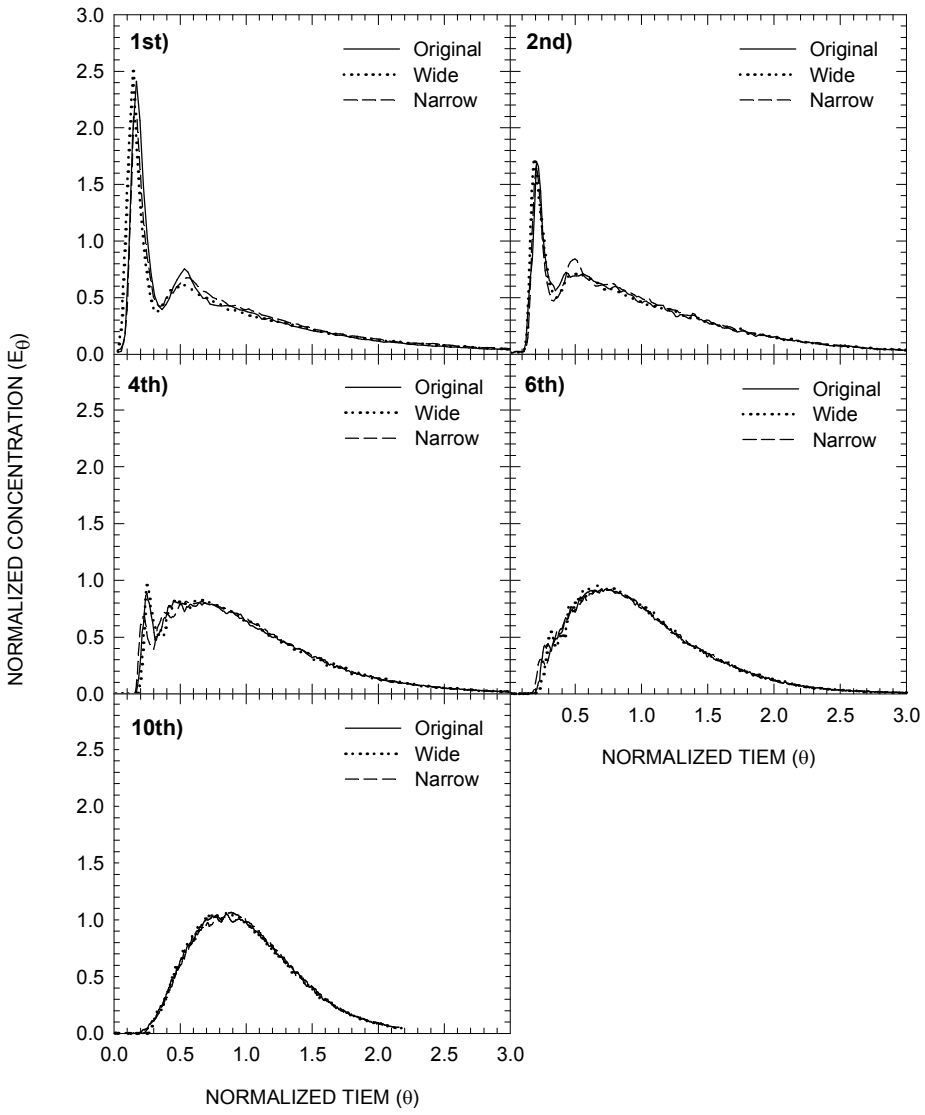

Figure 6.13. RTD from physical model reactor with three baffle opening. Normal opening is 1.2 inch and 0.45 inch for underflow and overflow baffles respectively. Wide is twice of normal opening and narrow is a half.

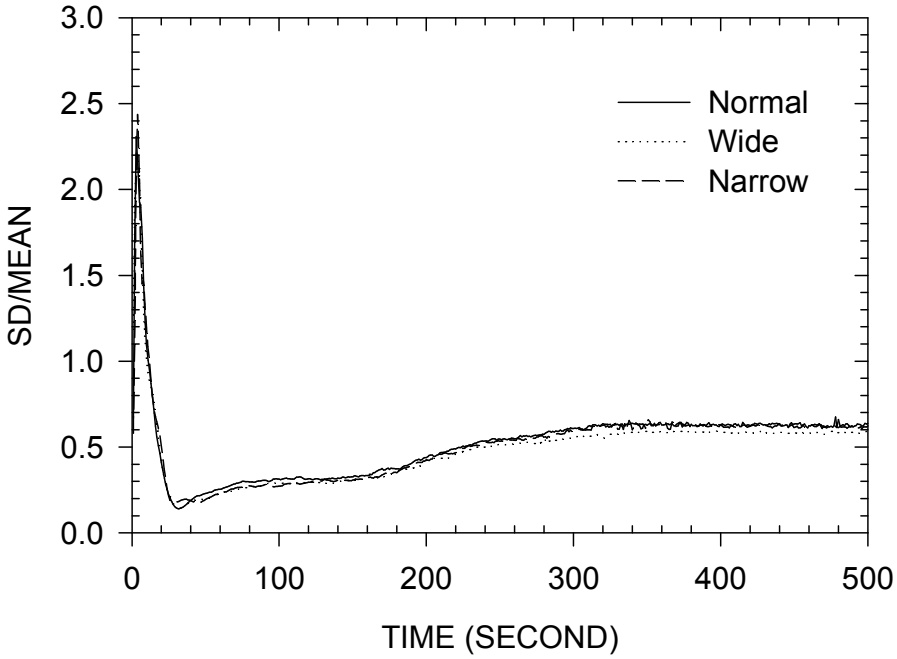

6.14. Mixing analysis using COV (standard deviation / mean) for the second chamber with normal, wide, and narrow baffles.

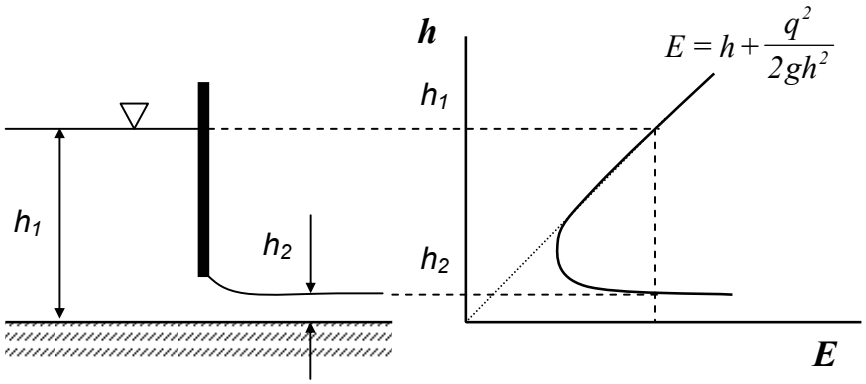

Figure 6.15. Specific energy diagram of open channel underflow weir (Munson et. al. 1990)

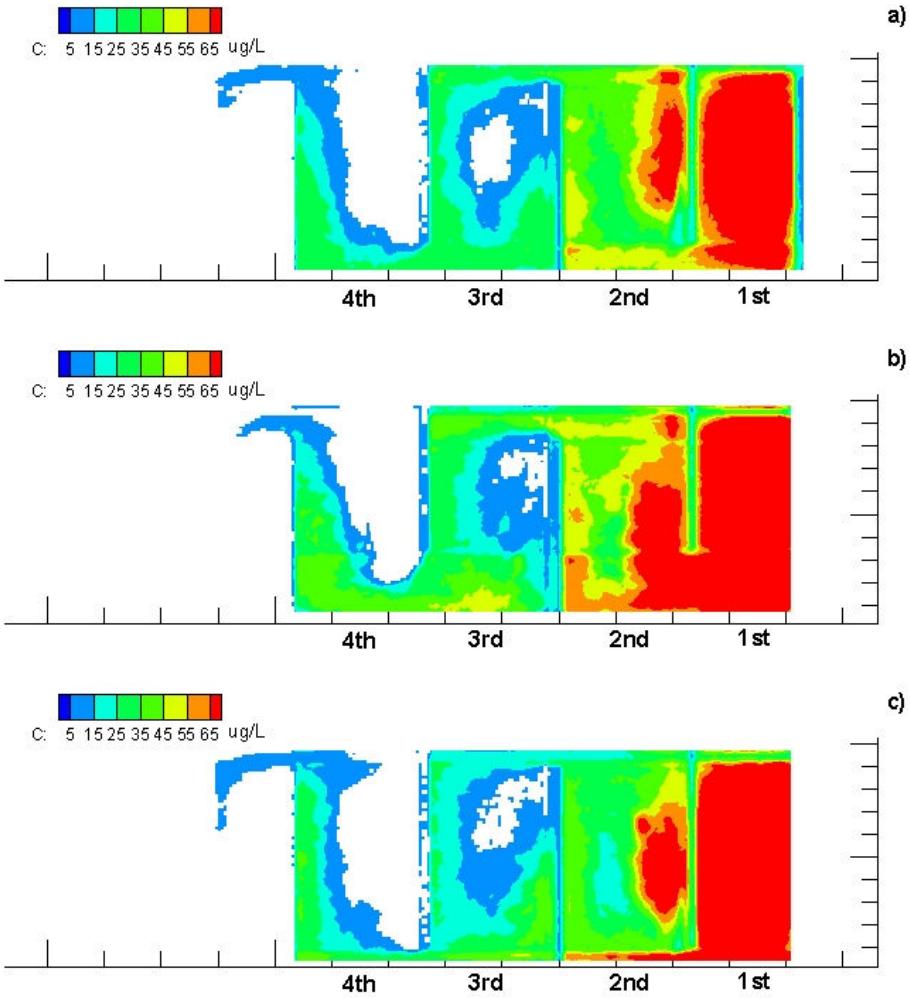

Figure 6.16. Dye mixing and transport after 180 seconds for normal baffle for a), wide baffle for b), and narrow baffle for c)

CHAPTER 7

APPLYING INTEGRATED OZONE CONTACTOR DESIGN TOOLS, MC-SFR, *OCM*, AND 3D-LIF, INTO A NEW OZONE CONTACTOR DESIGN

7.1. Introduction

A new ozone contactor with 150,000 m^3/day (40 MGD) capacity is in the planning stage in South Korea. The contactor will treat drinking water after conventional sand filtration and will be followed by biological activated carbon filters. The new ozone contactor consists of six consecutive chambers, among which the first and the second chambers are designed for enhanced mixing (close to a CSTR) with upward and downward flows, and the third to the sixth chambers as a plug flow reactor (PFR) with horizontal flow. Table 7.1 summarizes the dimension, the reactor type, and flow directions. Ozone is fed by a side-stream venturi injector (SVI) system and discharged into the first ozone chamber by an influent jet through a pipe with a diameter of 1.5 m. The volume of the new ozone contactor is 1,612 m^3 (0.43 MG) with a hydraulic detention time (HDT) of 15.5 minutes. The schematic diagram of the new ozone contactor is shown in Figure 7.1.

The design and operation of an ozone contactor are challenging tasks because the ozonation involves complex chemical and biological reactions, mass transfer processes, and non-ideal mixing conditions. The benefits of disinfection should be balanced with the risk of disinfection by-product formation and the consumption of financial resources, thus calling for an integrated design tool that helps designers determine optimal design parameters. The key elements for an optimal design are categorized by the Integrated Disinfection Design Framework (IDDF) (Bellamy, et al, 2000), which includes

disinfectant demand and decay, inactivation kinetics, disinfection by-product formation, and hydraulic characteristics. These four elements are essential for general disinfection design and operation.

The automatic and continuous analysis of disinfectant demand and decay are obtained using the MC-SFR system, described in Chapter 3 (Kim, et al, 2006a;Kim, et al, 2006c). Kinetic data are used for the following *OCM* software simulations. The *OCM* software could provide predictions for residual ozone concentration, *C. parvum* oocyst inactivation, and bromate formation with various design options to a designer during the planning stage. The *OCM* software can predict residual ozone concentration, log *C. parvum* inactivation, and bromate formation according to various operational scenarios, which could optimize design parameters such as initial ozone concentration, ozone dosage, pH, and residence time according environmental conditions such as water temperature.

The hydrodynamics of an ozone contactor are shown to be very critical for disinfection efficiency and disinfection by-product control (Kim, et al, 2006b). Chapter 5 and 6 introduced a three-dimensional laser-Induced fluorescence (3D-LIF) technique that has proven to be extremely useful for visualizing and quantitatively analyzing mixing behaviors in various types of reactor systems by imaging the instantaneous tracer concentration field over a three dimensional sampling space. 3D-LIF technology is used to analyze the hydrodynamics of the new ozone contactor.

The purpose of this chapter is to demonstrate an integrated design tool, including *OCM* software, MC-SFR, and 3D-LIF for new ozone contactor design optimization.

7.2. Experimental Methods

7.2.1. Ozone Decay and Bromate Formation Kinetics Using MC-SFR

The MC-SFR system is used to obtain kinetic data from raw water for the OCM software simulation. Details of the MC-SFR system are described in Chapter 3 (Kim, et al, 2006a). Raw water is sampled from an existing plant that shares the same source water with a new plant after sand filtration. The raw water is purged with analytical grade nitrogen gas to remove the carbonate species and then recarbonated with a 100 mM sodium bicarbonate stock solution to 0.02 mM total carbonate, which is close to a saturated carbonate dosage at pH 6.3 (Snoeyink & Jenkins, 1980). This pH is obtained from the raw water after sand filtration, which follows coagulation using alum as a coagulant.

Experiments are carried out according to the experimental matrix shown in Table 7.2 with an initial ozone concentration of 0.98 mg O_3/L. The representative temperatures for winter, spring/fall, and summer are 5, 15, and 25^{o}C, respectively, in South Korea, and pH 6, 7, and 8 are within the ordinary operational conditions of an ozone contactor in a drinking water treatment plant. Bromate formation kinetics are obtained by the same experimental method described in Chapter 4 (Kim, et al, 2006b).

7.2.2. Physical Model Reactor

The physical model reactor is scaled down based on the Froude number similarity using Equation (7.1), as described in Chapter 5.

$$\frac{t \times U}{H} = \varphi(Fr, \frac{W}{H}, \frac{D}{H}) \tag{7.1}$$

$$Fr = \frac{U}{\sqrt{gH}} \tag{7.2}$$

where t is time (T), U is axial velocity (LT^{-1}), H, W, and D are height (L), width (L), and depth (L), respectively, of the ozone contactor, g is gravitational acceleration (LT^{-2}), and Fr is the dimensionless Froude number. An acrylic model ozone contactor is built on a 70:1 scale from a proto-plant.

7.2.3. Conservative Tracer Test Using 3D-LIF

A conservative tracer test using 3D-LIF system is carried out as described in Chapter 5. Pulse injection volume of 100 mg/L stock Rhodamine 6G solution is 0.5 mL. The video capturing rate starts at 100 frames per second for 180 seconds, creating about 5.0 GB of raw video stream files. The raw data were calibrated and corrected by a procedure established by Tian and Roberts (2003).

7.3. Results and Discussion

7.3.1. Raw Water Quality Analysis

Table 7.3 summarizes raw water quality for the new ozone contactor. Raw water sampled after sand filtration showed very low TOC, UV_{254}, and bromide concentration. It is noteworthy that bromide concentration is considerably lower than 27 to 65 μg/L which is reported as the average bromide concentration from source water in the United States (USEPA, 2003). For this particular process design, formation of bromate should be of less significance compared to disinfection efficiency.

7.3.2. Ozone Decay and Bromate Formation Kinetics Using MC-SFR

An empirical equation for ozone decay is expressed by Equations (7.3) and (7.4) (Lev & Regli, 1992).

$$\frac{d[O_3]_l}{dt} = -k_D[O_3]_l - k_R[D]\cdot[O_3]_l \tag{7.3}$$

$$\frac{d[D]}{dt} = -k_R[D]\cdot[O_3]_l \qquad (7.4)$$

where $[O_3]_l$ is ozone residual in the liquid phase (ML^{-3}), $[D]$ is ozone demand (ML^{-3}), k_D is the first order rate constant for ozone decay (T^{-1}), and k_R is the second order rate constant for the ozone demand decrease ($L^3M^{-1}T^{-1}$).

Ozone decay rate (k_D), ozone demand (D_0), and ozone demand reaction rate (k_R) of the experimental conditions are shown in Table 7.4. Ozone decay rate (k_D) ranged from 0.0004 to 0.0070 $s^{-1,}$ depending on the temperature and the pH. A faster ozone decay in a higher pH is associated with an abundance of OH^-, which promotes faster ozone decay (Gurol & Singer, 1982;Tomiyasu, et al, 1985). Higher temperature accelerates ozone decay by Arrhenius expressions (Equation (2.4) and (2.5)). Fast ozone demand (D_0) and ozone demand decay rate constant (k_R) also increase as the temperature and the pH increase since ozone demand is partly incorporated with a hydroxyl radical chain reaction, and higher pH and temperature are preferred conditions (Elovitz & von Gunten, 1999;Park, et al, 2001). The ozone decay model, expressed by Equation (7.3) and (7.4), matched well with the experimental data, as shown in Figure 7.2. Bromate formation kinetics could be expressed by the first-order kinetic Equation (7.5). A considerable amount of bromate is formed instantaneously, called "fast bromate formation", which is caused by relatively abundant hydroxyl radical at the initial phase of the ozone degradation. After the initial phase, bromate increases gradually according to the *CT* increase. Table 7.5 shows "fast bromate formation" and the bromate formation rate over *CT*.

$$\frac{d[BrO_3^-]}{dt} = k_{BrO_3^-}[O_3]_l \qquad (7.5)$$

7.3.3. OCM Software for a New Ozone Contactor Design

OCM Software simulation

The ozone decay rate, ozone demand, the ozone demand reaction rate, and the bromate formation rate were obtained for each pH and temperature using MC-SFR. Additionally, the *C. parvum* oocyst inactivation rate (k_N) and the dispersion number (d) were obtained for *OCM* software simulation. Equation (7.6) was used to obtain k_N for each temperature regardless of the pH because the effect of pH on k_N would be negligible (Kim, et al, 2004).

$$k_N = 0.0917 \times 1.097^T . \tag{7.6}$$

The dispersion number, 0.048, was obtained from the conservative tracer test using a conductivity meter after a pulse injection of sodium chloride into the inlet of the third chamber. Dispersion number (d) was calculated by solving Equation (7.7) for large dispersion (d > 0.01) and a closed reactor after substituting variance (σ_θ^2), which was obtained from Equation (7.8) (Levenspiel, 1999).

$$\sigma_\theta^2 = 2d - 2d^2 \times (1 - e^{-\frac{1}{d}}) \tag{7.7}$$

$$\sigma_\theta^2 = \frac{\int (t-\tau)^2 C dt}{\int C dt} = \frac{\int t^2 C dt}{\int C dt} - \tau^2 \tag{7.8}$$

where C is conductivity (uS/cm) and τ is mean residence time (T). As dispersion number, 0.048, was taken from the third to the sixth chamber, equivalent dispersion numbers for each chamber is taken by multiplying the axial distance ratio (f) to 0.048 as shown at Equation (7.9).

$$f = \frac{L_{3rd} + L_{4th} + L_{5th} + L_{6th}}{L_{Nth}} \tag{7.9}$$

where L_{Nth} is a axial length of *Nth* chamber, $N = 3, \ldots, 6$.

CT, residual ozone concentration, log *C. parvum* oocyst inactivation, and bromate formation were predicted using *OCM* software with the original design conditions at three pH values and three temperatures. Although *OCM* software was designed for an ozone contactor with a fine bubble diffuser (FDB), it can easily be modified for an ozone contactor with a side-SVI system by means of using the initial ozone concentration and assigning zero for gas phase ozone concentration in the "ozone contactor dialog box" of *OCM* software. Figure 7.3 shows simulation results with an initial ozone concentration of 1 and 2 mg/L. From this figure, it was shown that high residual ozone concentration at the effluent could be problematic at low pH and low temperature, which would require additional equipment to quench residual ozone to prevent residual ozone from affecting the biological filters, which might add capital and operational costs. Increasing pH to 7 or 8 could decrease residual ozone concentration, but it would also decrease *C. parvum* oocyst inactivation because of lowered *CT*. Fortunately, additional bromate formation exerted by increasing the pH was not critical since overall bromate formation was far lower than 10 μg/L, which is the maximum contaminant level regulated by the US EPA (US EPA, 1994). *C. parvum* oocyst log inactivation efficiency was lower than 2.0 for all pH values and temperatures except for pH 6.0 at 25°C. Note that 2 log inactivation is the current regulation for *C. parvum* oocyst for drinking water treatment in the US (US EPA, 2006). If 2 log inactivation is targeted by only ozonation, additional ozone dosage might be required. The required initial ozone concentrations for the three pH values and three temperatures are shown in Figure 7.4. Ozone generator capacity is recommended to meet this initial ozone concentration.

Effect of Dispersion on Disinfection

Dispersion in an ozone contactor affects ozone consumption, log inactivation efficiency, and disinfection by-product formation (Roustan, et al, 1996;Do-Quang, et al, 2000a;Kim, et al, 2004;Kim, et al, 2006b). Lower dispersion number is known to increase inactivation efficiency (Do-Quang, et al, 2000b;Kim, et al, 2004) and to reduce bromate formation (Roustan, et al, 1996;Kim, et al, 2007). The *OCM* software was used to reveal the effect of the dispersion number, ranging from 0.01 to 4.8 using ozone decay kinetic constant from the raw water in the design conditions. The effect of the dispersion number on *C. parvum* oocyst inactivation is compared in Figure 7.5. Log inactivation was affected more sensitively on dispersion number when the dispersion number was relatively small and the target inactivation rate was high (e.g., pH 6.0 and 7.0 at 25^{o}C). The dispersion number 0.01 at pH 6.0 and 25^{o}C showed 33% higher log inactivation than dispersion number 4.8 in the same conditions. From this figure, it was interesting to note that efforts to reduce dispersion to less than about 0.2 would be much more advantageous than those for reducing it from 5 to 0.5. Therefore it is important to maintain dispersion number less than 0.2 for benefits of low dispersion for log inactivation. In addition, inactivation of *Giardia lambria* and virus might be more sensitive to the dispersion number because it has much higher inactivation efficiency than *C. parvum* oocyst in the same *CT* conditions (Rakness, et al, 2005).

7.3.4. Hydrodynamic Analysis Using 3D-LIF System

Figure 7.6 shows the dye mixing and transport behavior over time in a new ozone contactor. The first and second contactor is aimed for ozone contacting chambers and originally designed as two CSTRs in series. These chambers are characterized by upward and downward flow and a small chamber volume. The vertical flow is often incorporated with non-ideal flow like short-circuiting and back-flow as discussed in Chapter 6. Short-

circuiting is clearly observed from the second ozone chamber shown at Figure 7.6 (40 and 80 seconds). Although flow in this chamber is assumed as CSTR, mixing of the first and the second ozone chambers might be different from ideal CSTR. The mixing characteristics are analyzed with the COV (coefficient of variance) using Equation (7.10). The variation in the COV over time in the first and the second ozone chambers at 150,000 m^3/day flow rates is shown in Figure 7.7. The COV at the hydraulic detention time (HDT) of the first and the second chamber is 9% and 21%, respectively, which shows that mixing in the second chamber is not sufficient because COV at the second chamber is much larger than 10 % which is considered as good mixing (Rossman & Grayman, 1999).

$$COV = \frac{\text{Standard Deviation of Tracer Concentrations}}{\text{Mean Tracer Concentration}} = \frac{\sqrt{\frac{1}{n-1}\times\sum_{i,j,k}\left(C(x_i,y_j,z_k,t)-\frac{1}{n}\times\sum_{i,j,k}C(x_i,y_j,z_k,t)\right)^2}}{\frac{1}{n}\times\sum_{i,j,k}C(x_i,y_j,z_k,t)} \tag{7.10}$$

where *C(x, y, z, t)* is the dye concentration, *n* is the number of pixels in the zone.

Figure 7.8 shows normalized residence time distribution (RTD) curves obtained using 3D-LIF in the first to the sixth ozone chambers. This RTD curves obtained at the end of each chamber were compared with the CSTR in series model and the axial dispersion model. The CSTR model in the first chamber deviated considerably from the experimental RTD curve and the second chamber also deviated from the two CSTR in series model. The difference might be the result of non-ideal flow caused from short-circuiting and back-flow. The ADR model gradually matched better the RTD curve as the number of the chambers increases from the third chamber. The dispersion number of the third chamber is 0.113 and reached 0.030 at the sixth chamber.

One of the features of this ozone contactor configuration is two CSTRs followed by four PFRs. A question arises if this current hybrid configuration is hydro-dynamically beneficial to disinfection. The hydrodynamics of this system was analyzed with dispersion number because dispersion is critical design parameter for disinfection. The dispersion numbers were obtained at the three points of each PFRs, each of which is evenly spaced in axial distance of each chambers. Dispersion number showed tendency to decrease with axial distance as shown in Figure 7.7-a). Diffusivity (D), shown at Figure 7.7-b), was obtained by multiplying axial distance (L) and axial velocity (U) to dispersion number (d) using Equation (7.11).

$$d = \frac{D}{UL} \tag{7.11}$$

Diffusivity linearly decreased with axial distance (Figure 7.9-(b)). Diffusivity near the reactor inlet was higher because diffusivity was calculated based on accumulated reactor volume and initial CSTR like flow had very high diffusivity. If the first and the second chambers were designed as PFR, dispersion numbers would decrease as a result. For example, assuming that diffusivity is 0.16 m^2/sec throughout the whole contactor, which is the average of final two diffusivities in Figure 7.9-b), dispersion numbers would be lower than that of original design. Therefore, it is highly recommended to switch initial two CSTR into PFR-like chambers by removing intervening two baffles.

7.4. Conclusion

Newly developed integrated ozone disinfection system design tool which consists of MC-SFR, *OCM* software, and 3D-LIF system were applied to design a new ozone contactor under planning stage. From *OCM* simulation results with kinetic data from MC-SFR, excessive residual ozone concentration and low disinfection efficiency at low

temperature are expected for this particular reactor, which would need ozone quenching facility and additional ozone dosage respectively. Lower dispersion number less than about 0.2 was found to be critical for disinfection efficacy. Hydrodynamics study on original design using 3D-LIF system showed relatively poor mixing (*i.e.* short circuiting) in two CSTRs located at the inlet and consequently the overall dispersion number would increase. While this study remains as a pure simulation result using the software and lab-scale model reactor, it demonstrates how the newly developed tool might be used for design of ozone contactors in real world application. As our previous study has verified that the simulation results matched well with full-scale observations, this demonstration further provides valuable, practical information to the engineers for current design modification. For example, it was suggested that the first two chambers might need to be modified by removing the baffle so that more plug-flow like condition can be achieved.

Table 7.1 Proto-reactor dimension and type of six serial chambers of a new ozone contactor

Cell Order	Reactor Type	Width (m)	Depth (m)	Height (m)	Volume (m^3)	Volume (MG)	Flow Direction
1	CSTR	3.45	3.85	6.19	82.2	0.02172	upward
2	CSTR	3.45	3.85	6.19	82.2	0.02172	downward
3	PFR	18.5	3.65	6.19	418.0	0.11042	$\rightarrow$
4	PFR	14.65	3.85	6.19	349.1	0.09223	$\leftarrow$
5	PFR	14.65	3.85	6.19	349.1	0.09223	$\rightarrow$
6	PFR	14.65	3.65	6.19	331.0	0.08744	$\leftarrow$

Table 7.2 Experimental matrix for ozone decay kinetics

	pH 6.0	pH 7.0	pH 8.0
5 ^{o}C	✓	✓	✓
15 ^{o}C	✓	✓	✓
25 ^{o}C	✓	✓	✓

Table 7.3 Raw water qualities

pH	TOC (mg/L)	UV_{254} (1/cm)	SUVA (L/mg·cm)	Br (μg/L)
6.3	1.05	0.012	1.18×10^{-2}	6.9

Table 7.4 Ozone decay rate (k_D), fast ozone demand decay rate (D_0), and fast ozone demand (k_R)

	pH = 6.0			pH = 7.0			pH = 8.0		
	k_D (1/s)	D_0 (mg/L)	k_R (L/mg/s)	k_D (1/s)	D_0 (mg/L)	k_R (L/mg/s)	k_D (1/s)	D_0 (mg/L)	k_R (L/mg/s)
5 °C	0.0004	0.20	0.043	0.0006	0.27	0.046	0.0009	0.33	0.049
15 °C	0.0006	0.27	0.046	0.0007	0.31	0.052	0.0013	0.34	0.050
25 °C	0.0010	0.35	0.047	0.0015	0.38	0.056	0.0070	0.52	0.165

Table 7.5 Bromate formation rate (k_{BrO3}-, μgBrO_3^-/mgO_3/min) and "fast bromate formation" ($BrO_{3,0}^-$, mg/L)

	pH = 6.0		pH = 7.0		pH = 8.0	
	k_{BrO3}-	$BrO_{3,0}^-$	k_{BrO3}-	$BrO_{3,0}^-$	k_{BrO3}-	$BrO_{3,0}^-$
5 °C	0	1.94	0.066	1.58	0.08	1.76
15 °C	0.008	1.68	0.099	1.42	0.111	1.73
25 °C	0.025	1.65	0.1	1.38	0.11	1.87

Table 7.6 Dispersion Number at Design Flow Rate (150,000 m^3/day)

Chamber	1st	2nd	3rd	4th	5th	6^{th}
Flow Characteristics	CSTR	CSTR	PFR	PFR	PFR	PFR
Dispersion Number	10,000	10,000	0.113	0.065	0.040	0.033

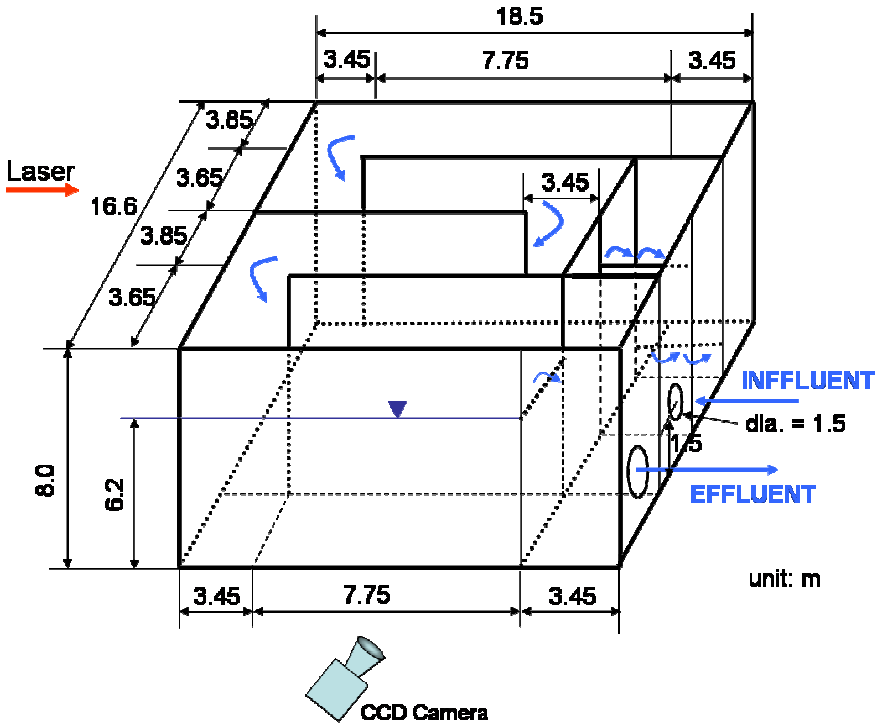

Figure 7.1. Proto-design of a new ozone contactor under planning stage

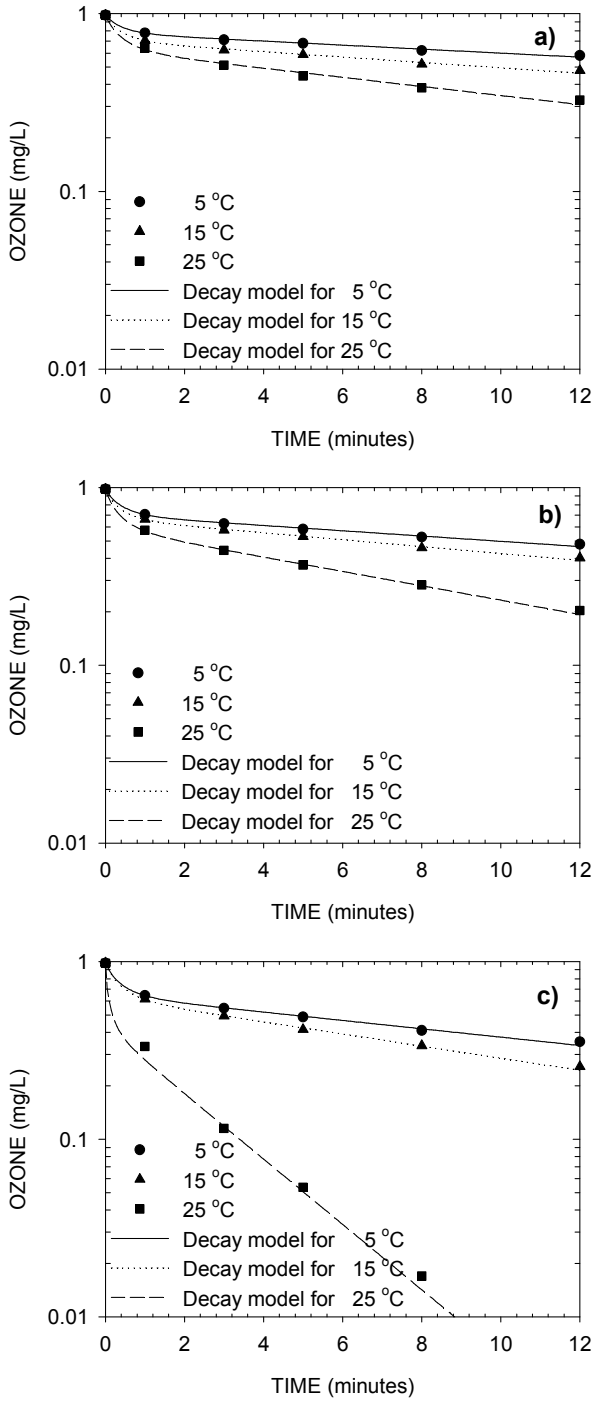

Figure 7.2. Ozone decay kinetics obtained from three different pH values and three different temperatures using the MC-SFR system

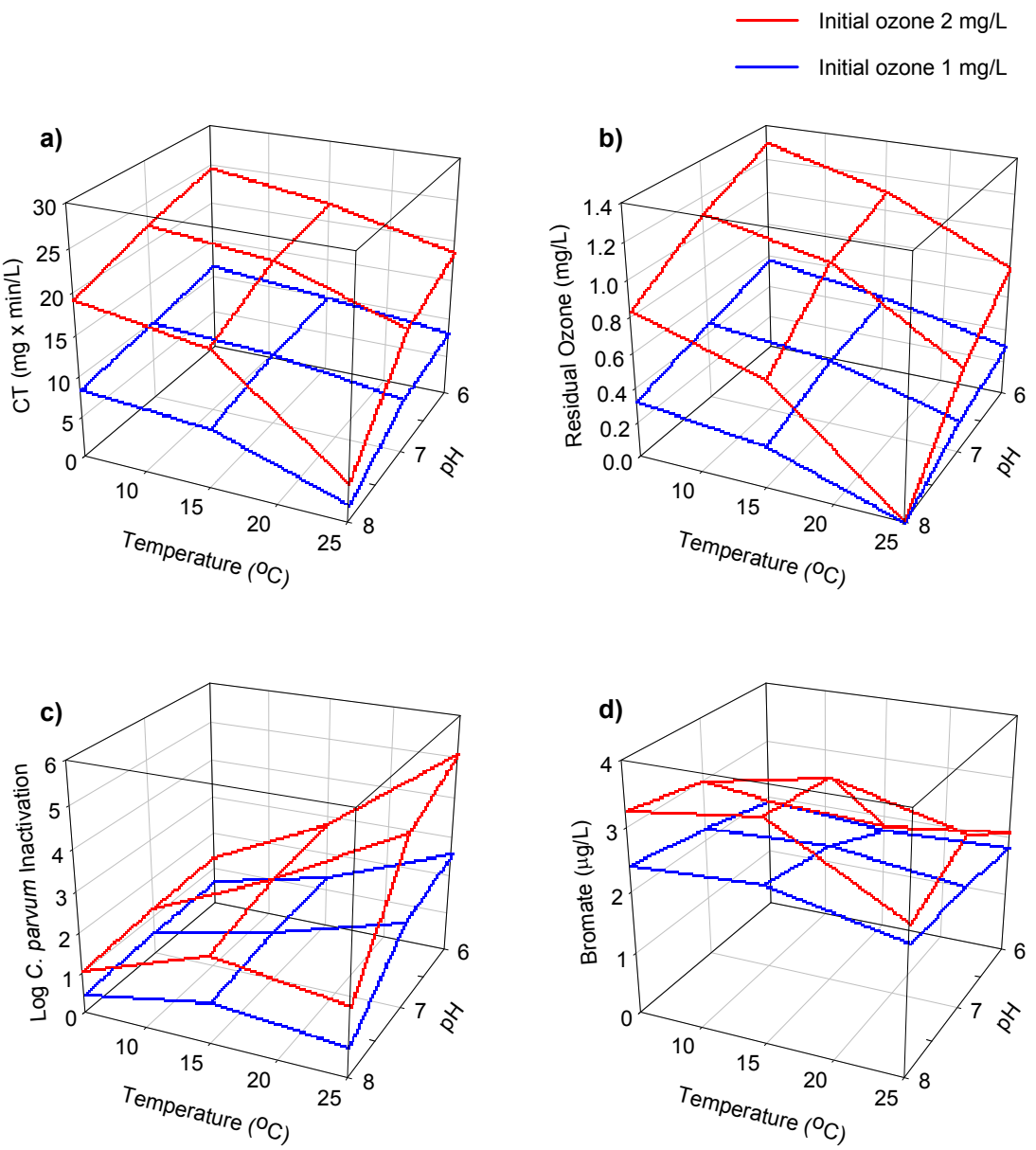

Figure 7.3. *CT* for a), residual ozone for b), log *C. parvum* inactivation for c), and bromate formation for d) at two initial ozone concentrations (1 and 2 mg/L).

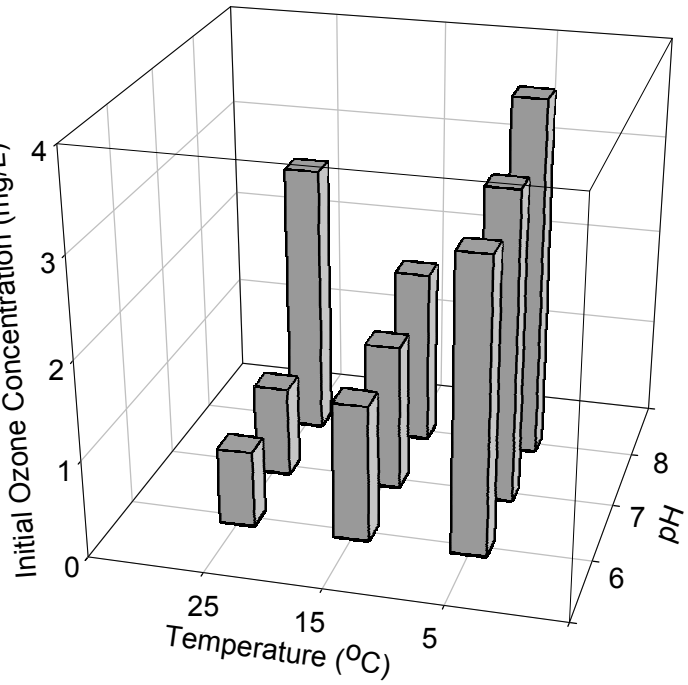

Figure 7.4. Initial ozone concentration required to meet 2 Log *C. parvum* oocyst inactivation

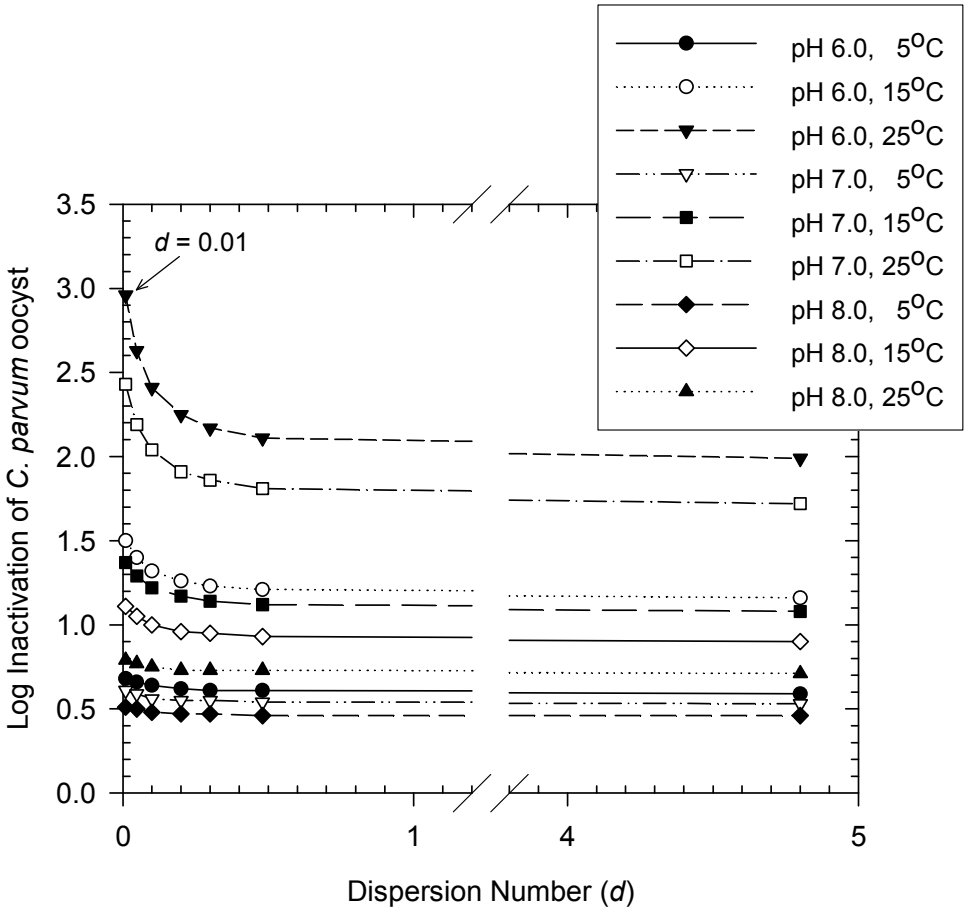

Figure 7.5. Effect of the dispersion number (*d*) on the log inactivation of the *C. parvum* oocyst with 1 mg/L initial ozone concentration

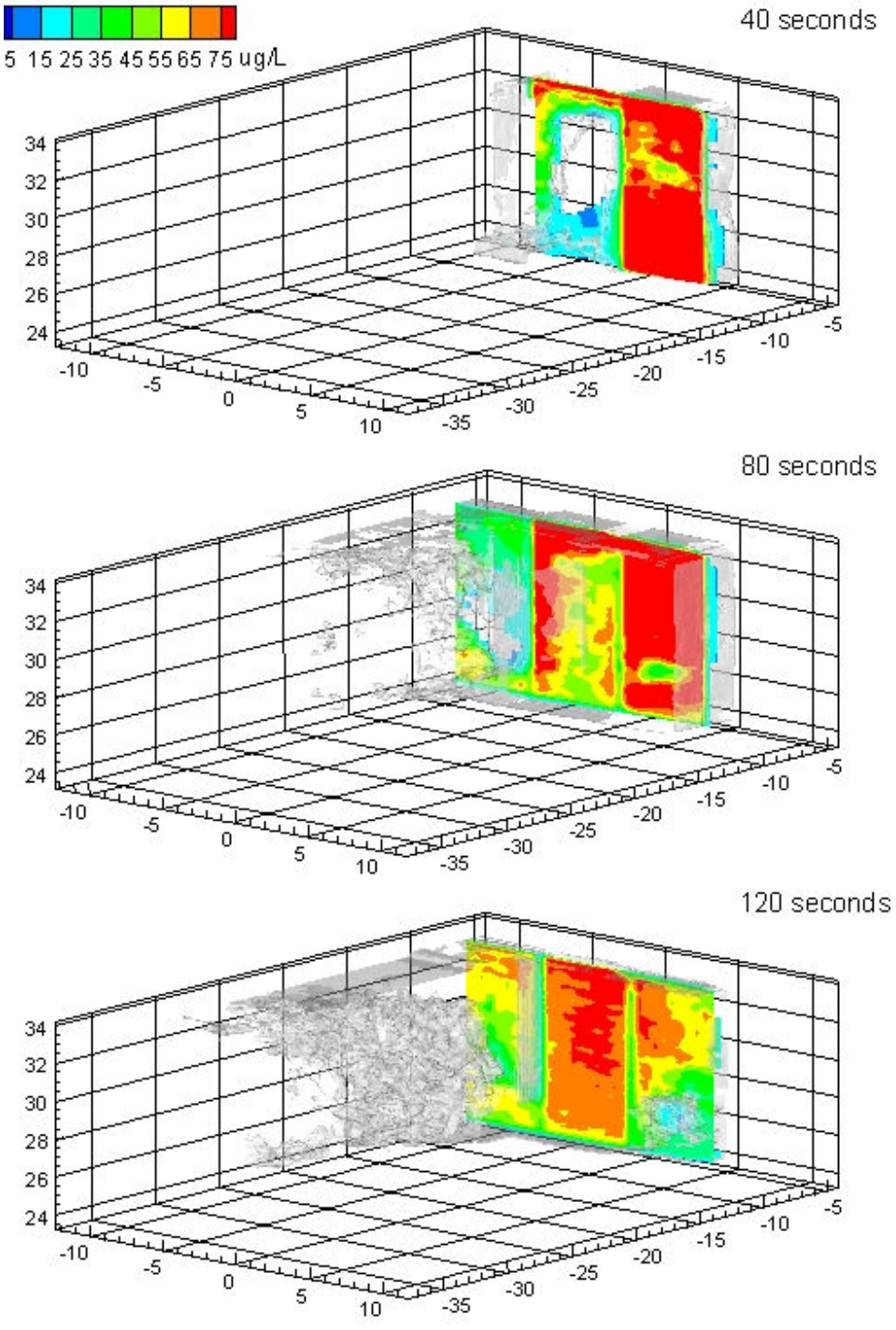

Figure 7.6. Cross sectional view of laser dye transport and mixing in the first and second ozone chambers.

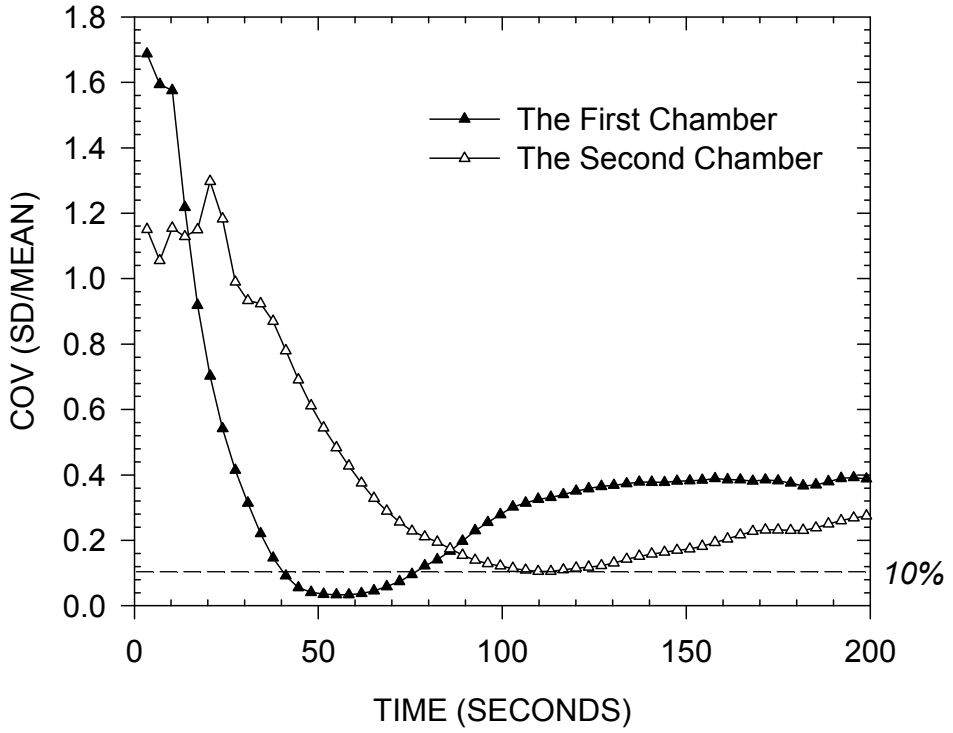

Figure 7.7. COV (Standard Deviation / Mean) of the first and second ozone chambers at flow, 150,000 m^3/day.

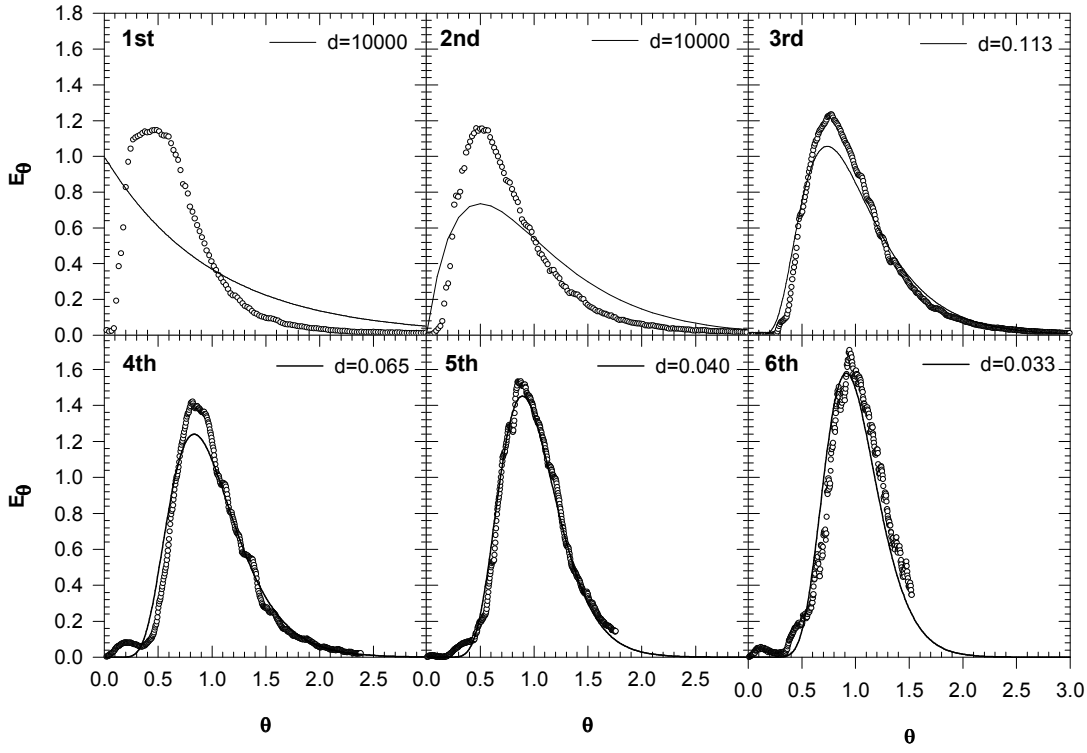

Figure 7.8. Residence time distribution (RTD) curves at each ozone chamber with a design flow rate of 150,000 m^3/day

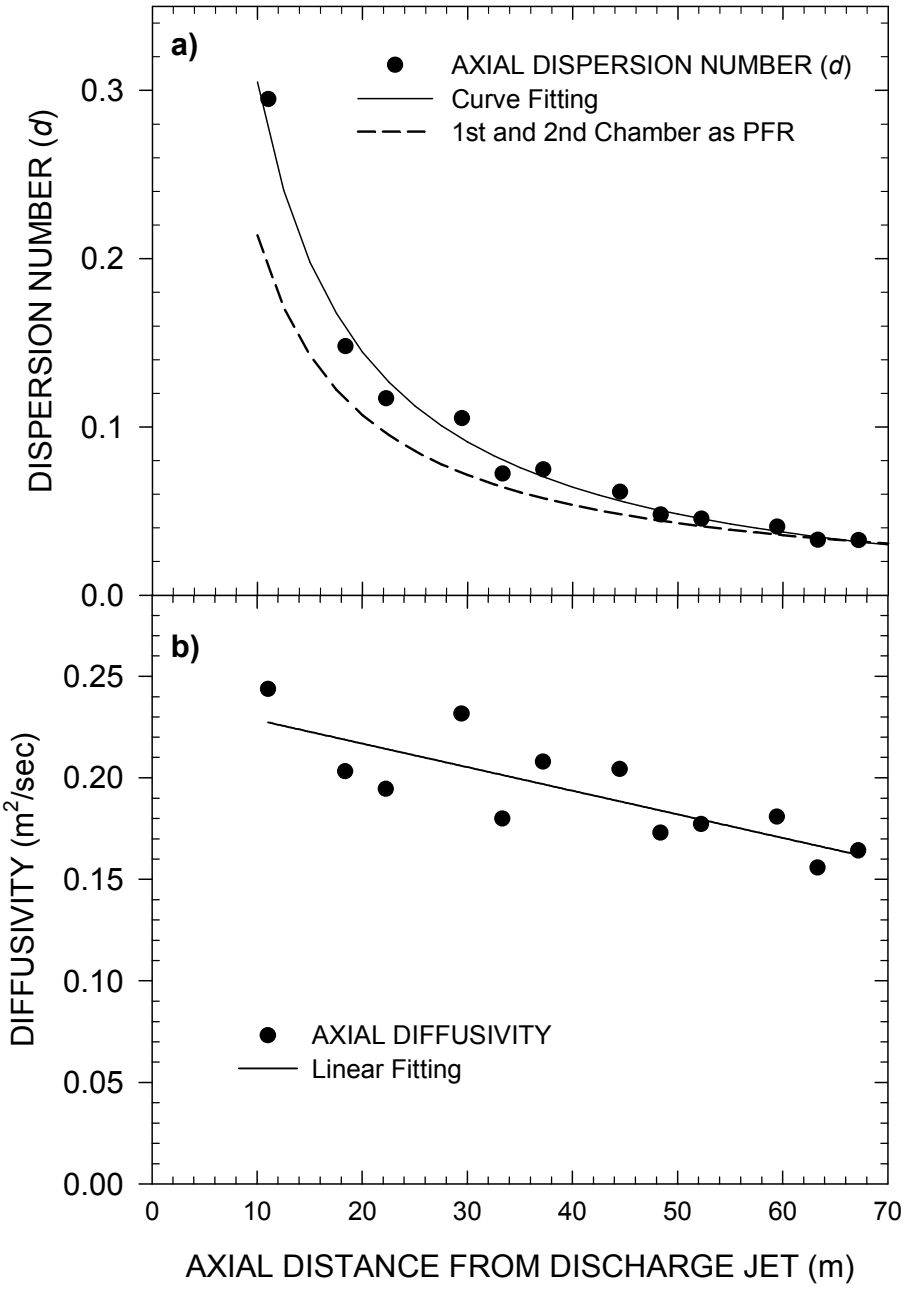

Figure 7.9. Diffusivity (a) and dispersion number (b) over axial distance from discharge jet

CHAPTER 8

SUMMARY AND CONCLUSIONS

Ozone disinfection is widely used, as *Cryptosporidium parvum* oocysts are prevalent in surface waters and commonly used chlorine-based disinfectants are ineffective in inactivating this pathogen. However, design and optimization of ozone disinfection processes in practice have been difficult due to superposition of complex chemical and biological reactions over non-ideal mixing conditions in ozone contactors. Integrated tools which support a designer or plant operator to handle these challenges are requested in the drinking water treatment field. Critical components of a recently proposed integrated ozone contactor design and optimization tool were either enhanced and newly developed in this study to optimize disinfection efficiency and disinfection by-product formation for new and existing ozone contactors.

The first component of the tool is a multi-channel stopped-flow reactor (MC-SFR), an instrument developed for automatic, continuous analysis of ozone decay kinetics in natural waters for the range of reaction times relevant to water treatment (*i.e.*, up to a few tens of minutes). The MC-SFR system is based on a novel flow injection analysis mechanism that mechanically separates the reaction fluid element providing preferred batch reaction conditions, while maintaining flow-through reactor advantages. These kinetics evaluations can be performed automatically in a near continuous manner. The instrument was verified using both synthetic and natural waters (Chapter 3) and later applied for real-world cases studies (Chapters 4 and 7).

Second, *Ozone Contactor Model* (*OCM*) software was upgraded for the validation of full-scale ozone contactors in support of current and future regulations regarding pathogen and bromate control in drinking water. Design of a new ozone contactor could

be another possible application of the *OCM* software. In this study, several important modifications were made for the first generation *OCM* software especially with respect to its application in natural waters (Chapter 4). Furthermore, this study reports the first time application of the *OCM* to simulate performance of full-scale ozone contactors which is currently under operation.

Finally, three dimensional laser induced fluorescence (3D-LIF) technique was applied to quantitatively investigate the mixing conditions within the ozone contactor, as a new component of the integrated design tool. This technique allows real time characterization of axial and lateral mixing in a physical model ozone contactor by capturing fluorescence light emitted from a dye using a high speed CCD camera. 3D-LIF technology was successfully applied to analyze flow hydrodynamics of horizontal flow, direct discharge ozone contactor with side-stream venture injector system (Chapter 5) and vertical flow, multi-chamber ozone contactor with fine bubble diffuser with high reliability and reproducibility. (Chapter 6)

As each design tool was developed, this study attempted the use of integrated ozone disinfection system design package (i.e., MC-SFR, OCM software, and 3D-LIF system) for a design of new ozone contactor under planning stage. *OCM* software predicts *CT*, residual ozone concentration, *C. parvum* oocyst log inactivation, and bromate formation using ozone decay kinetic data from MC-SFR. 3D-LIF system recommended enhanced contactor configuration through dispersion number and mixing analysis (Chapter 7).

Following major conclusions are drawn from this research:

1) MC-SFR system measures ozone decay kinetic constant accurately and reproducibly with flexible applicability in regard to both reaction times (*i.e.* seconds to minutes) and analyses (*i.e.* residual ozone and *p*CBA concentrations).

2) The MC-SFR provided useful information regarding ozone decay and hydroxyl radical generation in natural waters. It was found that hydroxyl radical concentration was much higher during the initial phase of ozone decay compared to later first-order decay stages. In particular, the ability of MC-SFR to measure the initial phase kinetics accurately might prevent the problems associated with overestimation of ozone and radical exposure which might be occurring when ozone and radical reactions during the initial phase are assumed to be instantaneous.

3) The *OCM* software was verified by predicting precisely both ozone concentration and bromate formation measured in a full scale ozone contactor. This validates the approach of axial dispersion reactor model approximation for the full-scale process.

4) Consistent with findings from the lab- and pilot-scale experiments and modeling, hydrodynamics of the ozone contactor plays a critical role in overall performance of full-scale reactors. When mixing conditions become close to plug-flow (*i.e.* lower dispersion number), ozone dosage required to achieve the same target inactivation efficiency would be significantly lower that that is required under high mixing condition. This also would result in lower bromate formation for the same target *C. parvum* inactivation.

5) This study reports the first successful application of 3D-LIF technique for the quantitative flow visualization in ozone disinfection reactors. This overcomes the

limitation of the past approaches where the reactor was considered as “blackbox”, such that modeling result was not able to provide specific design suggestions to improve the performance.

6) For the ozone contactor with side-stream venturi injection (SVI), influent flow behavior was found to play a critical role in mixing conditions throughout the ozone contactor. For example, the diameter of injection pipe was found to determine the mixing characteristics in the first chamber of the ozone contactor consisting of two chambers in series, causing short-circuiting under lower mixing energy condition. Under high momentum injection, the influent water formed spiral swirling which progressed toward the flow direction, resulting in lower overall mixing along the axial direction. Such a design might be in particular preferred in design of venturi injection reactors.

7) Installation of a diffusion wall for lower momentum flux and better lateral mixing was attempted for the ozone contactor with SVI. However, diffusion wall was not found to be effective because it hindered the swirling effect and caused back-flow in an ozone contactor.

8) 3D-LIF was further applied to simulate the hydraulics of full-scale ozone contactor. The tracer test results obtained with the full-scale ozone contactor matched well with the ones obtained with the laboratory-scale replicate reactor.

9) Visual observation of flow in the multi-chambered ozone contactor using 3D-LIF provided the experimental evidence for the existence of short-circuiting, internal recirculation within each chamber and presence of stagnant zones. Such phenomena explain why the reactor with many chambers would exhibit relatively high dispersion in full-scale designs, highlighting limitations of current full-scale design.

CHAPTER 9

FUTURE WORKS

9.1. Reactive Tracer Test for Measuring Three Dimensional Ozone Concentration

Measuring three dimensional ozone concentration profile is very important for precise assessment of disinfection efficiency and by-product formation. Fluorescent-dyed micro-spheres (1.0 μm diameter) and ozone stock solution is injected continuously into the influent of physical model ozone contactor treating natural water. When micro-spheres are exposed to dissolved ozone, the ozone diffuses into the particles, reacting with dye inside the particles. Reacted particle loses its fluorescence in relation to *CT* values. Residual fluorescence is measured using 3D-LIF system and converted into *CT* values by post-processing. The measured three dimensional *CT* could be used to predict pathogen inactivation and disinfection by-product formation, which could be further compared with the predicted results using *OCM* software. This will clearly reveal the effect of three dimensional hydrodynamics inactivation and disinfection by-product formation.

9.2. An ozone contactor numerical simulation using computational fluid dynamics (CFD)

Recent progress in CFD makes it possible to predict accurately three dimensional turbulent hydrodynamics and chemical reaction in ozone contactors. The advantages of CFD are simplicity of numerical experiments once established. CFD could replace full scale experiments which require time, labor, and financial cost. However, CFD should be verified and calibrated through actual experimental data. Experimental data from 3D-LIF could be used to calibrate related constants and verify simulation results. CFD coupled with chemical and biological reaction could be powerful and comprehensive tool to

analyze the complex hydrodynamics and reactions of an ozone contactor for design and operation optimization.

9.3. Applying to other disinfectants: free and residual chlorine

Integrated ozone contactor design system could be applied to other disinfectant after simple modification in chemical reaction. Possible disinfectants are free chlorine and monochloramine. Disinfection system using free chlorine is also required to optimize disinfection efficiency and disinfection by-product formation through integrated tools like those used for ozone disinfection. Chlorine disinfection produces tri halo methane (THM), halo acetic acids (HAA) as disinfection by-product.

Clear well serves a reactive chamber for disinfection system using free chlorine. Non-ideal flow, including short-circuiting, back-flow, and stagnant zone, are critical to reduce risks of DBP formation and maximize disinfection at the clear wells. Application of 3D-LIF system to clear well is though to serve as a powerful tool to enhance its hydrodynamics.

Monochloramine is used as a residual disinfectant to suppress microbial re-growth in the drinking water distribution system. It is produced by reacting chlorine gas or free chlorine with liquid ammonia at the final stage of drinking water treatment plant. However, its formation efficiency is known to be affected by mixing efficiency of their reacting chamber. The mixing level and its formation efficiency needs be carefully assesses to avoid excessive mixing, which might consume more energy for mixing. 3D-LIF system could provide direct assessment for mixing intensity needed for optimization of mixing and formation efficiency.

REFERENCES

Adams, et al, 1997. Effects of ozonation on the biodegradability of substituted phenols. *Water Research*, 31:10:2655.

Amy, et al, 2000. Bromate formation under ozonation conditions to inactivate Cryptosporidium. *Water Science and Technology*, 41:7:61.

Amy, et al, 1991. The Effects of Ozonation and Activated Carbon Adsorption on Trihalomethane Speciation. *Water Research*, 25:2:191.

Andreozzi, et al, 2001. Kinetic modeling of pyruvic acid ozonation in aqueous solutions catalyzed by Mn(II) and Mn(IV) ions. *Water Research*, 35:1:109.

Andreozzi, et al, 2003. Paracetamol oxidation from aqueous solutions by means of ozonation and H_2O_2/UV system. *Water Research*, 37:5:993.

Bader & Hoigne, 1981. Determination of Ozone in Water by the Indigo Method. *Water Research*, 15:4:449.

Bahnemann & Hart, 1982. Rate Constants of the Reaction of the Hydrated Electron and Hydroxyl Radical with Ozone in Aqueous-Solution. *J Phys Chem-Us*, 86:2:252.

Bellamy, et al, 2000. Determining disinfection needs. *Journal American Water Works Association*, 92:5:44.

Buhler, et al, 1984. Ozone Decomposition in Water Studied by Pulse-Radiolysis .1. $HO_2/O_2^-$and HO_3/O_3^- as Intermediates. *J Phys Chem-Us*, 88:12:2560.

Burguera, 1989. "Flow Injection Atomic Spectroscopy". *Practical Spectroscopy Series*, 7.

Carlson & Silverstein, 1997. Effect of ozonation on sorption of natural organic matter by biofilm. *Water Research*, 31:10:2467.

Chiou, et al, 1995. Modified Indigo Method for Gaseous and Aqueous Ozone Analyses. *Ozone-Science & Engineering*, 17:3:329.

Cho, et al, 2003. Investigation of ozone reaction in river waters causing instantaneous ozone demand. *Ozone-Science & Engineering*, 25:4:251.

Craik, et al, 2001. Inactivation of Cryptosporidium parvum oocysts using medium- and low-pressure ultraviolet radiation. *Water Research*, 35:6:1387.

Do-Quang, et al, 2000a. Influence of geometrical characteristics and operating conditions on the effectiveness of ozone contacting in fine-bubbles conventional diffusion reactors. *Ozone-Science & Engineering*, 22:4:369.

Do-Quang, et al, 2000b. Mathematical modeling of theoretical Cryptosporidium inactivation in full-scale ozonation reactors. *Ozone-Science & Engineering*, 22:1:99.

Dojlido, et al, 1999. Formation of the haloacetic acids during ozonation and chlorination of water in Warsaw waterworks (Poland). *Water Research*, 33:14:3111.

Dore, et al, 1980. Mechanism of Ozonation of Herbicides Derived from Phenoxyacetic Acid - 2-4d and Mcpa. *Water Research*, 14:7:767.

Driedger, et al, 2000. Sequential inactivation of Cryptosporidium parvum oocysts with ozone and free chlorine. *Water Research*, 34:14:3591.

Driedger, et al, 2001. Inactivation of Cryptosporidium parvum oocysts with ozone and monochloramine at low temperature. *Water Research*, 35:1:41.

El-Din & Smith, 2001. Development of transient Back Flow Cell Model (BFCM) for bubble columns. *Ozone-Science & Engineering*, 23:4:313.

Elmgharitabib, et al, 1982. Ozonation of Amines in Aqueous-Solutions. *Water Research*, 16:2:223.

Elovitz & von Gunten, 1999a. The effect of DNOM properties on the kinetics of ozone decomposition and hydroxyl radical scavenging. *Abstr Pap Am Chem S*, 217:U729.

Elovitz & von Gunten, 1999b. Hydroxyl radical ozone ratios during ozonation processes. I-The R-ct concept. *Ozone-Science & Engineering*, 21:3:239.

Elovitz & vonGunten, 1997. Influence of pH, temperature and DOM source on hydroxyl radical yields during ozonation. *Abstr Pap Am Chem S*, 213:15.

Ettema, et al, 2000. Hydraulic modeling: Concepts and practice.

Finch & Belosevic, 2001. Controlling Giardia spp. and Cryptosporidium spp. in drinking water by microbial reduction processes. *Canadian Journal of Civil Engineering*, 28:67.

Gilbert, 1987. Biodegradability of Ozonation Products as a Function of Cod and Doc Elimination by Example of Substituted Aromatic Substances. *Water Research*, 21:10:1273.

Grayman, et al, 1996. Water quality and mixing models for tanks and reservoirs. *Journal American Water Works Association*, 88:7:60.

Greene, et al, 2004. CFD design approach for chlorine disinfection processes. *Journal American Water Works Association*, 96:8:138.

Gurol & Singer, 1982. Kinetics of Ozone Decomposition - a Dynamic Approach. *Environ Sci Technol*, 16:7:377.

Gyurek, et al, 1999. Ozone inactivation kinetics of Cryptosporidium in phosphate buffer. *Journal of Environmental Engineering-Asce*, 125:10:913.

Hannoun, et al, 1998. Using hydraulic modeling to optimize contact time. *Journal American Water Works Association*, 90:8:77.

Heathcote & Drage, 1995. Development of an Ozone Disinfection Contactor Using a Physical Scale-Model. *Ozone-Science & Engineering*, 17:1:15.

Henry & Freeman, 1995. Finite element analysis and T-10 optimization of ozone contactors. *Ozone-Science & Engineering*, 17:6:587.

Hoigne & Bader, 1976. Role of Hydroxyl Radical Reactions in Ozonation Processes in Aqueous-Solutions. *Water Research*, 10:5:377.

Hoigne & Bader, 1983. Rate Constants of Reactions of Ozone with Organic and Inorganic-Compounds in Water .2. Dissociating Organic-Compounds. *Water Research*, 17:2:185.

Hoigne & Bader, 1988. The Formation of Trichloronitromethane (Chloropicrin) and Chloroform in a Combined Ozonation Chlorination Treatment of Drinking-Water. *Water Research*, 22:3:313.

Hoigne, et al, 1985a. Rate Constants of Reactions of Ozone with Organic and Inorganic-Compounds in Water .3. Inorganic-Compounds and Radicals. *Water Research*, 19:8:993.

Hoigne, et al, 1987. Rate Constants for Oh Radical-Scavenging by Humic Substances - Role in Ozonation and in a Few Photochemical Processes for the Elimination of Micropollutants. *Abstr Pap Am Chem S*, 193:78.

Hoigne, et al, 1985b. Oh Radical Formation in Natural-Waters - Experimental-Method and Interpretation of Results. *Abstr Pap Am Chem S*, 189:APR-:63.

Huang, et al, 2002. A computational fluid dynamic and experimental study of an ozone contactor. *Water Science and Technology*, 46:9:87.

Hungerford, et al, 1985. Reaction-Rate Measurement by Flow-Injection Analysis Using the Gradient Stopped-Flow Method. *Anal Chem*, 57:9:1794.

Hunt & Marinas, 1997. Kinetics of Escherichia coli inactivation with ozone. *Water Research*, 31:6:1355.

Hwang, et al, 1994. Removal of Odorous Compounds in Waste-Water by Using Activated Carbon, Ozonation and Aerated Biofilter. *Water Research*, 28:11:2309.

Khudenko & Shpirt, 1986. Hydrodynamic Parameters of Diffused Air Systems. *Water Research*, 20:7:905.

Kim, 2004. Real-time monitor and control of ozone disinfection process *International Ozone Association - Pan American Group Regional Conference, Windsor, Ontario.*

Kim, et al, 2007. Modeling Cryptosporidium parvum oocyst inactivation and bromate in a flow-through ozone contactor treating natural water. *Water Research*, 41:2:467.

Kim, et al, 2006a. A MULTI-CHANNEL STOPPED-FLOW REACTOR FOR MEASURING OZONE DECAY RATE: INSTRUMENT DEVELOPMENT AND APPLICATION. *ozone science and engineering*.

Kim, et al, 2006b. SIMULTANEOUS SIMULATION OF PATHOGEN INACTIVATION AND BROMATE FORMATION IN FULL-SCALE OZONE CONTACTORS. *J. of AWWA*.

Kim, et al, 2006c. Simultaneous Simulation of Pathogen Inactivation and Bromate Formation in Full-Scale Ozone Contactor *Journal American Water Works Association*, Accepted.

Kim, et al, 2002. Inactivation of Cryptosporidium oocysts in a pilot-scale ozone bubble-diffuser contactor. II: Model validation and application. *Journal of Environmental Engineering-Asce*, 128:6:522.

Kim, et al, 2004. Simultaneous prediction of Cryptosporidium parvum oocyst inactivation and bromate formation during ozonation of synthetic waters. *Environ Sci Technol*, 38:7:2232.

Kim, et al, 2006d. Control of bromate ion and brominated organic compounds formation during ozone/hydrogen peroxide treatment of secondary effluent. *Water Science and Technology*, 53:6:169.

Kowbel, et al, 1982. Determination of Mutagenic Activity in Salmonella of Residual Fulvic-Acids after Ozonation. *Water Research*, 16:11:1537.

Kusakabe, et al, 1991. Destruction Rate of Volatile Organochlorine Compounds in Water by Ozonation with Ultraviolet-Radiation. *Water Research*, 25:10:1199.

Lev & Regli, 1992a. Evaluation of Ozone Disinfection Systems - Characteristic Concentration-C. *Journal of Environmental Engineering-Asce*, 118:4:477.

Lev & Regli, 1992b. Evaluation of Ozone Disinfection Systems - Characteristic Time-T. *Journal of Environmental Engineering-Asce*, 118:2:268.

Levenspiel, 1999. Chemical Reaction Engineering: 3th ed. *John Wiley & Sons, Inc.*

Makinia & Wells, 2005. Evaluation of empirical formulae for estimation of the longitudinal dispersion in activated sludge reactors. *Water Research*, 39:8:1533.

Martinson & Lucey, 2004. Reduction of mixing in jet-fed water storage tanks. *Journal of Hydraulic Engineering-Asce*, 130:1:75.

Mason, et al, 1990. Carbamate Insecticides - Removal from Water by Chlorination and Ozonation. *Water Research*, 24:1:11.

Melin & Odegaard, 2000. The effect of biofilter loading rate on the removal of organic ozonation by-products. *Water Research*, 34:18:4464.

Munson, et al, 1998. Fundamentals of fluid mechanics, 3rd ed.

Murrer, et al, 1995. The development of an ozone contact tank simulation model. *Ozone-Science & Engineering*, 17:6:607.

Nemes, et al, 2000. The kinetics and mechanism of aqueous ozone decomposition in alkaline solution. *Inorg React Mech*, 2:4:327.

Nishijima, et al, 2003. DOC removal by multi-stage ozonation-biological treatment. *Water Research*, 37:1:150.

Onari, 1988. Determination of Ozone Decomposition Rate by Flow-Injection Technique. *Anal Sci*, 4:6:645.

Park, et al, 2004. Kinetic decomposition of ozone and para-chlorobenzoic acid (pCBA) during catalytic ozonation. *Water Research*, 38:9:2285.

Park, et al, 2001. Characterisation of raw water for the ozone application measuring ozone consumption rate. (vol 35, pg 2607, 2001). *Water Research*, 35:14:3515.

Pinkernell & von Gunten, 2001. Bromate minimization during ozonation: Mechanistic considerations. *Environ Sci Technol*, 35:12:2525.

Rakness, et al, 2005. Cryptosporidium log-inactivation with ozone using effluent CT_{10}, geometric mean CT_{10}, extended integrated CT_{10} and extended CSTR calculations. *Ozone-Science & Engineering*, 27:5:335.

Reckhow, et al, 1986. The Ozonation of Organic Halide Precursors - Effect of Bicarbonate. *Water Research*, 20:8:987.

Rennecker, et al, 2000. Synergism in sequential disinfection of Cryptosporidium parvum. *Water Science and Technology*, 41:7:47.

Rennecker, et al, 1999. Inactivation of Cryptosporidium parvum oocysts with ozone. *Water Research*, 33:11:2481.

Roberts & Snyder, 1993. Hydraulic Model Study for Boston Outfall .1. Riser Configuration. *Journal of Hydraulic Engineering-Asce*, 119:9:970.

Rositano, et al, 2001. Ozonation of NOM and algal toxins in four treated waters. *Water Research*, 35:1:23.

Rossman & Grayman, 1999. Scale-model studies of mixing in drinking water storage tanks. *Journal of Environmental Engineering-Asce*, 125:8:755.

Roustan, et al, 1993. Modeling Hydraulics of Ozone Contactors. *Ozone-Science & Engineering*, 15:3:213.

Roustan, et al, 1996. Bromate ion formation: Impact of ozone contactor hydraulics and operating conditions. *Ozone-Science & Engineering*, 18:1:87.

Ruzicka, 1988. Flow Injection Analysis. *Volume 62 of Chemical Analysis*.

Schmidtke & Smith, 1983. Scale-up of water and wastewater treatment processes

Schulz & Bellamy, 2000. The role of mixing in ozone dissolution systems. *Ozone-Science & Engineering*, 22:4:329.

Schulz, et al, 1995. Evaluating a High-Efficiency Ozone Injection Contactor. *Journal American Water Works Association*, 87:8:85.

Siddiqui, et al, 1996. Bromate ion removal by activated carbon. *Water Research*, 30:7:1651.

Singer & Hull, 2000. Modeling dissolved ozone behavior in ozone contactors. *AWWA Research Foundation, Denver, Colorado*

Singer, et al, 1992. Kinetics of Ozone Decomposition - Effects of Ph, Carbonate, and Humic Substances. *Abstr Pap Am Chem S*, 203:237.

Singer & Zilli, 1975. Ozonation of Ammonia in Wastewater. *Water Research*, 9:2:127.

Snoeyink & Jenkins, 1980. Water Chemistry. *John Wiley & Sons, Inc.*

Song, et al, 1996. Bromate formation and control during water ozonation. *Environ Technol*, 17:8:861.

Staehelin, et al, 1984. Ozone Decomposition in Water Studied by Pulse-Radiolysis .2. Oh and Ho4 as Chain Intermediates. *J Phys Chem-Us*, 88:24:5999.

Staehelin & Hoigne, 1982. Decomposition of Ozone in Water - Rate of Initiation by Hydroxide Ions and Hydrogen-Peroxide. *Environ Sci Technol*, 16:10:676.

Stockinger, et al, 1996. Ozonation of wastewater containing N-methylmorpholine-N-oxide. *Water Research*, 30:8:1745.

Straka, et al, 1985. Residual Aqueous Ozone Determination by Gas-Diffusion Flow-Injection Analysis. *Anal Chem*, 57:9:1799.

Straka, et al, 1984. Residual Ozone Determination by Flow-Injection Analysis. *Anal Chem*, 56:11:1973.

Tang, et al, 2005. Modeling Cryptosporidium parvum oocyst inactivation and bromate formation in a full-scale ozone contactor. *Environ Sci Technol*, 39:23:9343.

Tian & Roberts, 2003. A 3D LIF system for turbulent buoyant jet flows. *Experiments in Fluids*, 35:6:636.

Tomiyasu, et al, 1985. Kinetics and Mechanism of Ozone Decomposition in Basic Aqueous-Solution. *Inorg Chem*, 24:19:2962.

Tomiyasu & Gordon, 1984. Colorimetric Determination of Ozone in Water Based on Reaction with Bis(Terpyridine)Iron(Ii). *Anal Chem*, 56:4:752.

USEPA, 1991. Guidance manual for compliance with the filtration and disinfection requirements for public water systems using surface water sources. *USEPA, Washington*.

USEPA, 1994. Federal Register. *59*, 145:33668.

USEPA, 2003. Stage 2 Occurrence Assessment for Disinfectants and Disinfection Byproducts;. *EPA 68-C-99-206: Washington, DC*.

USEPA, 2006. National Primary Drinking Water Regulations : Long Term 2 Enhanced Surface Water Treatment Rule; Final Rule, edited, . *Fedral Register* 71:3:654.

von Gunten, 2003. Ozonation of drinking water: Part I. Oxidation kinetics and product formation. *Water Research*, 37:7:1443.

von Gunten & Hoigne, 1994. Bromate Formation During Ozonation of Bromide-Containing Waters - Interaction of Ozone and Hydroxyl Radical Reactions. *Environ Sci Technol*, 28:7:1234.

von Gunten & Pinkernell, 2000. Ozonation of bromide-containing drinking waters: a delicate balance between disinfection and bromate formation. *Water Science and Technology*, 41:7:53.

von Gunten & Zobrist, 1993. Biogeochemical Changes in Groundwater-Infiltration Systems - Column Studies. *Geochim Cosmochim Ac*, 57:16:3895.

Westerhoff, et al, 1997. Applications of ozone decomposition models. *Ozone-Science & Engineering*, 19:1:55.

WHO, 1990. IARC Monographs on the evaluation of carcinogenic risks to humans; WHO: Geneva, 52.

Widmer, et al, 1996. Water-borne Cryptosporidium: A perspective from the USA. *Parasitology Today*, 12:7:286.

Yang, et al, 1999. Ammonia removal in bubble column by ozonation in the presence of bromide. *Water Research*, 33:8:1911.

Yavich, et al, 2004. Evaluation of biodegradability of NOM after ozonation. *Water Research*, 38:12:2839.

VITA

DOO-IL KIM

Doo-Il Kim was born in Andong in South Korea. He received his bachelor's degree in Civil Engineering (Urban Engineering Major) from Seoul National University, Seoul, South Korea in 1991 and a master's degree in Civil Engineering (Urban Engineering Major) from Seoul National University, Seoul, South Korea in 1993. He joined for the *Samsung Institute for Construction Technology*, Construction Division of SAMSUNG Corporation, before coming to Georgia Tech to pursue a doctorate in Civil and Environmental Engineering in 2002. His research was focused on the development of ozone contactor design and optimization tools, called as MC-SFR, *OCM* software, 3D-LIF system.